Investigations on TiO_2 Based Nanocomposites as Potential Photonic Materials

Ph D Thesis submitted to

Cochin University of Science and Technology

In partial fulfilment of the requirements for the award of the Degree of

Doctor of Philosophy

Divya S.

Reg. No: 3997

International School of Photonics
Faculty of Technology
Cochin University of Science and Technology
Cochin -682022, Kerala, India

May 2015

Investigations on TiO_2 based nanocomposites as potential photonic materials

Ph D thesis in the field of Photonics

Author:

Divya.S
Research Fellow
International School of Photonics
Cochin University of Science & Technology
Cochin -682022, Kerala, India
divyasasi7@gmail.com

Research Advisor:

Dr. A. Mujeeb
Associate Professor
International School of Photonics
Cochin University of Science & Technology
Cochin -682022, Kerala, India
mujeeb@cusat.ac.in

Research Co-Advisor:

Dr. P. Radhakrishnan
Professor
International School of Photonics
Cochin University of Science & Technology
Cochin -682022, Kerala, India
radhak@cusat.ac.in, padmanabhan.radhak@gmail.com

International School of Photonics
Cochin University of Science & Technology
Cochin -682022, Kerala, India
www.photonics.cusat.edu

May 2015

Cover image: SEM images of TiO_2 nanotrees.
Cover design: Adrine Correya.

Dedicated to

My Loving Family……

INTERNATIONAL SCHOOL OF PHOTONICS
COCHIN UNIVERSITY OF SCIENCE AND TECHNOLOGY
COCHIN -682022, KERALA, INDIA

Dr. A. Mujeeb
Associate Professor

Certificate

This is to certify that the thesis entitled **“Investigations on TiO_2 Based Nanocomposites as Potential Photonic Materials”** submitted by **Divya S.**, is an authentic record of research work carried out by her under my guidance and supervision in partial fulfilment of the requirement of the degree of Doctor of Philosophy of Cochin University of Science and Technology, under the Faculty of Technology and has not been included in any other thesis submitted previously for the award of any degree.

Kochi-682022
20 - 05- 2015

Dr. A. Mujeeb
(Supervising guide)

Phone: +91 484 2575848 Fax: 0091-484-2576714.
Email: mujeeb@cusat.ac.in

INTERNATIONAL SCHOOL OF PHOTONICS
COCHIN UNIVERSITY OF SCIENCE AND TECHNOLOGY
COCHIN -682022, KERALA, INDIA

Dr. A. Mujeeb
Associate Professor

Certificate

This is to certify that the thesis entitled **"Investigations on TiO_2 Based Nanocomposites as Potential Photonic Materials"** submitted by **Divya S.**, has incorporated all the relevant corrections and modifications suggested by the audience during the pre-synopsis seminar and recommended by the Doctoral Committee.

Kochi-682022
20- 05- 2015

Dr. A. Mujeeb
(Supervising guide)

Phone: +91 484 2575848 Fax: 0091-484-2576714.
Email: mujeeb@cusat.ac.in

Declaration

I, Divya S., do hereby declare that the thesis entitled **"Investigations on TiO_2 Based Nanocomposites as Potential Photonic Materials"** is a genuine record of research work done by me under the supervision of Dr. A. Mujeeb, Associate Professor, International School of Photonics, Cochin University of Science and Technology, Kochi–22, India and it has not been included in any other thesis submitted previously for the award of any degree.

Kochi- 682022 **Divya S.**
20- 05- 2015

Acknowledgements

The work presented here in this dissertation could not have been done without the help of many people with whom I am associated. Thanking them with few words is an impossible task but I believe through these acknowledgements I am able to convey my deepest and sincere feelings to them.

First and foremost, I owe tremendous amounts of gratitude to my research supervisor ***Dr. A. Mujeeb*** *for giving me the chance to study under his direction. He has been an admirable supervisor by giving the freedom to work and also support and motivation. As my supervisor, he constantly reminded me to remain focused on achieving my goals.*

I thank ***Prof. P.Radhkrishnan****, for his fruitful discussions and consultations. I sincerely thank him for his constructive suggestions on my research papers and thesis. I am also deeply indebted to him for granting me a chance to visit Finland as part of my research to work with elite personality like* ***Prof. Martt Kauranen****. I would like to thank* ***Prof .V P N Nampoori*** *without whom I wouldn't understand half of what I've written herein this thesis. His constant support, guidance, patience and wise mentoring have helped in bringing out this thesis in final form.*

I sincerely thank ***Prof. C. P. Girijavallabhan, Dr. M. Kailasnath and Dr. Sheenu Thomas*** *for their timely help and encouragement. The financial assistance from* ***Inspire Fellowship****, funded by* ***DST India*** *is greatly acknowledged. I would also like to mention the help and assistance given to me by the* ***non- teaching staff*** *of ISP.*

During my research life I had made several friends whom I never want to lose. They have become so important that I can't imagine a life without them. My special mention goes to my twin, ***Indu****. Thankyou for making my life so enjoyable in all respects. It was a delight to be in company of* ***Tintuchechi, Susmitha, Aparna, Sister, Suneetha, Jaison, Nideep, Ajina, Mathew, Ratheesh, Linslal. Bobby sir, Pradeep, Adrine, Boney****. Thankyou guys, it was indeed a pleasure to be with all of you.*

Thanks definitely need to go to ***my parents*** *for their continued support throughout my life. They supported me with everything they had to enable me to overcome all the obstacles I had to face. Finally, I would like to thank my husband* ***Shreeraj*** *for being with me. Last but most important of all, I thank God for his blessings.*

Divya S.

“The task is...not so much to see what no one has yet seen; but to think what nobody has yet thought, about that which everybody sees.”

— Erwin Schrödinger

Preface

Nano materials with large third-order nonlinear susceptibility $\chi^{(3)}$ and ultrafast response have been under continuous scientific interest because of their potential applications for all-optical switching, light-controlled phase, refractive index modulation and optical power limiting devices. These nano materials can be inorganic, organic or various combinations of both classes of materials. Such nano scale composite materials containing metal oxides have been continuously focussed by the research community for their impending claims in the field of optoelectronic devices. In particular, TiO_2 has gained widespread acclaim for its prospective applications such as, in dye sensitized solar cells, photo catalysts, gas sensors, electro-chromic devices, biomaterials and so on. In this context, this thesis has been devoted for the detailed investigation of TiO_2 and TiO_2 based nanocomposites materials. The present thesis has been organized into seven chapters with its each chapter describing different aspects of TiO_2.

Chapter 1 gives an overview on the basics of TiO_2 in terms of its structure, properties and applications. Brief description regarding the structural, electronic and optical properties of the semiconductor has been provided. The innumerable favourable property of the material enables its efficient utilization in various scientific innovations. Various important applications of the material that has revolutionized the basic technology benefiting mankind have been included with working principle and schematic representations.

Chapter 2 focusses on the synthesis of the material and the experimental tools and techniques used in the present work. Mostly, we have employed sol gel and solvothermal methods for synthesis and hence detailed account of these methods have been given. Different characterization tools along with the specifications and experimental techniques with its theory used for analysis of the samples are also discussed. Detailed assembling and characterization of Dye Sensitised Solar Cells are also included in the later sections of the chapter.

Chapter 3 presents the synthesis and characterization of TiO_2 and its two important crystalline polymorphs; anatase and rutile. Studies revealed that the variation of optical band gap with temperature is synonymous with the formation of the polymorphs. Fluorescence studies revealed the presence of more imperfections and disorders in anatase than rutile. Nonlinear optical studies showed that optical constants of amorphous TiO_2 varied with subjected temperature. Discussions for such phenomenon are presented in the chapter with valid arguments. It is believed that this can be due to the variation in the electronic structure of TiO_2 with temperature.

Chapter 4 deals with morphology dependent optical studies of TiO_2 nanostructures. Size and shape dependent confinement systems have been continuously under scientific attention as with morphology, physical properties such as large binding energy, giant oscillator strength, large nonlinearity and short decay time varies. With such variation in the size and shape of the nanomaterials, symmetry of electronic states of the material also changes. Nanostructured TiO_2 in different shapes such as nanowires, nanosheets, nanospheres as well as nanoflowers have been prepared and characterized. Linear and nonlinear optical behaviour of the nanostructured TiO_2 is found to be shape dependent and is accounted in terms of effective surface-to-volume ratio of the structures.

Chapter 5 reports the synthesis and detailed discussions regarding the material chemistry of various TiO_2 based nanocomposites. Composite materials are especially of interest in developing efficient light-energy conversion systems, optical devices and microelectronics. Nanomaterials often have unique properties which enables us to realize composite materials with simultaneous multiple unique properties. It is possible to tailor the linear and nonlinear optical properties of semiconductor by doping with other potential candidates in relation to their various possible applications. The present chapter deals with the optical characterization of various TiO_2 based nanocomposites viz.- TiO_2-SiO_2, TiO_2-CeO_2, TiO_2-N (TiN), TiN-PVA. Their linear optical studies are performed using absorption and fluorescence spectroscopy whereas nonlinear optical characterization is done using Z-scan and valuable conclusions are drawn. For TiN-PVA, linear and nonlinear optical properties were studied from theoretical and experimental method. Theoretical method involved Tichy and Ticha relation pooled with generalised Miller's rule. The results derived from theoretical method differed greatly from the experimental .We believe that such incongruity is due to the SPR property of the TiN nanoparticle whose SPR peak almost coincides with the irradiated laser wavelength.

Chapter 6 deals with fabrication and characterization of Dye Sensitised Solar Cells (DSSCs). Human population is constantly growing with ever-evolving high quality of living standards, demanding the availability of never depleting source of energy. This has forced us to look for more environmental friendly, economically viable energy sources. DSSCs have emerged as the undisputed candidate among the different photovoltaic cells. Scientific community has been continuously engaged in efforts to increase the efficiency of cells by improving the spectral absorbance range by changing the dye; increasing the mobility of holes; stability of the cell by replacing the liquid electrolyte with solid and semi-solid electrolytes; improving the electron transport by varying the photoanode or by using morphologically different structures. The present chapter discusses in detail about the effect of electrolyte and effect of variation in the morphology as well as constituents of photoanode on the cell efficiency.

Chapter 7 points out the main conclusions of the present work along with few comments regarding future prospects.

List of Publications

Journal Publications

1. **Divya, S.**, Nampoori, V. P. N., Radhakrishnan, P., & Mujeeb, A. (2013). "Morphological Dependence on the Nonlinear Optical Behaviour of TiO_2 Nanostructures". *Adv. Electrochem.*, *1*(2), 124-127.

2. **Divya, S.**, Sebastian, I., Nampoori, V. P. N., Radhakrishnan, P., & Mujeeb, A. (2014). "Non-resonant excitonic effects on the third order nonlinear properties of TiO_2: From amorphous to rutile phase". *Opt. Laser Technol.*, *56*, 207-210.

3. **Divya, S.**, Nampoori, V. P. N., Radhakrishnan, P., & Mujeeb, A. (2014). "Evaluation of nonlinear optical parameters of TiN/PVA nanocomposite–A comparison between semi empirical relation and Z-scan results". *Curr. Appl. Phys.*, *14*(1), 93-98.

4. **Divya, S.**, Nampoori, V. P. N., Radhakrishnan, P., & Mujeeb, A. (2014). "Intermediate Ce^{3+} defect level induced photoluminescence and third-order nonlinear optical effects in TiO_2–CeO_2 nanocomposites". *Appl. Phys. A*, 114(2), 315-321.

5. **Divya, S.**, Thankappan, A., Vallabhan, C. P. G., Nampoori, V. P. N., Radhakrishnan, P., & Mujeeb, A. (2014). "Electrolyte/photoanode engineered performance of TiO_2 based dye sensitised solar cells". *J. Appl. Phys.*, *115*(6), 064501.

6. **Divya, S.**, Nampoori, V. P. N., Radhakrishnan, P., & Mujeeb, A. (2014). "Morphology dependent dispersion of third-order optical nonlinear susceptibility in TiO_2". *Appl. Phys. A*, *114*(4), 1079-1084.

7. **Divya, S.**, Nampoori, V. P. N., Radhakrishnan, P., & Mujeeb, A. (2014). "Intensity and composition-dependent sign reversal of non-linearity in TiO_2/CeO_2 nanocomposites". *Chin. Phys. B*, *23*(3), 034209.

8. **Divya, S.**, Sebastian, I., Nampoori, V. P. N., Radhakrishnan, P., & Mujeeb, A. (2014). "Tailoring optical properties of TiO_2 in silica glass for limiting applications". *Chin. Phys. B*, *23*(3), 034210.

9. **Divya, S.**, Nampoori, V. P. N., Radhakrishnan, P., & Mujeeb, A. (2014). "Electronic and optical properties of TiO_2 and its polymorphs by Z-scan method". *Chin. Phys. B*, *23*(8), 084203.

10. **Divya, S.**, Nampoori, V. P. N., Radhakrishnan, P., & Mujeeb, A. (2014). "Origin of optical non-linear response in TiN owing to excitation dynamics of surface plasmon resonance electronic oscillations". *Laser Phys. Lett.*, *11*(8), 085401.

11. **Divya, S.**, Sebastian, I., Nampoori, V. P. N., Radhakrishnan, P., & Mujeeb, A. (2014). "Band gap tuning and nonlinear optical characterization of TiO_2–SiO_2 nanocomposites with respect to composition and phase". *Opt. Mater.*, *37*, 433-438.

12. Thankappan, A., **Divya, S.**, Thomas, S., & Nampoori, V. P. N. (2013). "Optical characterization of ZnO nanoplates embedded in polymeric matrices for optical limiting applications". *Opt. Laser Technol.*, *52*, 37-42.

13. Sebastian, I., **Divya, S.**, Nampoori, V. P. N., Radhakrishnan, P., & Thomas, S. (2013). "Impact of intermediate localized states on nonlinear optical absorption of Ga-Ge-Se nanocolloidal solutions". *Appl. Phys. Lett.*, *102*(3), 031115.

14. Thankappan, A., Linslal, C. L., **Divya, S.**, Sabitha, P. V., Thomas, S., & Nampoori, V. P. N. (2014). "Optical nonlinear investigations on morphology controlled growth of ZnO crystals". *Opt. Laser Technol.*, *64*, 133-139.

15. Thankappan, A., **Divya, S.**, Augustine, A. K., Girijavallaban, C. P., Radhakrishnan, P., Thomas, S., & Nampoori, V. P. N. (2015). "Highly efficient betanin dye based ZnO and ZnO/Au Schottky barrier solar cell". *Thin Solid Films*, *583*, 102-107.

Conference Publications

1. **S. Divya**, Indu Sebastian,V. P. N. Nampoori, P. Radhakrishnan, and A. Mujeeb. (November 2011) "Nonlinear Optics of TiO_2- SiO_2 Nanocomposites". *National Symposium on Recent Advances in Nanoscience, Engineering & Technology (RANET-11)*, ABV-IIITM, Gwalior.

2. **S. Divya**, Indu Sebastian,V. P. N. Nampoori, P. Radhakrishnan, and A. Mujeeb. (December 2011) "Synthesis And Characterization Of TiO_2- SiO_2 Composites". *International Symposium in Frontiers of Photonics -2011 (FOP)*, IIT- Delhi, Delhi.

3. **S. Divya**, Indu Sebastian ,V. P. N. Nampoori, P. Radhakrishnan, and A. Mujeeb , (December 2011) "Observation of Saturable and Reverse Saturable Absorption in

SiO_2-TiO_2 Sol-Gel Colloids". *First International OSA Network of Students* (*IONS-OSA -2011)*, IIT- Delhi, Delhi.

4. **Divya, S**., Sebastian, I., Nampoori, V. P. N., Radhakrishnan, P., & Mujeeb, A. (July 2012). "Power and composition dependent nonlinear optical switching of TiO_2-SiO_2 nano composites". *International Conference on Optical Engineering (ICOE) IEEE,* (1-5).

5. **S. Divya**, V. P. N. Nampoori, P. Radhakrishnan, and A. Mujeeb, (April 2013) "Overview of electronic and optical properties of TiO_2 and its polymorphs via Z-scan method". *National Conference on Advance Materials and Applications* (*NCAMA)*, Nit Trichy.

6. **S. Divya**, V. P. N. Nampoori, P. Radhakrishnan, and A. Mujeeb, (June 2013) "Qualitative effects of laser irradiation on Titanium nitride nanoparticles". *International Conference on Materials for Advanced Technologies (ICMAT),* Singapore.

7. Aparna Thankappan, **S. Divya**, P. Radhakrishnan and V.P.N Nampoori, (January 2012) "Design and Fabrication of nano TiO_2 based Solar Cell Sensitized by Pomegranate Extract". *Kerala Science Congress*, Kerala.

8. Sebastian, I., **Divya, S**., Nampoori, V. P. N., Radhakrishnan, P., & Thomas, S. (July 2012). "Investigation on nonlinear properties of Ga-Ge-Se nanocolloidal solutions". *International Conference on Optical Engineering (ICOE) IEEE,* (1-4).

Contents

List of Figures

List of Tables

Chapter 1

Titanium dioxide (TiO_2): Structure, Properties and Applications

Abstract

This chapter overviews the basics of TiO_2 with respect to its structure, properties and applications. A brief account of its structural, electronic and optical properties is provided. Various emerging technological applications utilising TiO_2 is also discussed. With the last section of the chapter the scope of the present thesis is presented.

1.1 Introduction

Titanium dioxide (TiO_2) is one of the most investigated transition-metal oxides in material science. Ever since its commercial production in the early twentieth century, TiO_2 has been widely used as a pigment in sunscreens, paints, ointments, toothpaste as well as an important constituent in household plastics[1]. Titanium dioxide has long been used as a white pigment in paints and polymers. Since the discovery of photo catalytic water splitting on a TiO_2 electrode under ultraviolet (UV) light in 1972 by Fujishima and Honda[2], enormous scientific efforts have been devoted for the research of TiO_2 nanomaterials with respect to its application in wide range of areas including photovoltaics, photocatalysis, photo-/electrochromics, energy storage and sensors[3,4,5]. The number of scientific and technical publications on TiO_2 has been increasing exponentially since then. The database confirming such a statistics is shown in figure 1.1[6].

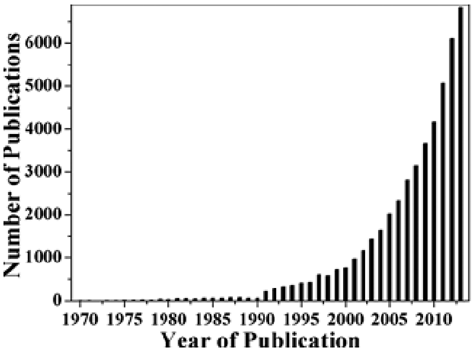

Figure 1.1: *Number of publications (Science Citation Index Expanded) in Web of Science when a search for the topic "titanium dioxide or titania or* TiO_2*" and "photo*" is performed.*

TiO_2 has various unique properties that make it a potential candidate for its diverse applications:

- ☐ *chemical*: chemical stability, corrosion/photo corrosion resistance, photo catalytic potential
- ☐ *electrical*: high dielectric constant ($\varepsilon_r \approx 60\text{-}100$)[7,8], increased electrical conductivity[9]
- ☐ *optical*: UV active[8,10], high band gap[9], high refractive index [10,11,12,13]
- ☐ *biological*: non-toxicity, biocompatibility [13,14]
- ☐ *economical*: low cost[15,16]

1.2 Properties

Structural, electrical and optical properties of TiO_2 are outlined in this section.

1.2.1 Structural Properties

TiO_2 is available in three stable polymorphic states: rutile, anatase and brookite as shown in figure 1.2[17] . Among these structures, rutile is the most stable phase[18]. Anatase and brookite are metastable phases that transform to rutile in the temperature range 973K–1173K depending on the grain size, ambient conditions and impurities[19]. Natural rutile crystals exhibit predominant (110) surface, which is considered to be the most stable surface of stoichiometric rutile, whereas anatase is most stable with (101) surface[20]. Both anatase and rutile have tetragonal crystal structures and contains 6 atoms per unit cell but belong to different space groups. However for the anatase phase, the distortion of the TiO_6 octahedron is slightly larger than that of the rutile phase. In rutile structure, each octahedron is in contact with 10 neighbouring octahedrons (two sharing edge oxygen pairs and eight sharing corner oxygen atoms) while in the anatase structure, each octahedron is in contact with eight neighbours (four sharing an edge and four sharing a corner). These differences in lattice structures render the two forms of TiO_2 different mass densities and electronic band structures. The brookite phase has an orthorhombic crystalline structure. Its unit cell is composed of 8 formula units of TiO_2 and is formed by edge-sharing TiO_6 octahedra. It has a larger cell volume and is the least dense and complicated among the three. However, this is an unstable phase and hence is of least scientific interest[21]. Schematic representation and structural data of TiO_2 in different phases are given in figure 1.2 and table 1.1 respectively.

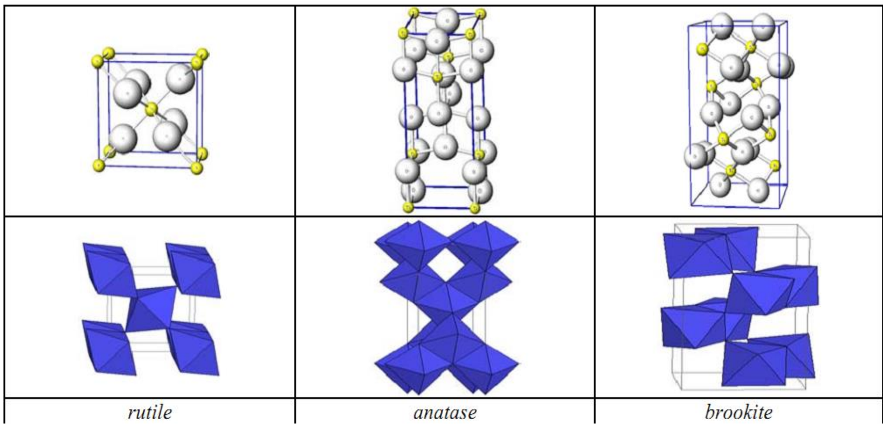

Figure 1.2: *Structure of three stable polymorphic states: rutile, anatase and brookite.*

Properties	**Rutile**	**Anatase**	**Brookite**
Crystal Structures	Tetragonal	Tetragonal	Orthorhombic
Lattice constants (A°)	a=4.5936 c=2.9587	a=3.784 c=9.515	a=9.184 b=5.447 c=51.54
Space groups	$P4_2/mnm$	$I4_1/amd$	Pbca
Molecule (cell)	2	2	4
Volume/molecule (A^{o3})	31.2160	34.061	32.172
Density (gcm^{-3})	4.13	3.79	3.99
Ti-O bond length (A°)	1.949 (4) 1.980 (2)	1.937(4) 1.965(2)	1.87-2.04
O-Ti-O bond angle	81.2° 90.2°	77.7° 92.6°	77.0°-105°

Table 1.1: *Crystal structure data for TiO_2.*

1.2.2 Thermodynamic Properties

Of all the three phases of TiO_2, rutile phase is the most stable at high temperatures for bulk form, whereas anatase and brookite are common in fine grained natural and synthetic sample in nanoscale regime. When the size of the nanoparticles is below 50nm, anatase is the most stable phase. The transformation from one phase to the other depends on the processing temperature and preparation method. Anatase phase was found to be transformed to rutile at > 973 K[22]. It has been found that prepared TiO_2 nanoparticles having anatase and/brookite structures, transforms to rutile after reaching a certain particle size. Once transformation to rutile was complete, it grew much faster than anatase. In studies conducted by Zhang and Banfield transformation sequence and thermodynamic phase stability depended on the initial particle sizes of anatase and brookite[23] . It was observed that for equally sized nanoparticles, anatase was thermodynamically stable for sizes < 11 nm, brookite was stable for sizes between 11nm and 35 nm and rutile was stable for sizes > 35 nm.

1.2.3 Electronic and Optical Properties

TiO_2 is one of the most important wide bandgap transition metal oxides with band gaps of 3.2, 3.02 and 2.96 eV for the anatase, rutile and brookite phases, respectively. The valence band of TiO_2 consists of 2p orbitals of oxygen hybridized with the 3d orbitals of titanium, while the conduction band has only the 3d orbitals of titanium. When TiO_2 is exposed to near-UV light, electrons in the valence band are excited to the conduction band leaving behind holes (h^+), as depicted in figure 1.3. The excited electrons (e^-) in the conduction band are now in a purely 3d state and because of dissimilar parity, the transition probability of e^- to the valence band decreases, reducing the probability of e^-/h^+ recombination.

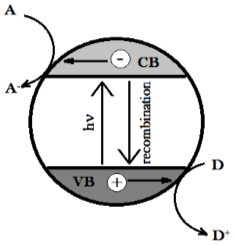

Figure 1.3: *Mechanism of light absorption by TiO_2.*

TiO_2 crystals have a high resistivity of $\sim 10^{15}$ Ωcm, and it is believed that bulk oxygen vacancies, titanium interstitials and reduced crystal surface generates shallow electron donor levels eventually contributing to the electric conductivity of TiO_2. It has been reported that replacement of oxygen by water vapour also significantly increases the electrical conductivity compared to films deposited with oxygen as reactive gas[24,25,26]. Point defects such as doubly charged oxygen vacancies and interstitial Ti ions with three or four charges also affect the conductivity and ionization energy in the case of rutile crystals[27]. Anatase TiO_2 has inherent surface band bending in a deeper region with a steeper potential compared to the rutile phase as represented in figure 1.4. In anatase, surface hole trapping dominates as the spatial charge separation is achieved by the transfer of photo generated holes towards the surface of the particle via the strong upward band bending. Although, in the rutile phase, the bulk recombination of electrons and holes occurs, with only holes very close to the surface being trapped and transferred to the surface.

TiO_2 nanomaterials have received a great deal of attention due to their high activity, strong oxidation capability and chemical stability. It has been reported that anatase thin film has different electrical and optical properties from the rutile film[28, 29]. This essential difference is mainly due to the variation in the band gap energies. Anatase has wider optical- absorption gap and smaller electron effective mass, thus resulting in a higher mobility for the charge carriers.

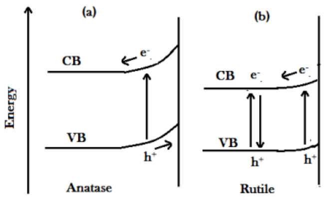

Figure 1.4: *Surface band bending of (a) anatase phase (b) rutile phase of* TiO_2.

These properties are beneficial for applications in optoelectronic and other useful devices. A rapid increase in the absorption takes place at low photon energies. It has been found that depending on the degree of reduction of rutile TiO_2, a blue colour arises from the visible tail of an IR absorption band with peak at about 0.75–1.18 eV [25,28,29,30,31,32]. Similarly, in anatase, the blue colour has been observed, which is caused by a wide absorption band with its maximum in the IR region. In addition, a colour centre at 3 eV due to an oxygen vacancy has been identified giving rise to a yellow colour [30,33].

1.3 Morphological Variations of TiO_2 Nanostructures

The physical and chemical properties of a material are governed by the type of motion allowed for its electrons to execute specific interactions which in turn directly depends on the space in which they are confined. Once the confinement process sets in, quantization occur leading to energy levels becoming well defined and distinct. Thus their electronic structures can be tailored by size and shape. Unlike the change in size, the change in shape often leads to variation in electronic state symmetries and their respective characteristics. It is believed that the shape can be used as a yard stick to engineer the electronic states in nanostructures. Basically the change in electronic structure refers to the change in single-particle electronic states which includes the state energy, the overall shape of the wave function, the symmetry, the polarization and the localization. Multitudes of research have been undertaken in the field of synthesis of novel structures and shapes like nanorods, nanoribbons, nanocubes, nanospheres, nanoflower, nanoprism etc. of various nanoparticles for harnessing their potential applications[34,35,36,37]. The control of size or shape can be achieved by adjusting the space in which the nanoparticles are allowed to grow. Due to the dependence of the semiconductor nanoparticle properties on their morphology, as well as on the fact that their surface to volume ratio varies incredibly, new properties are expected to arise that are not possessed by the individual entity. These modified features make the semiconductor TiO_2 viable for efficient utilization in many technological applications in variety of fields such as solar cells, heterogeneous photo catalysis and nonlinear optics[38,39,40,41]. The number of scientific articles published in the last decade in relation to titanium nanotube alone has crossed 1800[42]. As electrons and holes at the surface have wave functions with large amplitude, they have high probability of being trapped by surface impurities. This phenomenon further extends their use in the field of oxidation-reduction chemistry with many anticipated applications in fields such as photo-catalysis, photo-degradation and detoxification of chemical waste and environmental pollutants[43,44,45,46].

1.4 Modifications of TiO_2 Nanomaterials

Many applications of TiO_2 nanomaterials are closely linked to its optical properties and hence its band gap. However, sometimes its application is constrained by its wide band gap. Figure 1.5 shows the incoming solar radiation that reaches the earth surface[47]. According to this spectrum, the ultraviolet region and visible region constitutes to about 4% and 43%, respectively in the incoming solar radiation. The band gap of bulk TiO_2 lies in the UV regime (3.0 eV for the rutile phase and 3.2 eV for the anatase phase), which is only a small fraction of the solar energy (<10%). Thus in order to harness its potential, its optical activity is increased by shifting the response from UV to visible region[48,49,50] as shown in figure 1.6(a-d) .

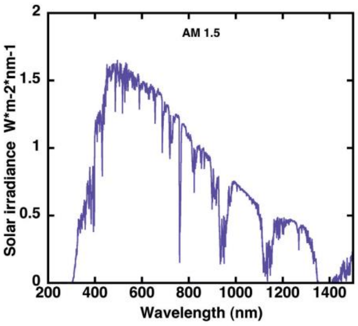

Figure 1.5: *Global air mass 1.5 solar spectral distributions.*

There are different methods to achieve this goal, such as (i) Doping TiO_2 nanomaterials with other elements can narrow the band gap and thus, altering the optical properties of TiO_2 nanomaterials.(ii) Sensitizing TiO_2 with other colourful inorganic or organic compounds thereby improving its optical activity in the visible spectral region.(iii) Coupling collective oscillations of the electrons in the conduction band of metal nanoparticle surfaces to those in the conduction band of TiO_2 nanomaterials in metal-TiO_2 nanocomposites.(iv) Altering the charge-transfer properties between TiO_2 and the surrounding environment through modification of the TiO_2 nanomaterials surface with other semiconductors.

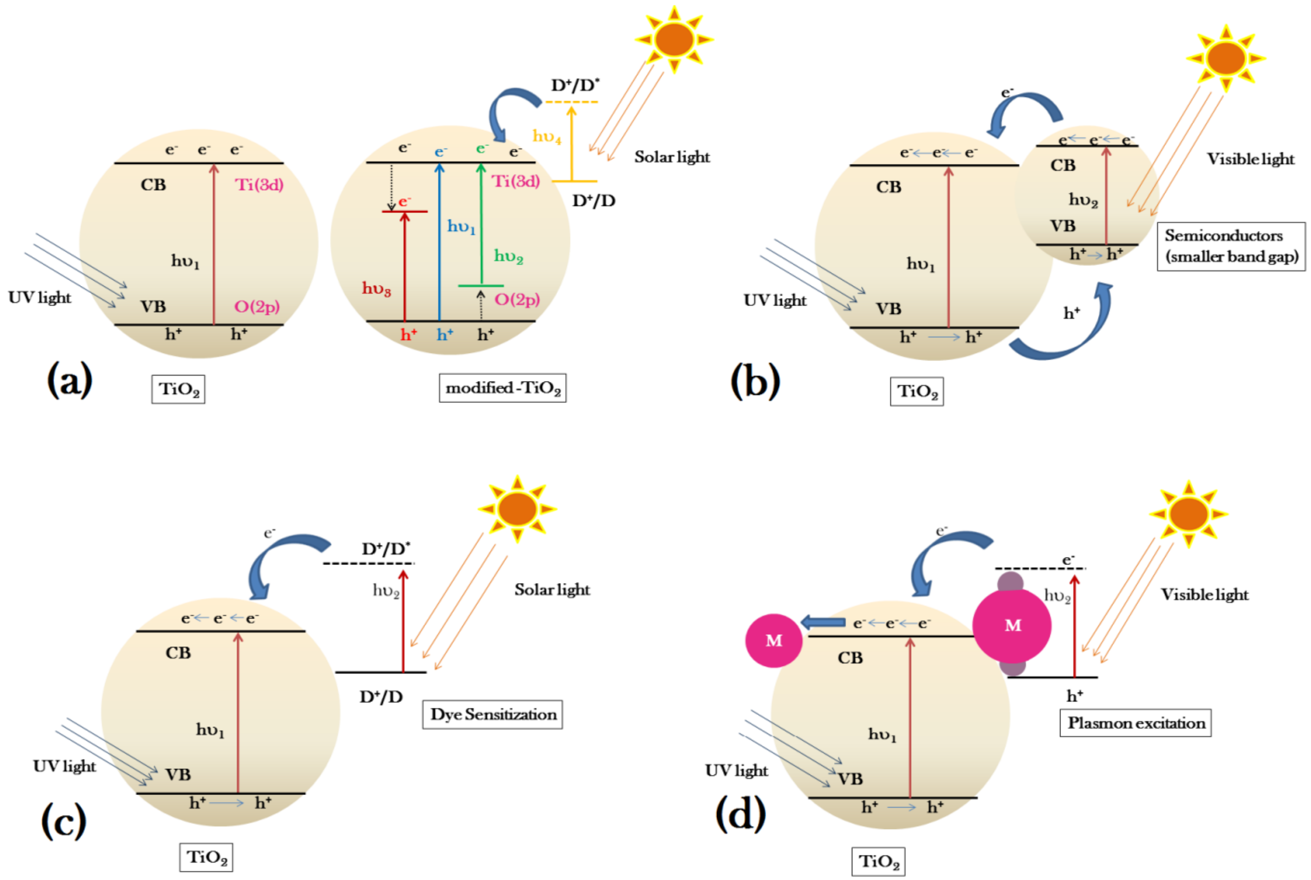

Figure 1.6: *Schematic representation of energy levels in (a) pure* TiO_2 *and modified* TiO_2; $h\upsilon_1$ – *pure* TiO_2, $h\upsilon_2$ – *non-metal doping,* $h\upsilon_3$ – *metal* TiO_2, $h\upsilon_4$ – *dye sensitization (b) doping (c) dye sensitization (d) noble metals coupling.*

1.5 TiO_2 Nanocomposites

The term nanocomposites broadly refers to the combination of large variety of systems such as one-dimensional, two-dimensional, three-dimensional and amorphous materials, made of distinctly dissimilar components at nanoscale regime. The general class of nanocomposite organic/inorganic materials is a vastly studied area of research. The properties of nano-composite materials depend not only on the properties of their individual parents but also on their morphology and interfacial characteristics. There is high possibility of unique properties which are unknown in the parent constituent materials to arise in their nanocomposites. Nanocomposite materials can be classified, according to their matrix materials, in three different categories: - Ceramic Matrix Nanocomposites (CMNC), Metal Matrix Nanocomposites (MMNC) and Polymer Matrix Nanocomposites (PMNC).

TiO_2 when coupled to a narrow-gap semiconductor material can result in an increase in photocatalytic reactivity and photoresponse. In such cases it is possible to create solid–solid interfaces between TiO_2 and other metals/semiconductor compounds. In such composites, on illumination, reactive electrons travel through the semiconductor to produce a response in TiO_2. The geometry of particles, surface texture and particle size play a significant role in interparticle electron transfer. Appropriate positioning and thickness of the introduced material results in enhanced charge transfer. This process extends the photoresponse of the TiO_2 to visible light wavelengths. Different materials are coupled with TiO_2, common semiconductors and metal oxides coupled to TiO_2 include: CdS, WO_3 and $Cs_xH_{3-x}PW_{12}O_{40}$[51,52,53,54]. Besides, metal oxides ZnO, MnO_2 and In_2O_3, when coupled to TiO_2 nanoparticles, have also been shown to increase the photocatalytic capability of TiO_2 nanoparticles[55,56,57].Semiconductor-semiconductor or semiconductor-metal composite nanoparticles facilitate charge rectification in these systems. Noble metal when deposited on semiconductor nanoparticles maximizes the efficiency of photocatalytic reactions. The noble metal acts as a sink for photoinduced charge carriers, promoting interfacial charge-transfer processes. Studies with regard to TiO_2–metal nanocomposites involving different materials (Au,Ag,Pt) revealed that these metal domains induces charge equilibrium in photoexcited TiO_2 nanocrystals affecting the energetics of nanocomposites by shifting the Fermi level to more negative potentials [58,59,60,61]. This corresponding shift in the nanocomposites is indicative of improved charge separation in TiO_2 metal systems and is effective towards enhanced photocatalysis[62,63].

Polymer nanocomposites have attracted great deal of scientific attention because of their significant enhancement in mechanical strength and thermal properties at low filler contents. Unique characteristics of the nanofillers endow these polymers with improved properties. To obtain nanocomposites with enhanced performance, nanoparticles are dispersed as nanopowders to promote a strong interface adhesion between matrix and nanofillers. The choice of the polymers is usually determined mainly by their mechanical, thermal, electrical, optical and magnetic behaviours. Other properties such as hydrophobic/hydrophilic balance, chemical stability, bio-compatibility, opto-electronic properties and chemical functionalities (i.e., solvation, wettability, templating effect etc) also should be considered in the choice of the polymers. Employing polymers allow easier shaping and better processing of the composite materials. Functionalizing TiO_2 nanoparticles with polymers having good conducting properties can be used to direct the charged electrons and electropositive holes away from the surface of TiO_2. TiO_2 nanoparticles when embedded in polymers, leads to charge segregation and hence reduced charge recombination[64]. Multitude of polymer/TiO_2 nanocomposites have been investigated for their improved properties such as polypyrrole, kaolinite, polyaniline, poly amide and poly-lactic acid (PLA)[65,66,67].

1.6 Applications of TiO_2

The applications of TiO_2 photocatalysts can be categorized into two areas: (i) Environmental remedy and (ii) Solar fuels applications. Some of its important applications are listed below:

Electrochromic Devices: Electrochromic windows and displays can be fabricated using TiO_2 in its nano form[68,69,70,71,72,73,74]. Electrochromism can be defined as the ability of a material to undergo colour change upon oxidation or reduction[75,76,77,78,79]. Electrochromic devices can vary their throughput of visible light and solar radiation upon electrical charging and discharging using a low voltage. A small voltage applied to the windows will cause them to darken and reversing the voltage causes them to lighten. Thus, it is possible to regulate the amount of energy entering through a “smart window” without the need of a curtain or shutter. Schematic representation of such devices is shown in figure 1.7. In the case of electrochromic information display an electrochromic layer is placed in front of a diffuse scattering pigmented surface. It is possible to achieve exceptional viewing properties with better contrast especially at off–normal angles than in the conventional LCDs. The origin of electrochromism lies in the electronic configuration of the semiconductor. If the band gap is larger than the energy of incoming radiation, the oxide is transparent. The metal ion of such a material can be reduced by the insertion of electrons and the Fermi level will shift into the next higher band, so that the material will start to interact with the incoming radiation and become absorbing. The redox potential of that molecule should lie above the conduction band edge. The process can be reversed by the application of a positive potential to the conductive substrate.

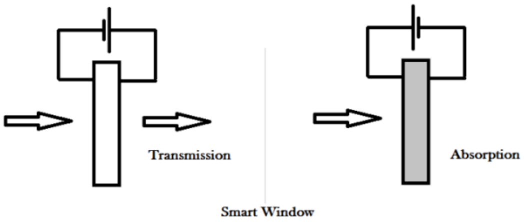

Figure 1.7: *Schematic sketch of an electrochromic device: smart window. Arrows indicate incoming and outgoing electromagnetic radiation.*

Sensing Applications: TiO_2 nanocrystalline films have been widely studied as sensors for various gases[80,81,82,83]. In addition to the conductivity change of gas-sensing material, the detection process can be performed by measuring the change of capacitance, work function, mass, optical characteristics or reaction energy released by the gas/solid interaction. Grimes et al. have found that TiO_2 nanotubes can perform exceptionally well as room-temperature hydrogen sensors not only with a high sensitivity of 10^4 but also with an ability to self-clean photoactively after environmental contamination[84].

Photovoltaic Applications: The conversion of light into electricity in a sensitized solar cell was reported in 1972[85]. A breakthrough in the efficiency from 1-2.5% to 7.1-7.9% was reported in 1991[86]. The cell was based on a film of nanostructured TiO_2 sensitized with a ruthenium complex as dye and with an organic electrolyte under simulated solar light illumination. Since then, lot of research has been carried out on improving the performance of DSSCs (Dye Sensitised Solar Cells) in terms of both higher energy conversion efficiency and higher stability.

Photocatalytic Properties: TiO_2 is regarded as the most efficient and environment friendly photocatalyst and it has been mostly used for photocatalytic toxic pollutant decomposing[87,88,89,90]. When photons with energy larger than the band gap of TiO_2 are incident, electrons are excited from the valence band to the conduction band, creating electron hole pairs as shown in figure 1.8. These charge carriers then migrate to the surface and react with the chemicals adsorbed on the surface to decompose the chemicals. This photodecomposition process usually involves one or more radicals or intermediate species such as •OH, O^{2-}, H_2O_2 or O_2, which play important roles in the photocatalytic reaction mechanisms. These •OH radicals and ions are able to virtually oxidize all organic materials to CO_2 and H_2O. The photocatalytic activity of a semiconductor is largely controlled by (i) the light absorption properties (ii) reduction and oxidation rates on the surface by the electron and hole and (iii) the electron hole recombination rate. A large surface area with a constant surface density of adsorbents and better crystalline property of the material leads to faster catalytic rates[91,92,93].

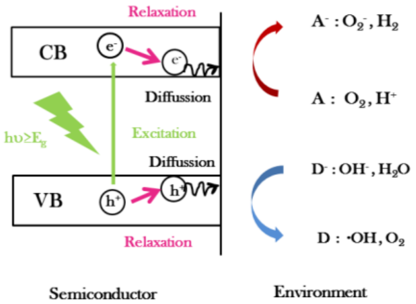

Figure 1.8: *Schematic representation of photo-induced processes at a TiO_2 semiconductor/electrolyte interface. Light excites electrons from valence band to conduction band. Electrons and holes react with environment acceptor (A) and/ donor (D).*

Water Splitting: In 1972, Fujishima and Honda discovered the phenomenon of photocatalytic splitting of water on TiO_2 electrode under ultraviolet (UV) light[94]. TiO_2 nanotube arrays are considered good candidates for efficient water splitting. When the TiO_2 photoanode is immersed in water and exposed to light irradiation, it absorbs photon energy corresponding to its band gap energy resulting in the generation of electron-hole pairs. The generated holes oxidize O^{2-} ions from absorbed water and produce oxygen gas and an electric current that moves through the external circuit to the conducting cathode reduces H^+ ions to produce hydrogen gas. Generally, the hydrogen production rate depends on the electrolyte, external bias, light intensity, TiO_2 morphology and structure. A proper optimisation of the above parameters can result in highly efficient cell for hydrogen generation.

Pigments: Titanium dioxide besides having high refractive index also has the ability to reflect and scatter the light in the visible spectrum[95]. Hence when it is divulged in paints, plastics or papers it imparts them brilliance and opacity. Unlike its convention counterpart lead (Pb), which is highly poisonous, TiO_2 is non-poisonous, non-toxic and biologically inert.

Antimicrobial effect: Among different materials which have found to inhibit the phenomenon of biofouling , TiO_2 has proved to be the most preferable due to its high stability, non-toxicity, photo sensitivity and antimicrobial activity[96,97].Under UV light, electrons are excited from valence-band to conduction-band leaving behind holes in valence-band. This generated positive hole in reaction with hydroxyl ions (OH^-) in water, produces hydroxyl radicals (HO•) which is more reactive than chlorine in disinfecting[98,99].

1.7 TiO_2 in Dye Sensitised Solar Cells

In the report “Top ten problems of humanity for next 50 years” by Richard .E Smalley renowned Nobel Prize winner (1996) for the discovery of new form of carbon, *energy* and *environment* bags the top and fourth positions respectively[85]. Constantly growing human population and ever-evolving high quality living standards, demands the availability of more energy. It is expected that worldwide power consumption would double within the next 30 years[100].The increasing energy demand, environmental issues such as greenhouse effect, pollution and approaching exhaustion of conventional energy sources have forced us to look for more environmental friendly, economically viable energy sources. The most appropriate unrivalled solution for such a crisis would be harnessing of different renewable energy resources. Among the different alternate power sources available such as nuclear, hydroelectric, geothermal, wind, biomass and solar, solar energy has the greatest potential. Several of the alternate energy sources used today is indirectly derived from solar energy. The sun provides the earth with approximately 100,000 TW which is almost 10,000 times more than the current energy consumption[99]. The solar cell, that is currently made available having significant stake in the energy market, is based on crystalline silicon and was first reported by Chapin et al. in 1954[101]. From then on extensive research investigations have led to increase in its efficiency, while trying to decrease the production cost. But it is still too expensive to be able to completely replace the conventional energy sources. This has steered a great research interest in the scientific world to find innovative ways of utilizing the solar energy with cheaper and more efficient methods. From the decade long study, Dye Sensitised Solar Cells (DSSCs), belonging to the third generation solar cells have emerged as the undisputed candidate among the different photovoltaic cells. Unlike the previous semiconductor devices, they do not rely on the conventional p-n heterojunction to separate photogenerated charge carriers. Here, they form a bulky junction, where charge separation takes place. These solar cells mainly require low-cost, non-toxic materials and facile fabrication processes and hence they tend to be a promising contender to the silicon based cells in the photovoltaic technology. Since then photovoltaics based on TiO_2 nanocrystalline electrodes have been widely studied. From the year 1985 to 2013, more than 11000 documents have been published in the field of Dye sensitised solar cells[102]. Figure 1.9 represents number of scientific documents published per year in the field of dye sensitised solar cells.

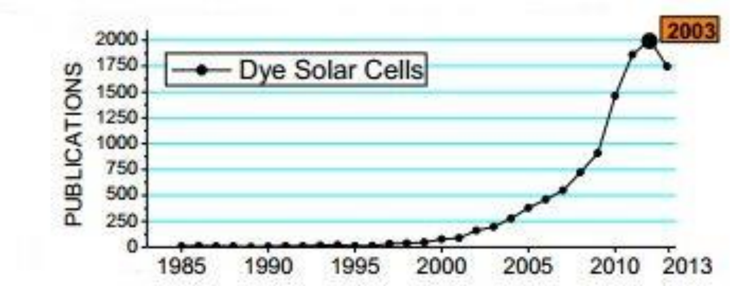

Figure 1.9: *Number of scientific documents published per year in the field of dye solar cell. Data were obtained from keyword search dye solar cell in the Scopus database.*

An extended schematic presentation of the structure and operating principles of the Dye Sensitised Solar Cells (DSSCs) is given in figure 1.10.

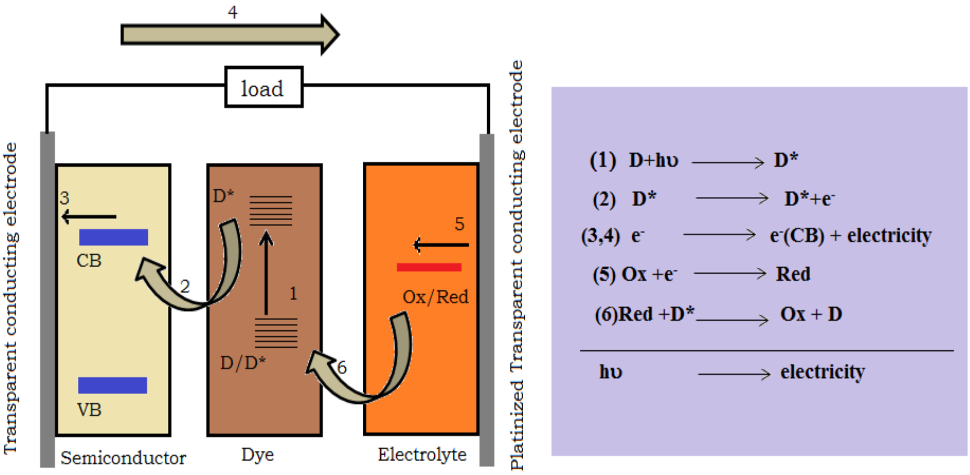

Figure 1.10: *Schematic representation of a typical Dye Sensitised Solar Cell.*

TiO_2 layer is deposited on a conductive ITO (Indium-tin-oxide) glass. The dye is placed over this semiconductor film, in contact with an electrolyte comprising of a redox couple. The excitation of the dye upon irradiation is followed by injection of the resulting electrons into the CB of the semiconductor, from where they reach the cell anode. Regeneration of “dye electrons” occurs through donation from the redox electrolyte in contact with the dye. Mostly used electrolyte is an organic solvent containing iodide/triiodide (I^{3-}/I^{-}) couple. Tri-iodide is reduced at the counter electrode and the resulting electron migrates from the anode to the counter electrode completing the circuit. The voltage generated is equal to the difference between the Fermi level of the electron in the solid TiO_2 and the redox potential of the electrolyte. The redox couple in the electrolyte should junction well such that the electron transfer from nanocrystalline TiO_2 to redox couple is slower than that from the counter electrode[103]. I^{3-}/I^- electrolyte very well satisfies the above essential condition and hence is considered to be the most favourable choice. The I^{3-}/I^- couple potential determines the thermodynamic driving force for the electron transfer from I^- to the oxidised dye. Finally, the mechanism of electron transfer from TiO_2 to I^{3-} is preceded by a weak dissociative chemisorption of iodine on TiO_2.The basic origin for the photovoltage is the change in the electron concentration in the nanocrystalline electron conductor that results from photoinduced charge injection from the dye. Photovoltage is determined by photoinduced chemical potential gradients and not by equilibrium electric fields[104].

DSSCs have gained considerable interest from the commercial aspect as well, such that large companies such as Sony, BASF and Samsung have invested for solar cell based studies in their own research. Also, new companies such as Dyesol (Australia), Solaronix (Switzerland) and G24i (Wales) have emerged with the main focus on the DSSC technology itself.

1.7.1 Merits of DSSCs

DSSCs are the most efficient third-generation solar cells as it possesses various important advantages over other p-n junction type solar cells such as;

- Injection process in a DSSC occurs through electrons. As a result DSSC works in low-light conditions such as cloudy skies or non-direct sunlight.
- Materials of lower purity can be used in DSSC and the fabrication processes are relatively simple and inexpensive.
- The operation of DSSC is independent of temperature.
- The Ruthenium (Ru) dye can experience 10^7 to 10^8 cycles without much decomposition, corresponding to a lifetime of 10 to 20 years under full sunlight[105,106].
- The materials used in DSSCs are environmental-friendly.
- Novel architectures with aesthetic appearance can be constructed, such as flexible sheets and flexible photovoltaic fibres. Some of the novel ideas using these cells are shown in the figure 1.11.

Figure 1.11: *Examples of DSSC Applications a) flexible DSSC-based solar module developed by Dyesol b) solar powered windows by Sony c) solar lanterns by Sony d) solar jacket commercialized by G24i e) solar travel bags by G24i.*

1.8 Nonlinear Optics

Nonlinear optics (NLO) impacts a wide range of technical fields, including optical communications, fiber optics, ultrafast lasers, quantum computing, ultra-cold atoms, plasma physics, particle accelerators, all-optical devices etc.[107]. These applications are essentially based on the non-linear optical properties of materials, i.e. changes in the refractive index of the material caused by an intense optical beam or by an external applied electric field. These effects become more pronounced in band gap engineered materials. As the dimension of the particle scales down from bulk three dimensional to zero dimensional, the ratio of index change to applied field in the active volume is increased. When intense light beam enters a transparent material, its susceptibility can become nonlinear[108]. It is generally expressed as Taylor's expansion in terms of the oscillating optical electric field

$$\chi(E) = \chi^{(1)} + \chi^{(2)}E + \chi^{(3)}E^2 + \chi^{(4)}E^3 \tag{1.1}$$

Non linearity is exhibited in the polarisation of the material as

$$P(E) = \varepsilon_0\chi^{(1)}E + \varepsilon_0\chi^{(2)}E^2 + \varepsilon_0\chi^{(3)}E^3 \tag{1.2}$$

All higher orders beyond $\chi^{(1)}$ represents the nonlinear response of a material in the presence of an intense light. The higher order terms become negligible as the intensity of the incident beam decreases. The two lowest order nonlinear responses are expressed by the second and third order nonlinear susceptibilities $\chi^{(2)}$ and $\chi^{(3)}$. Hence, the order of nonlinearity is classified as per the power of the intensity involved. In simple terms if we say, nth harmonic generation is an nth-order nonlinear effect and the optical Kerr effect is a third-order effect. Some of the NLO effects are listed in table 1.2[109].

NLO effect	Order
n^{th} harmonic generation	n
Sum and difference frequency generation	2
Raman scattering	2
n-photon absorption	n
Intensity dependent refraction	2,3
Induced opacity	2
Induced reflectivity	2
n wave mixing	n-1

Table 1.2: *Examples of Some NLO effects.*

Third order optical nonlinearities hold a significant stand in non-linear optics. Here, the polarization is proportional to third order in the electric field: $P(E)_3 = \varepsilon_0(\chi^{(3)}E^2)E.$ This leads to a polarization oscillating at the third harmonic, and also to a term in which the factor $(\chi^{(3)}E^2)$ has no oscillation frequency; this term oscillates at the fundamental frequency of the incident light. Thus the third-order nonlinearity causes both third harmonic generation (THG) and also an intensity-dependent change in the refractive index, which becomes nonlinear, n(I). The third-order term does not require a material with a centre of inversion symmetry. All materials have third order nonlinear susceptibility. The advancements in photonic switching and information processing will depend critically on the developments of improved photonic materials showing enhanced nonlinear properties. Choice of suitable nonlinear material depends on various factors such as the application (e.g. generation of a frequency or all-optical switching), the characteristics of the device (e.g. dimension, geometry, acceptable loss, response time, and non-linear conversion efficiency), and the operation conditions (e.g. wavelength, power, and CW or pulse)[110].

TiO_2 is considered as a promising but yet unexplored material for ultrafast, on-chip nonlinear optical devices. Its large nonlinear index of refraction is 30 times that of standard silica optical fiber[111]. Its high linear index of refraction and large Kerr nonlinearity can enhance optical confinement down to nano-scale dimensions.TiO_2 is highly transparent with no linear absorption in the visible range and no two photon absorption at higher wavelength>800nm.These properties makes it to surpass other transparent materials such as fused silica, SiN, diamond.

1.8.1 Optical Kerr Effect

The optical Kerr effect (OKE) can be defined as either light induced double refraction or an intensity-dependent refractive index. Here, the birefringence induced by a strong polarized laser beam is proportional to the square of the optical field. The intensity-dependent refractive index of the OKE is usually expressed as Eq 1.3: where n_o is the linear refractive index in the low light intensity regime and n, is the nonlinear refractive index.

$$n(I) = n_0 + n_2 I \qquad (1.3)$$

n_2 and $\chi^{(3)}$ are related by Eq (1.4), where both n_2 and $\chi^{(3)}$ are in esu and c is the speed of light.

$$n_2 = \frac{16\pi^2 \chi^{(3)}}{c n_0^2} \qquad (1.4)$$

1.8.2 Saturable Absorption

After absorbing a quantum of radiation, an atom requires a certain average time to return to its initial state. During this time period, that atom can no longer absorb light. If the radiation is intense enough, the absorption of the entire medium can be saturated. Such a phenomenon is called saturable absorption. Saturable absorption induces change in the absorption constant proportional to the pump intensity. In saturation spectroscopy, the saturation results in an additional transmitted amplitude which is proportional to the product of the pump intensity and the probe amplitude. The intensity-dependent absorption coefficient $\alpha(I)$ is related to the saturation intensity I_s, by Eq. 1.5 where τ is the lifetime for the return of the population to the ground state (in a simple two-level system it is equal to the lifetime of the excited state), $\Delta E = h\upsilon$ is the energy difference between the ground state and the excited state, and σ is the absorption cross section of the ground state. I_s can be defined as the intensity required to reduce the absorption α_0 to one half of the linear absorption (in the low intensity regime).

$$\alpha(I) = \frac{\alpha_0}{1+{}^{I}/_{I_s}}\,; I_s = \frac{\Delta E}{\sigma\tau} \qquad (1.5)$$

One of the important applications of saturable absorption is in the field of volatile computer memory, the dynamic random access memory (DRAM), for which refresh period depends upon the time taken for excited electrons to relax back to the ground state.

1.8.3 Two Photon Absorption

Two photon absorption (TPA) refers to the process in which two photons of identical or different frequencies are absorbed simultaneously such that the molecule from one stable state will be excited from lower state to the excited state. Schematic representation of TPA is shown in figure 1.12. TPA can be classified into two types: resonant TPA and non-resonant TPA. The non-resonant TPA refers to the process in which two photons combine to channel through an energy gap which is larger than the energies of individual photons. Here, it is not necessary that an intermediate state will be present between the lower and the excited state. It can be visualised as if moving up two stair step at a time. The nonlinear absorption in this case is proportional to the square of the instantaneous intensity and is given as[112]

$$\frac{dI}{dz} = -\alpha I - \beta I^2 \tag{1.6}$$

where α is the linear absorption coefficient and β is the two photon absorption coefficient.

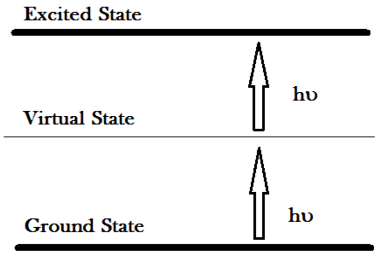

Figure 1.12: *Schematic diagram of two photon absorption.*

When there is an intermediate state in the gap, the transition occurs through two separate one photon transitions and the process is known as resonant TPA.

1.8.4 Excited State Absorption

In certain materials such as polyatomic molecules and semiconductors, nonlinear effects arises by means of redistribution of population densities of two or more excited states via absorption, both via successive linear and nonlinear absorption processes. Linear absorption can promote species to excited states that serve as the lower state of a second electric dipole allowed transition before the excited state electrons decay back to the ground state. There might be number of higher lying states that are radiatively coupled to these intermediate states, for which the energy differences are in near-resonance with the incident photon energy. Hence excited state absorption involves promotion of photons to higher lying states before relaxing back to the ground state.

1.8.5 Multiphoton Absorption

Multiphoton absorption refers to the simultaneous absorption of n photons from a single beam or multiple beams. The absorption of (n+1) photons from a single optical beam is given by

$$\frac{dI}{dz} = -(\alpha + \gamma^{n+1} I^{n})I \tag{1.7}$$

where γ^{n+1} is the n+1 photon absorption coefficient.

1.8.6 Free Carrier Absorption (FCA)

In the case of semiconductors the absorption of a photon with energy greater than the bandgap will excite the electron to the conduction band, where it is a free carrier and can contribute current flow when a field is applied. The excited electron will then rapidly thermalize and relax to the bottom of the conduction band. From there it will recombine with an excited hole in the valence band after a characteristic recombination time. But, at sufficiently high intensities, it can absorb another photon while it is still in the conduction band. This process is called free carrier absorption.

In the weak absorption regime, the attenuation may be described by[113]

$$\frac{dI}{dz} = -\alpha I - \sigma_c N_c(I)I \tag{1.8}$$

where N_c (I) is the intensity dependent carrier density and σ_c is the free carrier absorption cross section.

1.8.7 Optical Limiting

Optical limiters are devices that transmit light at low input fluences and become opaque at higher intensities. They are of special concern in nonlinear optics and optoelectronics for their possible application in the protection of eyes and sensitive detectors against intense radiation[114]. Their optical limiting characteristics can be analysed by estimating the imaginary part of susceptibility. The most desirable attribute of an ideal optical limiter is low threshold. An ideal optical limiter has linear transmission up to the threshold input fluence after which the transmittance remains constant. Optical limiting behaviour is analysed by measuring the nonlinear transmittance as a function of input fluence as represented in figure 1.13. From the value of fluence at the focus, fluence at other positions can be calculated using the standard equation for Guassian beam waist given as,

$$\omega^2(z) = \omega_0^2(1 + z^2/z_0^2) \qquad (1.9)$$

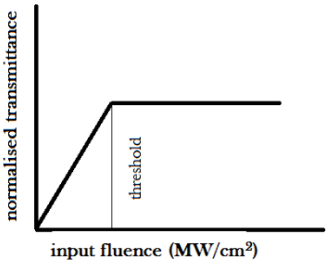

Figure 1.13: *Ideal optical limiting curve.*

1.8.8 Physical Origin of Optical Nonlinearity

The origin of optical non linearity can be classified as either structural or compositional. Structural refers to light-induced structure changes, such as the change of electronic density, average interatomic distances, molecular orientation, phase transition, etc. A light-induced chemical composition change consists essentially of light-induced chemical reactions such as molecular dissociation, polymerization and transformation. It can be reversible or permanent. At resonance, intense light intensity can induce distribution of electrons at different electronic states whereas at off resonance it can lead to distortion of electronic clouds. It gives the fastest response time. Besides electronic non linearity thermal non linearity also gives rise to high optical non linearity. Thermal non linearity is the driving principle for temperature sensors. It arises due to the generation of phonons on intense light irradiation.

1.9 Scope of the Thesis

Till now, exceptionally large number of fundamental studies and application-oriented research and developments has been carried out by many researchers worldwide in TiO_2 with its low-dimensional nanomaterial form due to its various novel properties. These nanostructured materials have shown many favourable properties for potential applications, including pollutant photocatalytic decomposition, photovoltaic cells, sensors and so on. This thesis aims to make an in-depth investigation on different linear and nonlinear optical and structural characteristics of different phases of TiO_2. Correspondingly, extensive challenges to synthesise different high quality TiO_2 nanostructure derivatives such as nanotubes, nanospheres, nanoflowers etc. are continuing. Here, different nanostructures of anatase TiO_2 were synthesised and analysed. Morphologically different nanostructures were found to have different impact on their physical and electronic properties such as varied surface area, dissimilar quantum confinement and hence diverged suitability for different applications. In view of the advantages of $TiO_{2,}$ it can act as an excellent matrix for nanoparticle composite films. These composite films may lead to several advantageous functional optical characteristics. Detailed investigations of these kinds of nanocomposites were also performed, only to find that these nanocomposites showed higher adeptness than their parent material. Fine tuning of these parameters helps researchers to achieve high proficiency in their respective applications. These innumerable opportunities aims to encompass the new progress in studies related to TiO_2 for an efficient utilization in photo-catalytic or photo-voltaic applications under visible light, accentuate the future trends of TiO_2-research in the environment as well as energy related fields serving promising applications benefitting the mankind. The last section of the thesis discusses the applicability of analysed nanomaterials for dye sensitised solar cells followed by future suggestions.

1.10 Conclusions

This chapter briefly presents the various properties of TiO_2 and its implementation with regard to recent trends and requirements. The distinctiveness of TiO_2 with respect to its structural, electronic and optical properties has been reviewed. Recent trends on the novel applications of TiO_2 are also discussed in detail. The last section of the chapter discusses the scope of the present thesis.

1.11 References

---

[1] Wu, N. L., Lee, M. S., Pon, Z. J., & Hsu, J. Z. (2004). “Effect of calcination atmosphere on TiO_2 photocatalysis in hydrogen production from methanol/water solution”. *J. Photochem. Photobiol.,A*, 163(1), 277-280.

[2] A. Fujishima and K. Honda, “Photolysis-decomposition of water at the surface of an irradiated semiconductor”. *Nature*, 1972, 238, 37–38.

[3] K.Nakata and A. Fujishima.(2012). “TiO_2 photocatalysis:design and applications”. *Photochem. Photobiol., A*, 13, 169–189.

---

[4] X. Su, L. Wu, X. Zhan, J. Wu, Y. Wei and Z. Guo. (2012) “Advanced titania nanostructures and composites for lithium ion battery”. *J. Mater. Sci.*, 47, 2519–2534.

[5] D.P.Macwan, P.N.Dave and S.Chaturvedi, (2011)“A review on nano-TiO_2 sol–gel type syntheses and its applications”. *J. Mater. Sci.*, 46, 3669–3686.

[6] Hua Xu, Shuxin Ouyang, Lequan Liu, Pakpoom Reunchan, Naoto Umezawaace and Jinhua Ye.(2014)“ Recent advances in TiO_2-based photocatalysis”. *J. Mater. Chem. A*,2, 12642-12661.

[7] M. Kagata, Y. Abe, “Dielectric properties of sintered TiO_2 and TiO_2-WO3 mixtures”, CARTS USA 2006, Digital Library, http://ecadigitallibrary.com/ pdf/CARTS 06/7_3 swq

[8] Lee, M. K., Lee, H. C., & Hsu, C. M. (2007). “High dielectric constant TiO_2 film grown on polysilicon by liquid phase deposition”. *Mater. Sci. Semicond. Process.*, *10*(2), 61-67.

[9] Pomoni, K., Vomvas, A., & Trapalis, C. (2008). “Electrical conductivity and photoconductivity studies of TiO_2 sol–gel thin films and the effect of N-doping”. *J. Non-Cryst. Solids*, *354*(35), 4448-4457.

[10] Fujishima, A. (1972). “ Electrochemical photolysis of water at a semiconductor electrode”. *Nature*, *238*, 37-38.

[11] Lee S, Park BH, Oh SG 1997 “In-situ ellipsometric investigation of TiO_2 thin-film initial growth”. J. Korean Phys. Soc.;31(2):352–356.

[12] AJ Thelen, “Design of Optical Interference Coatings ”. (McGraw-Hill, New York, 1989)

[13] MacLeod HA. Thin-Film Optical Filters. Bristol, UK: Adam Hiliger Ltd; 2001.

[14] Karthik, K., S. Kesava Pandian, and N. Victor Jaya. (2010) “Effect of nickel doping on structural, optical and electrical properties of TiO_2 nanoparticles by sol–gel method”. *Appl. Surf. Sci* 256(22): 6829-6833.

[15] O. Carp, C.L. Huisman, A. Reller (2004) “Photoinduced reactivity of titanium dioxide”.*Prog. Solid State Chem.*, 32, 33–177.

[16] Huber, B., Brodyanski, A., Scheib, M., Orendorz, A., Ziegler, C., & Gnaser, H. (2005).“Nanocrystalline anatase TiO_2 thin films: preparation and crystallite size-dependent properties”. *Thin Solid Films*, *472*(1), 114-124.

[17] http://www.geocities.jp/ohba_lab_ob_page/structure6.html

[18] Haines, J., & Leger, J. M. (1993). “ X-ray diffraction study of TiO_2 up to 49 GPa”. *Physica B*, *192*(3), 233-237.

[19] Horn M, Schwerdtfeger CF, Meagher EP.(1972)“Refinement of the structure of anatase at several temperatures”. *Z Kristallogr.* 36:273–281.

[20] Banerjee, A. N. (2011). “The design, fabrication, and photocatalytic utility of nanostructured semiconductors: focus on TiO_2-based nanostructures”. *Nanotechnol. Sci. Appl., 4,* 35.

[21] Divya, S., Sebastian, I., Nampoori, V. P. N., Radhakrishnan, P., & Mujeeb, A. (2014). “Non resonant excitonic effects on the third order nonlinear properties of TiO_2: From amorphous to rutile phase”. *Opt. Laser Technol., 56*, 207-210.

[22]Zhang, H.; Banfield, J. F. (1998). “Thermodynamic analysis of phase stability of nanocrystalline titania”. *J. Mater. Chem., 8*(9), 2073-2076.

[23] Zhang, H.; Banfield, J. F. (2000) “Understanding polymorphic phase transformation behavior during growth of nanocrystalline aggregates: Insights from TiO_2”. *J. Phys. Chem. B*, 104, 3481-3487.

[24] Ardakani, H. K. (1994). “Electrical and optical properties of in situ hydrogen-reduced titanium dioxide thin films deposited by pulsed excimer laser ablation”. *Thin Solid Films, 248*(2), 234-239.

[25]. Paxton, A. T., & Thien-Nga, L. (1998). “Electronic structure of reduced titanium dioxide”. *Phys. Rev. B: Condens. Matter, 57*(3), 1579”.

[26] Bally A. (1999) “Electronic Properties of Nanocrystalline Titanium Dioxide Thin Films”. Lausanne, France: Département de physique, *Ecole polytechnique fédérale de Lausanne EPFL*;.

[27] Springer S. (2004) “Free carriers in nanocrystalline titanium dioxide thin films”. Ecole polytechnique fédérale de Lausanne EPFL. Lausanne;: Thèse no: 2934.

[28] Tang, H., Prasad, K., Sanjines, R., Schmid, P. E., & Levy, F. (1994). “Electrical and optical properties of TiO_2 anatase thin films”. *J. Appl. Phys*, *75*(4), 2042-2047.

[29] Mo, S. D., & Ching, W. Y. (1995). “Electronic and optical properties of three phases of titanium dioxide: rutile, anatase, and brookite”. *Phys. Rev. B: Condens. Matter, 51*(19), 13023.

[30] Straumanis, M. E., Ejima, T., & James, W. J. (1961). “The TiO_2 phase explored by the lattice constant and density method”. *Acta Crystallographica*, *14*(5), 493-497.

[31] Carnahan, R. D., & Brittain, J. O. (1965). “Optical absorption study of the reduction kinetics of rutile crystals”. *J. Am. Ceram. Soc., 48*(7), 365-369.

[32] Cronemeyer, D. C., & Gilleo, M. A. (1951). “The optical absorption and photoconductivity of Rutile”. *Phys. Rev., 82*(6), 975.

[33] Sekiya, T., Ichimura, K., Igarashi, M., & Kurita, S. (2000). “Absorption spectra of anatase TiO_2 single crystals heat-treated under oxygen atmosphere”. *J. Phys. Chem. Solids, 61*(8), 1237-1242.

[34] Cao, X., Lan, X., Guo, Y., Zhao, C., Han, S., Wang, J., & Zhao, Q. (2007). “Preparation and Characterization of Bifunctional ZnO/ZnS Nanoribbons Decorated by γ-Fe_2O_3 Clusters”. *J. Phys. Chem. C, 111*(51), 18958-18964.

[35] Cao, H., Wang, G., Zhang, S., & Zhang, X. (2006). “Growth and photoluminescence properties of PbS nanocubes”. *Nanotechnology, 17*(13), 3280.

[36] Can, X.Millstone, J. E.; Li, S. Y.Mirkin, C. A. (2007) *Angew.Chem., Int. Ed.*, 46, 8436–8439.

[37] Tian, Lu, Han Yao Tan, and Jagadese J. Vittal. (2007) “Morphology-controlled synthesis of Bi_2S_3 nanomaterials via single-and multiple-source approaches”. *Cryst. Growth Des.*, 8(2): 734-738.

[38] Davies, J. H., Long, A. R., “Eds.Physics of Nanostructures”; *Institute of Physics: Philadelphia*, PA, 1992.

[39] Norris, J. R., Jr., Meisel, D., “Eds.Photochemical Energy Conversion”; Elsevier: New York, 1989.

[40] Hagfeldt, A.; Gratzel, M. (1995) “Light-Induced Redox Reactions in Nanocrystalline Systems”. *Chem. Rev.*, 95,49-68.

[41] Wang, Y. 1991 “Nonlinear Optical Properties of Nanometer-Sized Seminconductor Clusters”. *Acc. Chem. Res*., 24(5), 133-139.

[42] Huo, K., Gao, B., Fu, J., Zhao, L., & Chu, P. K. (2014). “Fabrication, modification, and biomedical applications of anodized TiO_2 nanotube arrays”. *RSC Advances*, 4(33), 17300-17324.

[43] Kalyanasundaram, K. 1987 “Photochemistry in Microheterogeneous Systems”. Academic Press: New York,.

[44] Lewis. L. N. (1993) “Chemical Catalysis by Colloids and Clusters”. *Chem.Rev.*, 93, 2693-2730.

[45] Tyner, C. E. (1990). “Applications of Solar Thermal Technology to the Destruction of Hazardous Wastes”. *Sol. Energy Mater*.,21(2-3), 113-129

[46] Schiavello, M. “Photocatalysis and Environment: Trends and Applications”. Kluwer Academic: Boston, MA, 1987.

[47] Z.G. Zou, J.H. Ye, K. Sayama, H. Arakawa. (2001) “Direct splitting of water under visible light irradiation with an oxide semiconductor photocatalyst”. *Nature*, 414 625-627.

[48] X. Chen, Y. Lou, S. Dayal,X. Qiu, R. Krolicki, C. Burda, C. Zhao, J. Becker, (2005) “Doped semiconductor nanomaterials”. *J. Nanosci. Nanotechnol*. 5(9), 1408-1420,

[49] Burda, C,Lou, Y.Chen, X..Samia, A.C.S.Stout, J.;Gole,J.L. *(*2003) “Enhanced Nitrogen Doping inTiO_2Nanoparticles”. *Nano Lett.*,3(8), 1049-1051.

[50] Chen, X., Lou, Y., Samia, A. C., & Burda, C. (2003). “Coherency strain effects on the optical response of core/shell heteronanostructures”. *Nano Lett.*, *3*(6), 799-803.

[51] Zhu , J.H. , Yang , D.et al .(2008) “Synthesis and characterization of bamboo- like CdS/TiO_2 nanotubes composites with enhanced visible – light photocatalytic activity”. *J Nanopart. Res.* ,10 (5), 729 – 36 .

[52] Yang, H., Shi, R., Zhang, K., Hu, Y., Tang, A., & Li, X. (2005). “Synthesis of WO_3/TiO_2 nanocomposites via sol–gel method”. *J. Alloy Compd.*, 398(1), 200-202.

[53] Xiao, M., Wang, L., Huang, X., Wu, Y., & Dang, Z. (2009). “Synthesis and characterization of WO_3/titanate nanotubes nanocomposite with enhanced photocatalytic properties”. *J. Alloy Compd., 470*(1), 486-491.

[54] Yu, X., Guo, Y., Xu, L., Yang, X., & Guo, Y. (2008). “A novel preparation of mesoporous $Cs_xH_{3-x}PW_{12}O_{40}/TiO_2$ nanocomposites with enhanced photocatalytic activity”. *Colloid Surface A*, *316*(1), 110-118.

[55] Xue, M., Huang, L., Wang, J. Q., Wang, Y., Gao, L., Zhu, J. H., & Zou, Z. G. (2008). “The direct synthesis of mesoporous structured MnO_2/TiO_2 nanocomposite: a novel visible-light active photocatalyst with large pore size”. *Nanotechnology*, *19*(18), 185604.

[56] Wang, Q., Yang, D., Chen, D., Wang, Y., & Jiang, Z. (2007). “Synthesis of anatase titania-carbon nanotubes nanocomposites with enhanced photocatalytic activity through a nanocoating-hydrothermal process”. *J Nanopart. Res.*, *9*(6), 1087-1096.

[57] Shchukin, D., Poznyak, S., Kulak, A., & Pichat, P. (2004). "TiO_2-In_2O_3 photocatalysts: preparation, characterisations and activity for 2-chlorophenol degradation in water". *J. Photoch. Photobio A, 162*(2), 423-430.

[58] Chandrasekharan, N., & Kamat, P. V. (2000). "Improving the photoelectrochemical performance of nanostructured TiO_2 films by adsorption of gold nanoparticles". *J. Phys. Chem. B, 104*(46), 10851-10857.

[59] Pastoriza-Santos, I., Koktysh, D. S., Mamedov, A. A., Giersig, M., Kotov, N. A., & Liz-Marzán, L. M. (2000). " One-pot synthesis of Ag@ TiO_2 core-shell nanoparticles and their layer-by-layer assembly". *Langmuir, 16*(6), 2731-2735.

[60] Subramanian, V., Wolf, E., & Kamat, P. V. (2001). "Semiconductor-metal composite nanostructures. To what extent do metal nanoparticles improve the photocatalytic activity of TiO_2 films". *J. Phys. Chem. B, 105*(46), 11439-11446.

[61] Kraeutler, B., & Bard, A. J. (1978). "Heterogeneous photocatalytic preparation of supported catalysts. Photodeposition of platinum on titanium dioxide powder and other substrates". *J. Am. Chem. Soc, 100*(13), 4317-4318.

[62] Subramanian, V., Wolf, E. E., & Kamat, P. V. (2004). "Catalysis with TiO_2/gold nanocomposites. Effect of metal particle size on the Fermi level equilibration". *J. Am. Chem. Soc, 126*(15), 4943-4950.

[63] Jakob, M., Levanon, H., & Kamat, P. V. (2003). "Charge distribution between UV-irradiated TiO_2 and gold nanoparticles: determination of shift in the Fermi level". *Nano Lett., 3*(3), 353-358.

[64] Li, S., Chen, M., He, L., Xu, F., & Zhao, G. (2009). "Preparation and characterization of polypyrrole/TiO_2 nanocomposite and its photocatalytic activity under visible light irradiation". *J. Mater. Res., 24*(08), 2547-2554.

[65] Min, S. X., Wang, F., Zhang, Z. M., Han, Y. Q., & Feng, L. (2009). " Preparation and Photocatalytic Activity of PANI/AMTES-TiO_2 Nanocomposite Materials". *Acta Phys-Chim Sin, 25*(7), 1303-1310.

[66] Shaomin, L., Wenqi, G., Chunhua, B., Yi, Q., Yongqin, G., Bihua, X., & Cheng, W. (2006). "Preparation of TiO2/kaolinite nanocomposite and its photocatalytical activity". *J. Wuhan Univ. Technol., 21*(4), 12-15.

[67] Luo, Y. B., Li, W. D., Wang, X. L., Xu, D. Y., & Wang, Y. Z. (2009). "Preparation and properties of nanocomposites based on poly (lactic acid) and functionalized TiO_2". *Acta Mater., 57*(11), 3182-3191.

---

[68] Kamat, Prashant V. (2001) “Electrochromic and Photoelectro-chromic Aspects of Semiconductor Nanostructure-Molecular Assembly”. *Electrochem. Nanomater* 229.

[69] Pichot, F., Ferrere, S., Pitts, R. J., & Gregg, B. A. (1999). “Flexible Solid-State Photoelectrochromic Windows”. *J. Electrochem. Soc., 146*(11), 4324-4326.

[70] Aliev, A. E., and H. W. Shin. “Nanostructured materials for electrochromic devices”. *Solid State Ionics* 154 (2002): 425-431.

[71] Bach, U., Corr, D., Lupo, D., Pichot, F., & Ryan, M. (2002). “Nanomaterials-Based Electrochromics for Paper-Quality Displays”. *Adv. Mater, 14*(11), 845-848.

[72] Bonhote, P., Gogniat, E., Campus, F., Walder, L., & Grätzel, M. (1999). “Nanocrystalline electrochromic displays”. *Displays, 20*(3), 137-144.

[73] Bonhôte, P., Gogniat, E., Grätzel, M., & Ashrit, P. V. (1999). “Novel electrochromic devices based on complementary nanocrystalline $TiO_2$and WO_3 thin films”. *Thin Solid Films, 350*(1), 269-275.

[74] Campus, F., P. Bonhote, M. Grätzel, S. Heinen, and L. Walder. “Electrochromic devices based on surface-modified nanocrystalline TiO_2thin-film electrodes”. *Sol. Energy Mater. Sol. Cells* 56(3) (1999): 281-297.

[75] Choi, S. Y., Mamak, M., Coombs, N., Chopra, N., & Ozin, G. A. (2004). “Electrochromic performance of viologen-modified periodic mesoporous nanocrystalline anatase electrodes”. *Nano Lett, 4*(7), 1231-1235.

[76] Cinnsealach, R., Boschloo, G., Nagaraja Rao, S., & Fitzmaurice, D. (1999). “Coloured electrochromic windows based on nanostructured TiO_2films modified by adsorbed redox chromophores”. *Sol. Energy Mater. Sol. Cells, 57*(2), 107-125.

[77] Cummins, D., Boschloo, G., Ryan, M., Corr, D., Rao, S. N., & Fitzmaurice, D. (2000). “Ultrafast electrochromic windows based on redox-chromophore modified nanostructured semiconducting and conducting films”. *J. Phys. Chem. B, 104*(48), 11449-11459.

[78] Deb, S. K., Lee, S. H., Edwin Tracy, C., Roland Pitts, J., Gregg, B. A., & Branz, H. M. (2001). “Stand-alone photovoltaic-powered electrochromic smart window”. *Electrochim. Acta, 46*(13), 2125-2130.

[79] Garcia-Canadas, J.; Peter, L. M.; Upul Wijayantha, K. G. (2003).“Characterisation of electrochromic viologen-modified nanocrystalline TiO_2 films by frequency-resolved optical transmission spectroscopy”. *Electrochem. Commun.*, 5, 199.

[80] Benkstein, K. D., & Semancik, S. (2006). “Mesoporous nanoparticle TiO_2 thin films for conductometric gas sensing on microhotplate platforms”. *Sens. Actuators, B*, *113*(1), 445-453.

[81] Birkefeld, L. D., Azad, A. M., & Akbar, S. A. (1992). “Carbon monoxide and hydrogen detection by anatase modification of titanium dioxide”. *J. Am. Ceram. Soc.*, *75*(11), 2964-2968.

[82] Carney, C. M., Yoo, S., & Akbar, S. A. (2005). “TiO_2-SnO_2 nanostructures and their H_2 sensing behaviour”. *Sens. Actuators, B*, *108*(1), 29-33.

[83] Chow, L. L. W., Yuen, M. M. F., Chan, P. C. H., & Cheung, A. T. (2001). “Reactive sputtered TiO_2 thin film humidity sensor with negative substrate bias”. *Sens. Actuators, B*, *76*(1), 310-315.

[84] Gao, L., Li, Q., Song, Z., & Wang, J. (2000). “Preparation of nano-scale titania thick film and its oxygen sensitivity”. *Sens. Actuators, B*, *71*(3), 179-183.

[85] Tributsch,H .(1972).“Reaction of excited chlorophyll molecules at electrodes and in photosynthesis”. *Photochem. Photobiol.*, 16, 261-269.

[86] O'Regan, B.; Grätzel, M. (1991) “A low-cost, high-efficiency solar cell based on dye-sensitized colloidal TiO_2 films”. *Nature*, *353*,737-740.

[87] Tan, O. K., Cao, W., Zhu, W., Chai, J. W., & Pan, J. S. (2003). “Ethanol sensors based on nano-sized α-Fe_2O_3 with SnO_2-ZrO_2, TiO_2 solid solutions”. *Sens. Actuators, B*, *93*(1), 396-401.

[88] Tang, H.; Prasad, K.; Sanjines, R.; Levy, F. (1995) “TiO_2 anatase thin films as gas sensors” *Sens. Actuators B*, 26, 71

[89] C.C. Wang, Z. Zhang, and J. Y. Ying, (1997) “Photocatalytic Decomposition of Halogenated Organics over Nanocrystalline Titania”, *Nanostr. Mater.*, 9(1), 583-586.

[90] Wang, J., Wen, F. Y., Zhang, Z. H., Zhang, X. D., Pan, Z. J., Zhang, P., & Xu, L. (2006). “Investigation on degradation of dyestuff wastewater using visible light in the presence of a novel nano TiO_2 catalyst doped with upconversion luminescence agent”. *J. Photochem. Photobiol., A*, *180*(1), 189-195.

[91] Ivanković, S., Gotić, M., Jurin, M., & Musić, S. (2003). “Photokilling squamous carcinoma cells SCCVII with ultrafine particles of selected metal oxides”. *J. Sol-Gel Sci. Technol.*, *27*(2), 225-233.

[92] Sakai, H., Baba, R., Hashimoto, K., Kubota, Y., & Fujishima, A. (1995). “Selective killing of a single cancerous T24 cell with TiO_2 semiconducting microelectrode under irradiation”. *Chem. Lett*, (3), 185-186.

---

[93] Chen, X., & Mao, S. S. (2007). “Titanium dioxide nanomaterials: synthesis, properties, modifications, and applications”. *Chem. Rev.*, *107*(7), 2891-2959.

[94] Huber, B., Brodyanski, A., Scheib, M., Orendorz, A., Ziegler, C., & Gnaser, H. (2005). “Nanocrystalline anatase TiO_2 thin films: preparation and crystallite size-dependent properties”. *Thin Solid Films*, *472*(1), 114-124.

[95] Pfaff, G., & Reynders, P. (1999). “Angle-dependent optical effects deriving from submicron structures of films and pigments”. *Chem. Rev.*, *99*(7), 1963-1982.

[96] S. Sakthivel, M.V. Shankar & M.Palanichamy (2004). “Enhancement of photocatalytic activity by metal deposition: characterization and photonic efficiency of Pt, Au and Pd deposited on TiO_2 catalyst”. *Water Res.*, 38(13), 3001–3008.

[97] Colmenares, J. C., Aramendia, M. A., Marinas, A., Marinas, J. M., & Urbano, F. J. (2006). “Synthesis, characterization and photocatalytic activity of different metal-doped titania systems”. *Appl. Catal., A*, *306*, 120-127.

[98] M. De Kwaadsteniet, M. Botes & T.E. Cloete, (2011). “Application of nanotechnology in antimicrobial coatings in the water industry”. *Nano*, *6*(05), 395-407.

[99] Butterfield, I. M., Christensen, P. A., Curtis, T. P., & Gunlazuardi, J. (1997). “Water disinfection using an immobilised titanium dioxide film in a photochemical reactor with electric field enhancement”. *Water Res.*, *31*(3), 675-677.

[100] Grätzel, M. (2007). “Photovoltaic and photoelectrochemical conversion of solar energy”. *Philos. Trans. A Math Phys. Eng. Sci.*, 365(1853), 993-1005.

[101] Chapin, D. M., Fuller, C. S., & Pearson, G. L. (1954). “A new silicon p-n junction photocell for converting solar radiation into electrical power”. *J. Appl. Phys.*, 25(5), 676-677.

[102] Hinsch, A. *“Status of the dye solar cell technology (dsc) as a guideline for further research”.*

[103] Peter, L. M. (2007) “Characterization and modeling of dye-sensitized solar cells.” *J. Phys. Chem. C* 111(18): 6601-6612.

[104] Pichot, F., & Gregg, B. A. (2000). “The photovoltage-determining mechanism in dye-sensitized solar cells”. *J. Phys. Chem. B*, *104*(1), 6-10.

[105] Grätzel, M. (2000). “Perspectives for dye-sensitized nanocrystalline solar cells”. *Prog. Photovoltaics Res. Appl.*, 8(1), 171-185.

---

[106] Durrant, J. R., Nelson, J., & Klug, D. R. (2000). " Functionalising nanocrystalline TiO_2 films: dye sensitised solar cells and optical biosensors". *Mater. Sci. Technol.*, 16(11-12), 1345-1348.

[107] Divya, S., Nampoori, V. P. N., Radhakrishnan, P., & Mujeeb, A. (2014). "Evaluation of nonlinear optical parameters of TiN/PVA nanocomposite–A comparison between semi empirical relation and Z-scan results". *Curr. Appl. Phys.*, 14(1), 93-98.

[108] Sheik-Bahae,M.,& Hasselbeck, M. P. (2000)."Third-order optical nonlinearities". *Handbook of Optics*, 4,16-1.

[109] Nie, W. (1993). "Optical nonlinearity: phenomena, applications, and materials". *Adv. Mater., 5(7-8), 520-545.*

[110] Chakraborty, P. (1998). "Metal nanoclusters in glasses as non-linear photonic materials". *J. Mater. Sci.*, 33(9), 2235-2249.

[111] Evans, C. C., Reshef, O., Bradley, J., Parsy, F., Choy, J., Deotare, P.,& Mazur, E. (2013). "TiO_2 for Nonlinear Optical Devices". *In Nano-Optics for Enhancing Light-Matter Interactions on a Molecular Scale .. Springer Netherlands*. 405-405.

[112] Sapra, S., & Sarma, D. D. (2004). "Evolution of the electronic structure with size in II-VI semiconductor nanocrystals". *Phys. Rev. B: Condens. Matter*, *69*(12), 125304.

[113] Richard L Sutherland; "Handbook of nonlinear optics",CRC press (2003)

[114] Divya, S., Nampoori, V. P. N., Radhakrishnan, P., & Mujeeb, A. (2014). "Origin of optical non-linear response in TiN owing to excitation dynamics of surface plasmon resonance electronic oscillations". *Laser Phys. Lett.* , *11*(8), 085401.

Chapter 2

Material Preparation Methods and Characterization Techniques

Abstract

This chapter describes the synthesis as well as the main experimental techniques that have been used for the study of TiO_2 based photonic materials.

2.1 Methods of Synthesis

TiO_2 nanoparticles can be synthesized using various methods such as sulfate process, chloride process, impregnation, co-precipitation, hydrothermal method, direct oxidation of $TiCl_4$, metal organic chemical vapour deposition method etc[1]. In the presented work we have mainly utilized sol gel and solvothermal methods.

2.1.1 Sol-Gel

The sol-gel method is a versatile process used for synthesizing various oxide materials due to low cost, ease of fabrication and low processing temperatures[2, 3]. This method generally allows control of the texture, chemical and the morphological properties of the sample. It is extensively used to prepare TiO_2 films, particles etc. In general, the sol gel process involves the transition of a system from a liquid "sol" into a solid "gel" phase. During sol-gel process, a colloidal suspension is formed from the hydrolysis followed by polymerization reactions of the precursors, which are usually inorganic metal salts or metal organic compounds such as metal alkoxides[4,5]. The homogeneity of the resultant material depends on the solubility of reagents in the solvent, the sequence of addition of reactants, the temperature and the pH. The precursors generally used are organic alkoxides. Besides, this method has several other advantages, such as allowing impregnation or co-precipitation, which can be used to introduce dopants.

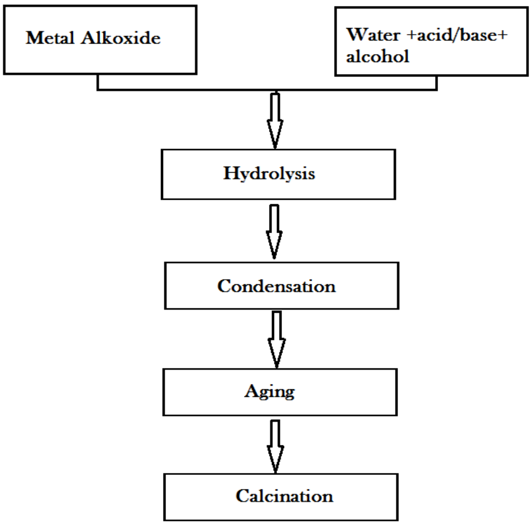

Figure 2.1: *Schematic representation of conventional sol gel route.*

There are several major reactions in the sol-gel process: (i) hydrolysis of the alcohol groups (ii) condensation of the resulting hydroxyl groups leading to the formation of a sol (iii) gelation (iv) ageing and (v) drying which are schematically represented in figure 2.1 and 2.2. Complete polymerization and decrease in the amount of solvent increases the viscosity transforming the liquid sol into a solid gel phase. The wet gel is then converted into a dense ceramic upon further drying and heat treatment. A highly porous and extremely low-density material, known as aerogel, is obtained if the solvent from the wet gel is removed under supercritical conditions.

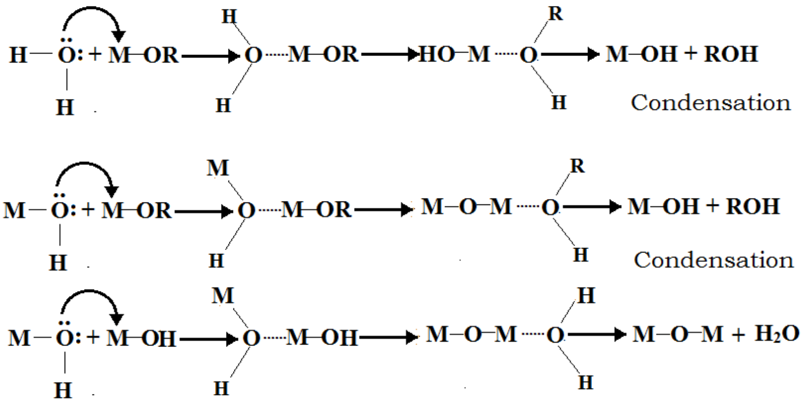

Figure 2.2: *Hydrolysis and condensation steps for sol-gel mechanism.*

Advantages of Sol-Gel Technique

Sol gel technique leads to the synthesis of products with-

- ❑ High degrees of homogeneity, as reagents used are mixed at the molecular level.
- ❑ The prospect to control simultaneously the bulk properties, such as the phase composition, and the surface characteristics, such as the surface area, the total pore volume distribution, etc.
- ❑ Desired level of porosity, by using appropriate heat treatment and firing times.
- ❑ High purity, as organometallic alkoxy precursors can be purified by distillation or recrystallization.
- ❑ Different shape materials into complex geometries in gel state.
- ❑ Simple, economic and effective method to produce high quality coatings.

2.1.2 Hydrothermal Method

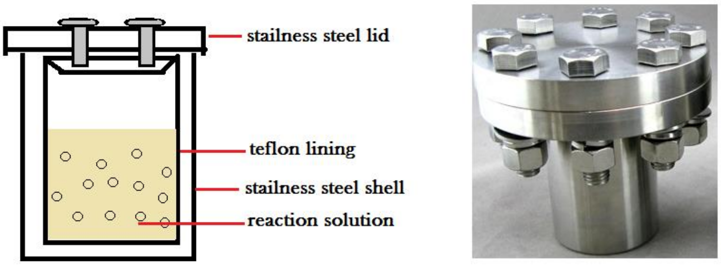

Figure 2.3: *Typical autoclave used in hydrothermal synthesis.*

Usually, this process is carried out in closed steel vessels called autoclaves under controlled temperature and/ pressure with the reactions occurring in aqueous solution as represented in figure 2.3. Here a nutrient is supplied along with water[6]. The temperature can be raised above the boiling point of water, reaching the pressure of vapour saturation. The temperature and the amount of solution taken in the autoclave mostly determine the internal pressure produced. A temperature gradient is maintained between the opposite ends of the growth compartment. At the hotter end, the nutrient solute dissolves, while at the cooler end it is deposited on a seed crystal, growing the desired crystal. The hydrothermal method has been widely acclaimed to prepare TiO_2 nanostructures such as nanotubes, nanospheres, nanoflowers etc. Main advantage of the hydrothermal method over other types of crystal growth is its ability to create crystalline phases which are not stable at the melting point. Shortcomings are the high cost of equipment and the inability to monitor crystals during the process of their growth. TiO_2 nanoparticles are synthesized using this method by adding titanium alkoxide to distilled water and by adjusting the desired pH with HNO_3 or NH_4OH. The mixed solution is then poured into the hydrothermal vessel and treated at 80-100°C for few hours.

2.1.3 Solvothermal Method

The solvothermal method is identical to the hydrothermal method except that a variety of solvents other than water can be used for this process. This method has been found to be a versatile route for the synthesis of a wide variety of nanoparticles with narrow size distributions, particularly when organic solvents with high boiling points are chosen. The solvothermal synthesis allows for the precise control over the size, shape distribution and crystallinity of metal oxide nanoparticles or nanostructures than in the case of the hydrothermal method and has been widely employed to synthesize TiO_2 nanoparticles and nanorods with/without the aid of surfactants[1]. The product characteristics can be varied by changing certain experimental parameters, including reaction temperature, reaction time, solvent type, surfactant type and precursor type.

2.2 Characterization Techniques

No single technique is capable of providing a complete characterization of a sample. There are three different stages of physical investigation techniques that can be used to characterize a material viz. X-ray diffraction, microscopic and spectroscopic techniques. In addition, other techniques such as thermal analysis and physical property measurements can give a complete outlook about the nature of the sample. In the following sections different characterization techniques employed with present studies are described.

2.2.1 X-Ray Diffraction (XRD)

X-ray diffraction method can be used to study single crystals, powders and other forms of solids[7]. It is now a common method to study the crystal structures and atomic spacing. An X-ray powder diffraction pattern is a set of characteristic lines or peaks, each of which is of different intensity and position (d- spacing or Bragg angle, θ) on a strip of photographic film. The interaction of the material produces constructive interference leading to maximum diffracted beam intensity when it satisfies the Braggs Law[8]. The Bragg's law for diffraction is

$$n\lambda = 2dsin\Theta \qquad (2.1)$$

where, n is an integer describing the order of reflection, λ is wavelength of X-ray, d is inter-planar spacing, ϴ is Bragg angle at which diffraction maximum occurs.

Bragg's law relates the wavelength of electromagnetic radiation to the diffraction angle and the d spacing of a crystal. The diffracted X-rays are then detected and processed. Each material gives well-defined peaks characteristic of its crystal structure as each material has a set of unique d spacing. Crystalline material gives sharp peaks whereas an amorphous material gives rise to broad and less intense ones. The intensities may vary from sample to sample depending on the method of sample preparation and the instrumental specifications.

If the line broadening is caused only by small crystallite size, the size can be estimated from the Scherrer's equation 2.2

$$D = \frac{k\lambda}{\beta cos\Theta} \qquad (2.2)$$

where D is mean diameter of the crystallite, β is FWHM on the 2ϴ scale in radian and k is a constant.

XRD studies for the present investigation were performed using an AXS Bruker D% 005 Diffractometer (Germany). X-ray generator was operated at 40 KV and 30mA with Cu as the X-ray source. CuKα with λ = 1.5418 A° radiation was used.

2.2.2 FTIR Spectroscopy

FTIR spectra give information about the bonding between atoms in a sample, and are generally used in the semiconductor industry to determine the presence of dopant or impurity atoms. The results so obtained from this characterization technique gives quantitative data regarding the impurity type whereas qualitative data about the concentration of the impurity.

The studies were done using instrument of Thermo Nicolet, Avatar 370 model with spectral range 4000-400 cm $^{-1}$ and resolution of 4 cm $^{-1}$.

2.2.3 Electron Microscopy

An electron microscope employs a beam of electrons to illuminate a specimen and create an enlarged image, which provides the surface and internal information on a nanometer scale. TEM and SEM have proved to be indispensable tools in nanotechnology for analysing nanostructures.

i. Transmission Electron Microscopy (TEM)

The particle size, shape and detailed morphology of the particle were investigated by TEM (HR-TEM; Philips CM 30) operating at 300 KV[9]. Powder samples were dispersed in distilled water. Here, an electron source generates an electron beam which is accelerated at a high voltage. Electrons are then focused onto the specimen by an electromagnetic condenser lens system. Usually the incident electrons interact with a specimen and X-ray, cathode luminescence and six types of electrons: (1) transmission (2) back-scattered (3) reflected (4) secondary (5) Auger and (6) trapped electrons are generated. The transmission and scattered electrons are collected for TEM imaging. TEM is the only technique allowing a 3D observation and quantitative characterization of most kinds of lattice defects. The diffraction patterns of HRTEM images are also very useful for studying the nanocrystalline phases of materials.

ii. Scanning Electron Microscopy (SEM)

Surface morphological imaging were performed using SEM (JOEL Model JSM-6390LV) equipped with EDS (JOEL Model JED-2300) for qualitative elemental analysis[10]. In SEM, unlike as observed in TEM, it is inelastic scattering which provides information on the specimen to be analysed. When the primary electron beam interacts with the sample, the electrons lose energy by scattering and absorption processes occur within a defined specimen volume. Different types of signal can be collected from inelastic interactions. Most commonly, SEMs are equipped with different detectors for collecting secondary electrons (information on the topography of the surface), backscattered electrons (composition of the surface) and X- rays (elemental analysis of the sample). SEM image relies on surface processes rather than transmission; hence it is able to image bulk samples.

2.2.4 Optical Studies

i. Absorption Spectroscopy

Absorption spectra of the prepared samples were measured using the spectrophotometer JascoV-570(UV/VIS/IR)[11].The spectrometer consists of single monochromatic, UV/VIS region 1200 lines/mm plane grating, NIR region: 300 lines/nm plane grating, Czenry –Turner mount double beam type Resolution : 0.1nm (UV/ VIS region) 0.5nm (NIR region). Light source is a 30 mW deuterium discharge tube in 190 nm to 350 nm region, 20 W tungsten iodide lamp in 330 to 2500 nm region. Wavelength limit ranges from 190 nm to 2500 nm.

ii. Photoluminescence Spectroscopy

Photoluminescence spectra were recorded using Cary Eclipse fluorescence spectrometer of VARIAN[12]. It has appropriate sample holders to perform fluorescence measurements of both liquid and solid samples. The angle of incidence of the excitation i.e. the angle between the exciting light and line perpendicular to the surface of the sample mounting slide in case of solid samples can be varied from 20º-35º. The source of excitation is xenon lamp.

iii. Thermal Lens Experiment for Diffusivity Measurements

Thermal lens (TL) technique aims to optically measure the thermal energy released by the sample on light absorption and consequent non-radiative relaxation of the excited species to lower levels[13]. A typical schematic representation of the technique has been presented in figure 2.4

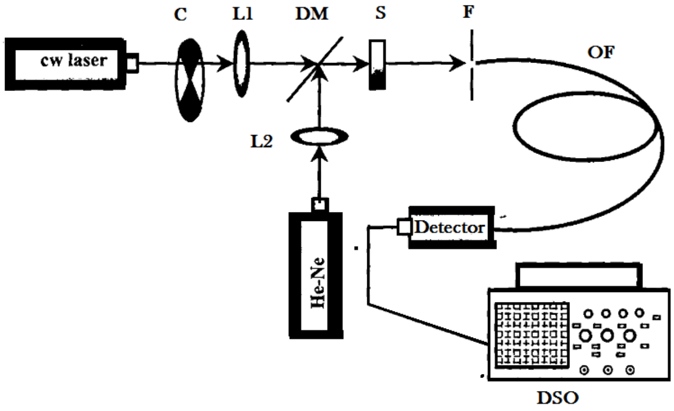

Figure 2.4: *Schematic diagram of the experimental set up: C- Chopper, L1 & L2 –Lenses, DM-Dichroic mirror, S-Sample, F-Filter, OF-Optical Fibre, DSO- Digital Storage Oscilloscope.*

A diode pumped solid state laser (532 nm; 50mW; Micro DPSS laser model BWT-50) with Gaussian beam profile is used as the heating source and an intensity stabilized He–Ne laser (633nm; 4mW; JDS Uniphase) as the probe beam. The pump beam is intensity modulated using a mechanical chopper (HMS /ITHACO model 230). These light beams are made collinear and made to pass through the sample solution with the help of a dichroic mirror and a convex lens. The sample is mounted on a micrometre translation stage. The position of the sample is adjusted so as to obtain maximum intensity change of the probe beam.The thermal lens signal is detected by sampling the intensity at the centre portion of the probe beam by coupling it to a fast photodetector through an optical fibre (OF). Digital storage oscillator (DSO) then processes the signal output from the detector. When chopper allows the irradiation of the pump beam on the sample, it creates a thermal lens in the sample due to local heating of the medium. The temperature distribution in the medium mimics the beam profile of the excitation beam and hence refractive index gradient is created in the medium. This modification in the refractive index causes the medium to acts as a lens, called thermal lens. The thermal lens usually has negative focal length as most of the materials expand upon heating and hence have negative temperature coefficient of refractive index. So, the probe beam which travels collinearly with the pump beam experience a diverging lens and hence beam shape expands due to the formation of the thermal lens. The output TL signal is recorded from which the relative change in intensity and initial slope is measured. Analysis of results leads to the determination of Θ and t_c. From these values, thermal diffusivity of the sample under investigation is evaluated. The thermal lens technique depends on the change in refractive index due to non-radiative de-excitation of sample following the optical excitation which helps in attaining accurate results.

❑ Theory

The magnitude of the effective thermal lens produced by propagation of a continuous Gaussian laser beam of spot size ω is governed by the steady state balance between laser heating and solvent or matrix heat dissipation. If the beam is suddenly turned on at time t=0, the lens approaches to steady state governed by[14]

$$f(t) = f_\infty \left[1 + {}^{t_c}\!/_{2t}\right] \tag{2.3}$$

$$\text{where } f_\infty = {}^{\pi k\omega^2}\!\Big/_{PA\left[\frac{dn}{dT}\right]} \qquad 2.4)$$

where k is the thermal conductivity ($\mathrm{Wcm^{-1}K^{-1}}$) is the laser power (W), A is the sample absorbance, dn/dT is the refractive index change with temperature and t_c is the time response to attain the steady state focal length and is given by

$$t_c = {}^{\omega^2}\!/_{4T_D} \tag{2.5}$$

from which T_D can be calculated. The thermal diffusivity in the sample is detected by its effect on the propagation of the probe laser beam aligned with the centre of the lens. If, after passage through the sample, the laser beam intensity is sampled in a small spot at the centre, the intensity observed is inversely proportional to the beam area. The expression relating the intensity as a function of time is given as[15,16]

$$I_{(t)} = I_{(0)}\left[1 - \frac{\Theta}{1 + {}^{t_c}\!/_{2(t)}} + \frac{\Theta^2}{2\left(1 + {}^{t_c}\!/_{2(t)}\right)^2}\right] \tag{2.6}$$

Modified equation for continuous wave laser source is,

$$I_{(t)} = I_{(0)}\left[1 - \frac{\Theta}{1 + {}^{t_c}\!/_{2(t-t_0)}} + \frac{\Theta^2}{2\left(1 + {}^{t_c}\!/_{2(t-t_0)}\right)^2}\right]^{-1} \tag{2.7}$$

Here t_o is the time at t=0, Θ is directly proportional to P_{th} by the relation

$$\Theta = \frac{P_{th}\left({}^{dn}\!/_{dT}\right)}{\lambda k} \tag{2.8}$$

where P_{th} is the laser power degraded to heat and λ is the laser wavelength. For a given solvent or matrix, Θ is obtained from the initial intensity I_0 and the intensity after the steady state I_t from

$$\Theta = 1 - (1 + 2I)^{1/2} \tag{2.9}$$

$$I = \frac{I_0 - I_\infty}{I_\infty} \tag{2.10}$$

The initial slope m of the decay curve is obtained using the relation,

$$m = {}^{2\Theta}/_{I_0 t_c} \tag{2.11}$$

and hence the value of t_c and hence Θ is calculated.

iv. Z-scan Experiment for the Analysis of Nonlinear Optical Properties

Optical non linearity is very important in the study of semiconductor nanocrystal as it becomes very prominent when the material dimension is reduced to nanoscale regime[17]. Materials with large nonlinear susceptibilities and fast response time are widely used for their potential application in the field of photonic devices. Studies of nonlinear properties of materials are essential for the design and fabrication of devices for various applications like optical limiting and logic gates. For the nonlinear optical measurements, we have employed the open-aperture and closed aperture Z-scan technique developed by Sheik Bahae and his co-workers which is a single beam method used in a wide variety of experiments to determine the nonlinear susceptibilities of solids, ordinary liquids and liquid crystals and has sensitivity comparable to interferometric methods[18]. A Q-switched Nd:YAG laser (Spectra Physics LAB-1760, 532 nm, 7 ns, 10 Hz) is used as the light source and the experimental setup was configured based on Sheikh Bahae et al. The sample to be investigated taken in a 1 mm cuvette were mounted on a translation stage controlled by a computer and was moved along the Z-axis through the focal region of a lens of focal length 20 cm. The radius of the beam waist ω_0 was calculated to be 35.4µm. The Rayleigh length $z_0 = \pi\omega_0^2/\lambda$ was estimated to be 7.4 mm which was higher than the thickness of the sample. This is an essential criterion for Z-scan experiments. The transmitted beam energy, reference beam energy and their ratio were simultaneously measured by an energy ratiometer (Rj7620, Laser Probe Corp) having two identical pyro electric detector heads (Rjp735). The data were analysed using the procedure described by Bahae et.al and the nonlinear coefficients were studied by fitting the experimental Z-scan curve with the theoretical one[19]. The experimental set up for single beam Z-scan set up is presented in figure 2.5.

A single Gaussian laser beam is used in the experiment and the transmittance of the nonlinear medium (or through a finite aperture) in the far field as a function of the sample position z, is measured with respect to the focal plane. This is known as the Z-scan trace. Any deviation from the Gaussian beam profile will lead to inaccurate results. To ensure the beam profile does not undergo considerable changes inside the sample, the sample thickness is always kept less than the Rayleigh range. As the sample is moved along the propagation direction of the beam, the laser beam will experience both amplitude and phase variations. If the transmitted light is measured through an aperture placed in the far field with respect to the focal region, the technique is called **closed aperture Z-scan**[15-16.] Here the transmitted light will be sensitive to both nonlinear absorption and nonlinear refraction. On the other hand when the transmitted light is measured without an aperture, the mode of measurement is known as **open aperture Z-scan**. Here, the output is sensitive only to nonlinear absorption.

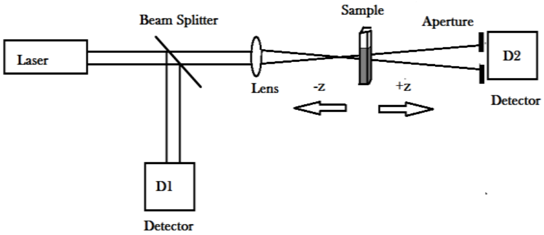

Figure 2.5: *Schematic representation of the experimental set up for Z-Scan technique.*

Closed aperture and open aperture Z-scan method yields the real and imaginary part of nonlinear susceptibility respectively. In order to nullify the effect of nonlinear absorption from the closed aperture Z-scan, generally closed aperture Z-scan data is divided by open aperture data[16]. The resultant Z-scan data contains information only about the nonlinear refraction.

❑ Open Aperture Z-scan Technique

Open aperture Z-scan technique is employed to study the nonlinear absorption in a sample. Nonlinear absorption refers to the variation in the transmittance of a material as a function of intensity or fluence. If nonlinear absorption such as two photon absorption (TPA) is present, it exhibits transmission minimum at the focal point. If the sample is a saturable absorber, transmission increases with increase in incident intensity resulting in transmission maximum at the focus. Typical ideal curves from open aperture Z-scan are shown in figure 2.6.

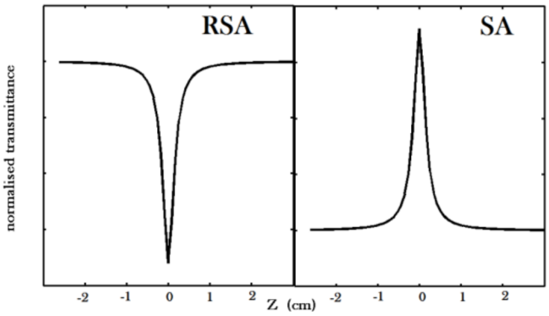

Figure 2.6: *Typical ideal open aperture Z-scan curves: Reverse Saturable Absorption (RSA) and Saturable Absorption (SA).*

Reverse Saturable Absorption (RSA)

When the absorption cross section from excited state is larger than that from the ground state, the transmission of the system will be less under intense laser field. This process is called reverse saturable absorption and the resulting curve is reverse saturable absorption curve.

Saturable Absorption (SA)

When the absorption cross section from excited state is lesser than that from the ground state, the transmission of the system will be more when the system is subjected to intense laser field. This process is called saturable absorption and the resulting curve is saturable absorption curve.

❑ Theory

In the case of open aperture Z-scan, the transmitted light at the output is sensitive only to intensity variations. Hence phase variations are insignificant in this case. The intensity dependent non-linear absorption coefficient α(I) is written in terms of linear absorption coefficient α and Two photon absorption (TPA) coefficient β as

$$\alpha(I) = \alpha + \beta I \tag{2.12}$$

The irradiance distribution at the output surface of the sample can be written as

$$I_r(z,r,t) = \frac{I(z,r,t)e^{-\alpha t}}{1 + q(z,r,t)} \tag{2.13}$$

$$\text{where } q(z,r,t) = \beta I(z,r,t)L_{eff} \tag{2.14}$$

L_{eff} is the effective length in terms of sample length l and α , is given as

$$L_{eff} = \frac{(1 - e^{-\alpha l})}{\alpha} \tag{2.15}$$

The total transmitted power P (z,t) is obtained by integrating equation (2.12) over z and r and is given by

$$P(z,t) = P_I(t)e^{-\alpha l}\frac{\ln[1 + q_0(z,t)]}{q_0(z,t)} \quad (2.16$$

where

$$P_1(t) = \frac{\pi\omega_0^2 I_0(t)}{2} \tag{2.17}$$

$$q_0(z,t) = \frac{\beta I_0(t) L_{eff} z_0^2}{z^2 + z_0^2} \tag{2.18}$$

For a pulse of Gaussian temporal profile, equation (2.16) can be integrated to give the transmission as

$$T(z) = \frac{1}{q_{0\sqrt{\pi}}} \int_{-\infty}^{\infty} \ln\left(1 + q_0 e^{-t^2}\right) dt \tag{2.19}$$

If $|q_0| < 1$ equation (2.18) can be simplified as

$$T(z, S = 1) = \sum_{m=0}^{\infty} \frac{[-q_0(z,0)]^m}{(m+1)^{3/2}} \tag{2.20}$$

where m is an integer. The parameter q_0 can be obtained by fitting the experimental results to equation (2.18). Then nonlinear absorption coefficient β can be obtained from equation (2.19).The strength of nonlinear absorption is determined from the imaginary part of third order susceptibility $\chi^{(3)}$ by the relation[20]

$$Im\,\chi^3 = \frac{\varepsilon_0 n_0^2 c^2 \beta}{\omega}(m^2V^{-2}) = \frac{n_0^2 c^2 \beta}{240\pi^2\omega}\ (esu) \tag{2.21}$$

where λ is the excitation wavelength, n_0 is the linear refractive index, ε_0 is permittivity of free space and c the velocity of light in vacuum.

❑ Closed Aperture Z-scan Technique

The closed aperture Z-scan data contains the information about self-refraction and self-phase modulation. When the sample is moved along various positions along the z–axis, it starts acting as a thin lens of variable focal length due to change in refractive index at each position

$$n(I) = n_{0+}n_2 I \tag{2.24}$$

where, n_o is the linear refractive index of the sample and n_2 is the nonlinear refraction. At the beginning, when the sample is far away from the focus (-z) the beam irradiance is low and negligible nonlinear refraction occurs, hence the transmittance remains almost constant. As the sample is moved towards the focus, beam irradiance increases leading self-lensing in the sample. A negative self-lensing prior to the focus will collimate the beam, causing beam narrowing at the aperture resulting in an increased transmittance. As the sample moves, away from the focus (+z), self-defocussing occurs which increases the beam divergence, leading to beam broadening at the aperture, thereby decreasing the transmittance. So the Z-scan trace will cross the zero during this process. Therefore, a negative nonlinear refraction will result in peak-valley structure whereas positive nonlinear refraction follows valley-peak structure. Hence it can be concluded that besides the ease of measurement of the magnitude of nonlinear refraction (n_2), deduction of its sign are the major advantage of the Z-scan experiment. Typical ideal curves from closed aperture Z-scan are as shown in figure 2.7

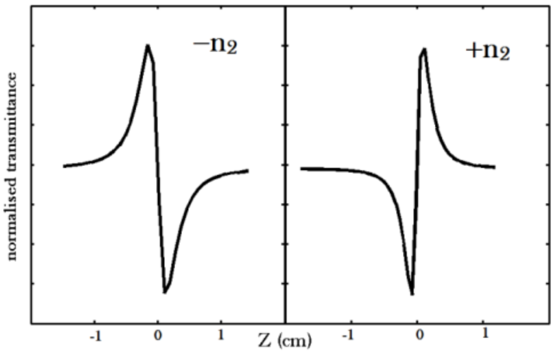

Figure 2.7: *Typical ideal closed aperture Z-scan curves: negative non-linear refractive index (-n_2) and positive non-linear refractive index (+n_2).*

❑ Theory

In a cubic nonlinear medium the index of refraction (n) is expressed in terms of nonlinear index (n_2) as

$$n = n_0 + n_2|E|^2 = n_0 + n_2 I \tag{2.25}$$

where no is the linear index of refraction ,E is the peak electric field ,n_2 is the intensity dependent refractive index and I denotes the irradiance of the laser beam within the sample. Assume a TEM_{00} beam of waist radius w_0 travelling in the +z direction then

$$E(z,r,t) = E_0(t)\frac{\omega_0}{\omega(z)} exp\left[-\frac{r^2}{\omega^2(z)} - \frac{ikr^2}{2R(z)} e^{i\Phi(z,t)}\right] \tag{2.26}$$

where beam radius is

$$w^2(z) = \omega_0^2\left(1 + {z^2}/{z_0^2}\right) \tag{2.27}$$

Radius of curvature of the wave front at z :

$$R(z) = z\left(1 + {z^2}/{z_0^2}\right) \tag{2.28}$$

Beam diffraction length $z_0 = {k\omega_0^2}/{2}$ (2.29)

and wave vector $k = {2\pi}/{\lambda}$ (2.30)

$E_0(t)$ is the radiation electric field at the focus and contains the temporal envelope of the laser pulse. The term $e^{i\Phi(z,t)}$ contains all the radially uniform phase variations. As the beam reaches the exit surface of the sample, it suffers radial variations in its phase given by ΔΦ(r). For a thin sample, the amplitude and phase of the electric field varies as a function of position inside the sample z' and is given by

$$\frac{d\Delta\Phi}{dz'} = \Delta(I)k \tag{2.31}$$

$$\frac{dI}{dz'} = -\alpha(I)I \tag{2.32}$$

Where $\alpha(I)$ in general includes linear and nonlinear absorption terms. For cubic non linearity and negligible nonlinear absorption equation (2.31) and (2.32) can be solved to obtain the phase shift ΔΦ at the sample exit surface and is given as,

$$\Delta\Phi(z,r,t) = \Delta\Phi\ (z,t)exp\left[-\frac{2r^2}{\omega^2(z)}\right] \tag{2.33}$$

with

$$\Delta\Phi(z,t) = \frac{\Delta\Phi_0\ (t)}{(1+{z^2}/{z_0^2})} \tag{2.34}$$

$\Delta\Phi_0\ (t)$ is the on axis phase shift at the focus defined as

$$\Delta\Phi_0\ (t) = k\Delta n_0(t)L_{eff} = \frac{2\pi}{\lambda}n_2I_0(t)L_{eff} \tag{2.35}$$

where $I_0(t)$ is the on axis irradiance at the focus. The complex electric field exiting the sample E_e now contains the non-linear phase distribution

$$E_e(z,r,t) = E(z,r,t)e^{-\alpha l/2}e^{i\Delta\Phi[z,r,t]} \tag{2.36}$$

By virtue of Huygen's principle and guassian decomposition method;

$$e^{i\Delta\Phi\ (z,r,t)} = \sum_{m=0}^{\infty}\frac{[i\Delta\Phi_0(z,r,t)]^m}{m!}e^{-2mr^2/\omega^2(z)} \tag{2.37}$$

After including the initial beam curvature for the focussed beam, resultant electric field pattern at the aperture is given by

$$E_a(r,t) = E(z,r=0,t)e^{-\alpha l/2} \times \sum_{m=0}^{\infty}\frac{[i\Delta\Phi_0(z,t)]^m}{m!}\frac{\omega_{mo}}{\omega_m}\exp\left[-\frac{r^2}{\omega_m^2}-\frac{ikr^2}{2R_m}+i\Theta_m\right] \tag{2.38}$$

If, d is the propagation distance in free space from sample to the aperture plane and

$$g = 1 + \frac{d}{R(z)} \tag{2.39}$$

The remaining parameters in the above equation can be expressed as

$$\omega_{mo}{}^{2} = \frac{\omega^{2}(z)}{(2m+1)}\ ;\ d_m = \frac{k\omega_{mo}{}^{2}}{2};\ \Theta_m = \tan^{-1}\left[\frac{{}^{d}\!/_{d_m}}{g}\right] \tag{2.40}$$

$$\omega_m^2 = \omega_{mo}{}^{2}\left[g^2 + \frac{d^2}{d_{mo}^2}\right] \text{ and } R_m = d\left[1 - {}^{g}\!\Big/_{g^2 + \frac{d^2}{d_m^2}}\right]^{-1} \tag{2.41}$$

The on axis electric field at the aperture plane is obtained by putting r=0 in equation (2.38). In case of small nonlinear phase change [$\Delta\Phi_0 \ll 1$] and small aperture normalised transmittance can be written as

$$T(z,\Delta\Phi_0) = \frac{|E_a(z,r=0,\Delta\Phi_0|^2}{|E_a(z,r=0,\Delta\Phi_0=0|^2}$$

$$= \frac{\left|(g + {}^{id}\!/_{d_0})^{-1} + i\Delta\Phi_0(g + {}^{id}\!/_{d_1})^{-1}\right|^2}{\left|(g + {}^{id}\!/_{d_0})^{-1}\right|^2} \tag{2.42}$$

The far field condition d$\gg z_0$ gives geometry independent normalised transmittance as

$$\mathrm{T}(\mathrm{z},\Delta\varphi_0) = 1 + \frac{4\Delta\varphi_0\mathrm{x}}{(\mathrm{x}^2+9)(\mathrm{x}^2+1)} \tag{2.43}$$

Here x=z/z$_0$ &; $\Delta\varphi_0 = {}^{2\pi\, n_2\, I_0 L_{eff}}\!/_{\lambda}$ (2.44)

For cubic non linearity, the peak and valley of the Z-Scan transmittance can be calculated by solving the equation

$$\frac{dT(z,\Delta\varphi_0)}{dz} = 0 \tag{2.45}$$

Solution to this yields the peak valley separation as

$$\Delta Z_{p-v} = 1.7z_0 \tag{2.46}$$

Peak valley transmittance change is given as

$$\Delta T_{p-v} = 0.406\Delta\Phi_0 \tag{2.47}$$

Studies have proved that this relation is accurate to 0.5% for $|\Delta\Phi_0| \leq \pi$. For large aperture, this equation is modified within 2% accuracy and is given as

$$\Delta T_{p-v} = 0.406(1-S)^{0.25}|\Delta\Phi_0|;\ for\ |\Delta\Phi_0| \leq \pi \tag{2.48}$$

where S is the linear transmittance of the far field aperture. From the closed aperture Z-Scan fit, $|\Delta\Phi_0|$ can be obtained. Then the nonlinear refractive index n_2 can be determined using equation (2.35) and is given as

$$n_2 = \frac{\lambda}{2\pi\, n_2\, I_0 L_{eff}} \Delta\Phi_0 \left({}^{m^2}\!/_{W}\right) = \frac{c n_0 \lambda}{80\pi^2\, n_2\, I_0 L_{eff}} \Delta\Phi_0\ (esu) \qquad (2.49)$$

The n_2 is related to Re $\chi^{(3)}$ as

$$Re\chi^{(3)} = 2n_2\, \varepsilon_0 n_0^2 c\, (m^2V^{-2}) = {}^{n_0 n_2}\!/_{3\pi}\ (esu) \qquad (2.50)$$

Thus from the real and imaginary part of $\chi^{(3)}$, the modulus of third order nonlinear susceptibility can be found out as

$$|\chi^{(3)}| = \sqrt{[Re\chi^{(3)}]^2 + [Im\chi^{(3)}]^2} \qquad (2.51)$$

The magnitude of $\chi^{(3)}$ determines the strength of non-linearity of the material.

2.3 Dye Sensitised Solar Cell (DSSC) Characterization

2.3.1 Assembling of DSSCs

The ITO coated counter electrode was placed on the top so that the conductive side of the counter electrode faced the dye adsorbed TiO_2 film. Electrolyte placed at the edges was drawn into the space between the electrodes by capillary action. Binder clips were used to hold the electrodes together. Figure 2.8 shows the picture of a typical experimental laboratory level DSSC cell.

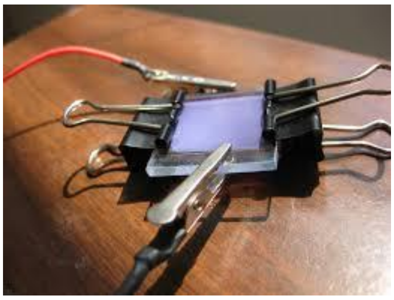

Figure 2.8: *Picture of a typical experimental laboratory level DSSC.*

2.3.2 Characterization

The standard characterization techniques of solar cells include the determination of the dc current–voltage characteristic under white light illumination of different intensities and the determination of the photocurrent under low intensity monochromatic light. Figure 2.9 shows typical I-V characteristics of a solar cell. Analysis of the photocurrent– voltage curves includes the determination of the following parameters:

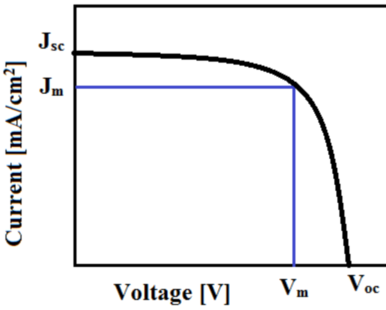

Figure 2.9: *Typical I-V Characteristics of a solar cell.*

- ☐ The **Fill Factor (FF)** is the ratio of the maximum power to the external short- and open-circuit values, and is calculated as

  $$FF = \frac{J_m \times V_m}{J_{sc} \times V_{oc}} \tag{2.52}$$

  Where J_{SC} (short-circuit current density) is measured under the condition where the applied potential, V, equals zero volt. V_{OC} (open-circuit potential) is the cell potential measured when the current in the cell is zero, corresponding to almost flat valence and conduction bands. J_m and V_m are the maximum current density and voltage, respectively

- ☐ The **Efficiency (η)** measures the performance of a solar cell and is defined as the ratio of the maximum electrical power extracted to the radiation power incident on the solar cell surface[21].

  $$\eta = \frac{P_{max}}{P_{in}} = \frac{J_{sc} \times V_{oc} \times FF}{P_{in}} \tag{2.53}$$

- ☐ The **Incident Photon to Charge Carrier Efficiency (IPCE)**, mentioned as the ‘external quantum efficiency’ (EQE), is a vital characteristic of a device. Precisely, with devices using same architecture, it is possible to compare the light-harvesting performance of sensitizers. This performance parameter is defined as the number of electrons generated by light in the external circuit divided by the number of incident photons as a function of excitation wavelength, as in the following equation[22]

  $$\mathrm{IPCE}(\lambda) = \frac{\text{photocurrent density}}{\text{wavelength } \times \text{photonflux}} = \mathrm{LHE}\ (\lambda) \times \Phi_{inj} \times \eta_c \tag{2.54}$$

where LHE(λ) is the light-harvesting efficiency at wavelength λ, Φ_{inj} is the quantum yield for electron injection from the excited sensitizer in the conduction band of TiO_2 and η_c is the efficiency for the collection of electrons. IPCE(λ) is determined experimentally from the measurement of the short-circuit photocurrent density J_{SC} under illumination at wavelength λ with incident power density P_{in} using the formula[23],

$$\mathrm{IPCE}(\lambda) = \frac{1240 \times J_{sc}}{P_{in} \times \lambda} \qquad (2.55)$$

2.4 Conclusions

The preparation methods used in the research work have been discussed in the chapter. The characterization techniques along with theory, used to analyse the samples in different aspects viz., morphology, chemical structure, optical properties have been presented in detail. A brief outline on DSSCs is also presented in this chapter.

2.5 References

---

[1] Chen, X., & Mao, S. S. (2007). “Titanium dioxide nanomaterials: synthesis, properties, modifications, and applications”. *Chem. Rev., 107*(7), 2891-2959.

[2] Najafi, S. I., Touam, T., Sara, R., Andrews, M. P., & Fardad, M. A. (1998). “Sol-gel glass waveguide and grating on silicon”. *J. Lightw. Tech., 16*(9), 1640.

[3] Jiang, H., Yuan, X. C., Lam, Y. L., Chan, Y. C., & Ng, G. I. (2001). “Single-step fabrication of surface relief diffractive optical elements on hybrid sol-gel glass”. *Opt. Eng.* , *40*(9), 2017-2021.

[4] Zhang,G.,& Hua,I. (2000). “Cavitation chemistry of polychlorinated biphenyls: decomposition mechanisms and rates”. *Environ. Sci. Technol., 34*(8), 1529-1534.

[5] Wu, L., Yu, J. C., Zhang, L., Wang, X., & Ho, W. (2004). “Preparation of a highly active nanocrystalline TiO_2 photocatalyst from titanium oxo cluster precursor”. *J. Solid State Chem., 177*(7), 2584-2590.

[6] Abbasi, A. Z. (2010). Synthesis and applications of nanoparticles in polymer matrix (Doctoral dissertation, Philipps-Universität Marburg).

[7] J.Tanaka, and S.L. Suib, (1999). “Experimental Methods in Inorganic Chemistry”, *PracticeHall,*NewJersey,

---

[8] Patterson, A. L. (1939). “The Scherrer formula for X-ray particle size determination”. *Phys. Rev.*, *56*(10), 978.

[9] Transmission electron microscope , HR-TEM;*Philips CM 30*,manual

[10] Scanning electron microscope ((*JOEL Model JSM-6390LV*) equipped with EDS (*JOEL Model JED-2300*),Japan. Manual.

[11] Model V-550/560/570 Spectrophotometer Hardware /Function manual (data station type). *JASCO Corporation* ,Tokyo, Japan

[12] Cary Eclipse Hardware operation manual, *VARIAN* Australia (2000).

[13] Santhi, A., Umadevi, M., Ramakrishnan, V., Radhakrishnan, P., & Nampoori, V. P. N. (2004). “Effect of silver nano particles on the fluorescence quantum yield of Rhodamine 6G determined using dual beam thermal lens method”. *Spectrochim. Acta, Part A*, 60(5), 1077-1083.

[14] Whinnery, J. R. (1974). “Laser measurement of optical absorption in liquids”. *Acc. Chem. Res.*, *7*(7), 225-231.

[15] Brannon, J. H., & Magde, D. (1978). “Absolute quantum yield determination by thermal blooming. Fluorescein”. *J. Phys. Chem.*, *82*(6), 705-709.

[16] Kurian, A. (2002). “Characterization of photonic materials using thermal lens technique” (*Doctoral dissertation*, Cochin University of Science and Technology).

[17] Nalwa, H. S., & Miyata, S. (1996). “Nonlinear optics of organic molecules and polymers”. *CRC press*.

[18] M.S. Bahae, A.A. Said, E.W. Van Stryland. (1989) “High-sensitivity, single-beam n 2 measurements”. *Opt. Lett.*, 14,955

[19] Sheik-Bahae, M., Said, A. A., Wei, T. H., Hagan, D. J., & Van Stryland, E. W. (1990). “Sensitive measurement of optical nonlinearities using a single beam”. *IEEE J. Quant. Electron.*, 26(4), 760-769.

[20] Divya, S., Nampoori, V. P. N., Radhakrishnan, P., & Mujeeb, A. (2014). “Intermediate Ce^{3+} defect level induced photoluminescence and third-order nonlinear optical effects in TiO_2–CeO_2 nanocomposites”. *Appl. Phys. A*, 114(2), 315-321.

[21] Divya, S., Thankappan, A., Vallabhan, C. P. G., Nampoori, V. P. N., Radhakrishnan, P., & Mujeeb, A. (2014). “Electrolyte/photoanode engineered performance of TiO_2 based dye sensitised solar cells”. *J. Appl. Phys.*, *115*(6), 064501.

[22] Nazeeruddin, M. K., Baranoff, E., & Grätzel, M. (2011). “Dye-sensitized solar cells: a brief overview”. *Sol. Energy* , *85*(6), 1172-1178.

[23] Sandquist, C., & McHale, J. L. (2011). “Improved efficiency of betanin-based dye-sensitized solar cells”. *J. Photochem. Photobiol., A, 221*(1), 90-97.

Chapter 3

Fluorescence and Third Order Nonlinear Studies on TiO_2: From Amorphous to Rutile Phase

Abstract

The present chapter deals with the synthesis and characterization of TiO_2 and its polymorphs. Optical band gap is found to vary with annealing temperature. The fluorescence emission spectra confirmed the presence of more imperfections and disorders in anatase than in rutile phase. The third-order nonlinear susceptibilities of TiO_2 and its polymorphs; anatase and rutile, prepared by sol-gel technique followed by heat treatment were investigated using the Z-scan technique at wavelength of 532 nm with laser pulses of 7ns duration. It was found that the values of optical constants of amorphous TiO_2 after subjecting it to heat treatment varied considerably. It is assumed that this can be due to variation in the electronic structure of TiO_2 synchronous with the formation of its polymorphs, anatase and rutile. Amorphous TiO_2 is marked by the localization of the tail states near the band gap, whereas its crystalline counterparts are characterised by complete delocalised tail states.

Results of this chapter are published in :

i. S. Divya et.al. *Opt. Laser Technol.* (2014), 56, 207-210.
ii. S. Divya et.al. *Chin. Phys. B.* (2014), 23(3), 034210.

3.1 Introduction

Materials with large third-order optical nonlinearity have drawn significant scientific attention due to their high prospective applications in optical communication devices, such as all-optical switches, optical correlators etc.[1,2]. During the past years, the metal/dielectric composite films were considered to have the most prevalent third-order nonlinear susceptibilities due to the pronounced enhancement of local field[3]. However, a drawback of this kind of films is the thermal damage and light loss induced by the large resonance absorption[4]. Interestingly, as an alternate candidate for nonlinear optical materials, metal oxide thin films have shown growing interest due to the high optical nonlinearity, fast response time, and low absorption index[5,6]. TiO_2 is one such material which has been in the scientific limelight because of their irreplaceable role in applications related to environmental cleaning and protection, photocatalysis, gas sensing, fabrication of solar cells and batteries[7,8,9]. In addition to being frequently used in technological applications it also proves its suitable candidature in areas such as production of paints, paper, plastics, cosmetics, etc.[10,11,12]. TiO_2 is a high band gap semiconductor transparent to visible light and has exceptional optical transmittance. It possesses high refractive index and good insulating properties. Besides its various applications, due to its low cost and safety towards humans and our environment, it can be considered beneficial to humankind in all respects. TiO_2 exists in three polymorphic phases: rutile (tetragonal density = 4.25 g/cm^3), anatase (tetragonal, 3.894 g/cm^3) and brookite (orthorhombic, 4.12 g/cm^3)[13]. Both anatase and rutile have tetragonal crystal structures but belong to different space groups. The brookite phase has an orthorhombic crystalline structure and is having an unstable phase and hence, is of very little scientific interest. Among these three, rutile is the most thermodynamically stable phase; anatase and brookite are metastable phase and are transformed to rutile on heat treatment. In general, the rutile phase is formed at high temperatures, while the anatase phase is formed at low temperatures. However, rutile phase possesses higher values of refractive index, dielectric constant, electric resistance and stability[14]. Usually brookite exists as an impurity in anatase and rutile phases and hence these two remain the most investigated forms. It has been noted that the physical properties and the nonlinear optical response of TiO_2 films are strongly dependent on the processing route[15]. In general, anatase is characterised by the presence of self-trapped excitons, whereas the rutile has free excitons[16]. This opposite nature of excitonic states in anatase and rutile is related to their structural differences. The non-linearity of nanoparticles in such cases is due to excitonic absorption caused by photo excited generation of excitons. Studies related to their electronic and optical properties using orthogonalised linear-combination-of-atomic-orbitals method have already been reported[17]. In the present chapter, investigation on physics of bound excitons and giant nonlinearities associated with them have been conducted and explained. The short radiative lifetime associated with this large oscillator strength allows fast switching in a nonlinear-optical device operated at near-resonant wavelengths. Here, the electronic and optical properties of amorphous, anatase and rutile phases have been mainly focussed. However, here we have expounded the variation in the properties of these two forms by considering the role played by excitons by analysing their nonlinear phenomenon studied using Z-scan technique. Here, we have tried to explain the physics of bound excitons and giant nonlinearities associated with them.

3.2 Experimental

The TiO_2 sol was prepared via sol-gel method and is synthesized as follows. Titanium tetrabutoxide (TTBO) was used as the precursor to prepare TiO_2 sol. A mixture of HCl and isopropyl alcohol was added to TTBO under continuous magnetic agitation at room temperature. The TiO_2 sol composition was of molar ratio TTBO /isopropanol/water =1:26.5:1.5. The [H+]/ [TTBO] molar ratio ranged from 0.02 to 1.1. The resultant TiO_2 sol was clear and stable. The obtained nanoparticles were thermal treated at 100ºC to remove the excess moisture content. Thus amorphous TiO_2 nanoparticles were obtained. Further, these amorphous nanoparticles in powder form were subjected to 500ºC and 900ºC to obtain the anatase and rutile TiO_2 respectively.

The prepared TiO_2 samples were characterised by optical absorption measurements using a UV/VIS/IR spectrophotometer. Optical nonlinear absorption coefficient (ß) and nonlinear refractive index (n_2) of the samples were calculated by both open and closed aperture Z-scan technique using a Nd:YAG laser[18]. Z-scan technique developed by Bahae.et. al., is a single beam method for measuring the sign and magnitude of nonlinear refractive index n_2 and has sensitivity comparable to interferometric methods. The sample is moved in the direction of light incidence near the focal spot of the lens with a focal length of 200 mm. The Rayleigh length z_0 is estimated to be 7.4 mm, much greater than the thickness of the sample cuvette (1mm), which is an essential prerequisite for Z-scan experiments. The data were analysed using the procedure described by Bahae et.al. and the non-linear coefficients were obtained by fitting the experimental Z-scan plot with the theoretical plots[19].

3.3 Results and Discussions

i. Absorption Spectroscopy

The absorption spectra of the samples dispersed in deionized water are as shown in figure 3.1. From the figure it is evident that with the formation of anatase and rutile TiO_2, there occurs relative red shift in the absorbance spectra. The graph shows that annealing induces the growth of TiO_2 nanoparticles.

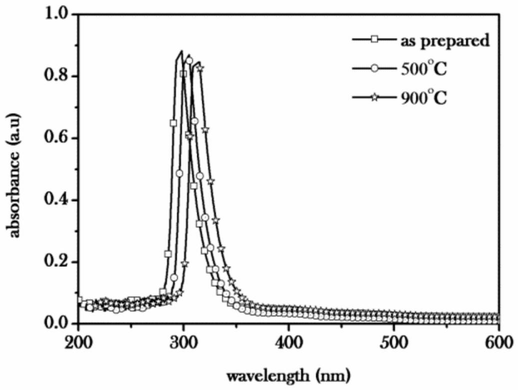

Figure 3.1: *Absorption spectra of the TiO_2 nanoparticles.*

The optical band gap can be estimated by plotting $(\alpha h\upsilon)^2$ versus photon energy ($h\upsilon$) based on the relation[20]

$$\alpha h\upsilon = A(h\upsilon - Eg)^{½} \qquad (3.1)$$

where α is the absorption coefficient, A is a constant, Eg is the band gap. According to the above relation, the intercept of the tangent on the photon energy axis corresponds to optical band gap.

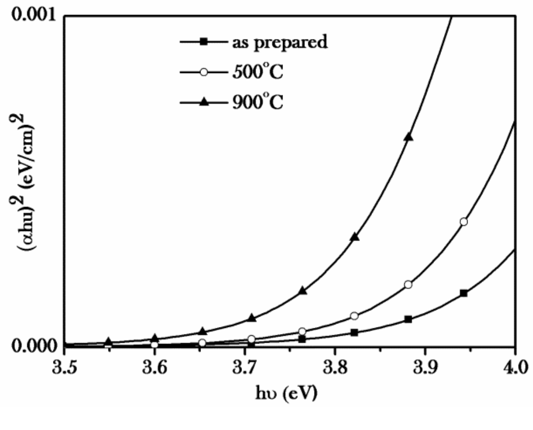

Figure 3.2: *$(\alpha h\upsilon)^2$ v/s hυ plot for determining the band gap of the TiO_2 nanoparticles.*

Figure 3.2 represents the band gap calculation of the samples. A decrease in the band gap of the semiconductor is observed with increasing annealing temperature. This could be due to the fact that when the samples are subjected to higher temperature the crystallites begin to move and start agglomerating thereby decreasing the band gap.

ii. Photoluminescence Studies

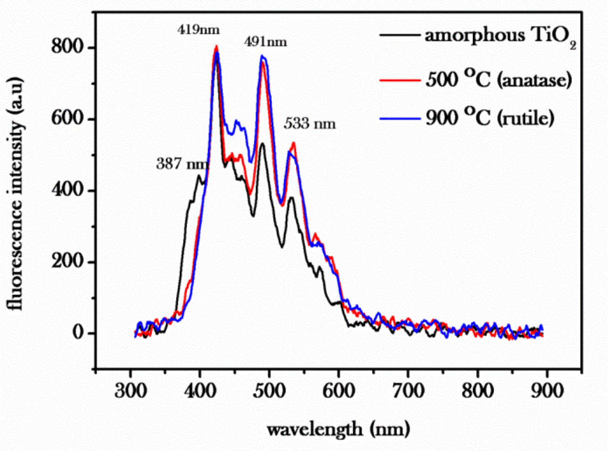

Figure 3.3: *Fluorescence spectrum of the nanoparticles at an excitation wavelength of 255nm.*

Figure 3.3 represents the fluorescence spectra of the samples at an excitation wavelength of 255nm. Figure shows multiple emission peaks at 387 nm, 419 nm, 491 nm and 533 nm. Emission at 387 nm is due to annihilation of excitons while remaining three peaks could be arising from surface states[21]. The surface state is generally localized within the band gap of the semiconductor and they can trap the excited state electrons and can lead to higher wavelength emissions. The oxygen vacancies and surface hydroxyl groups are the dominant sites for trapped electrons and holes. These trapped carriers which are captured by oxygen vacancies and surface hydroxyl groups, contribute to the visible luminescence in these nanoparticles. Emissions at 419 nm, 491 nm, and 533 nm are assigned to the surface state emissions and are due to the recombination of trapped electron–hole arising from dangling bonds in the TiO_2 nanoparticles. As the sample is annealed, the emission at 387 nm subsides and this could be related to the fact that nanoparticle having more surface states dominate the excitonic emission. The emission at 533 nm is found to be due to O^{2-} vacancies. Therefore, it is concluded that the visible luminescence band originates from the oxygen vacancies associated with Ti^{3+}. Here it is observed that as the annealing temperature increases, emission peaks undergo slight red shift as observed in absorption spectra due to the increase in particle size. Further it is noted that the intensity of green luminescence increases with annealing temperature and is maximum for anatase followed by rutile. These emissions are again due to oxygen vacancies and hence it can be confirmed that anatase consists of more imperfections and disorder. This result is in agreement with the conclusion drawn by H.Tang[16]. This may be due to the fact that anatase crystallizes in a less dense structure than rutile[22]. This favours impurity diffusion and disorder creation in anatase crystals.

It is observed that the surface state emission generally consists of two categories of emission. One set occurs as series giving emissions at 421 nm, 491 nm and 573 nm with almost a difference of nearly 80 nm. This occurs from the de-excitation from lower vibronic levels in Ti^{3+} 3d states of TiO_2 to the deep trap levels (acceptor) created by OH^-. Another set is having emission wavelengths 533 nm and 612 nm, which are also separated by nearly 80 nm. These emissions are due to de-excitation from lower vibronic levels in the oxygen vacancies of TiO_2 lattice to the ground state. The whole emission mechanism is depicted in the figure.3.4.

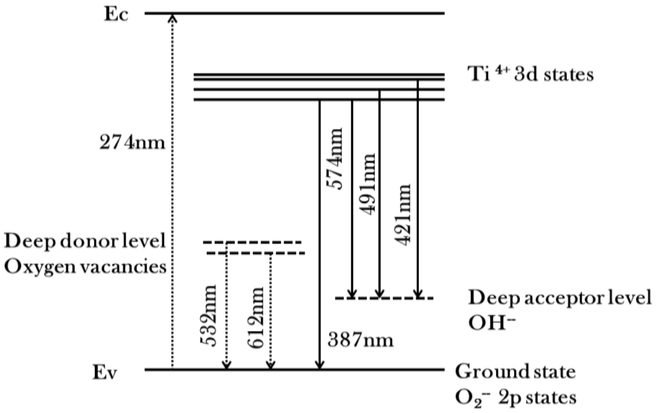

Figure 3.4: *Emission mechanism in* TiO_2 *nanoparticles.*

iii. XRD Studies

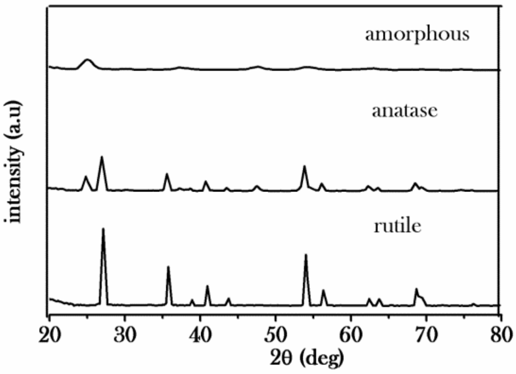

Figure 3.5: *XRD pattern of amorphous, anatase and rutile* TiO_2 *nanoparticles.*

Figure 3.5 represents the XRD pattern of amorphous, anatase and rutile TiO_2. Amorphous TiO_2 does not have any characteristic crystalline peaks. The experimental spacing were compared with those reported for rutile (110) (2θ of 27.45◦) and anatase (101) (25.24◦) to identify the particle structure[23].

iv. Nonlinear Optical Studies

The third order nonlinear optical properties of nano TiO_2 samples were investigated using Z-scan technique and are represented in figure 3.6 and 3.7 at a laser power of $196 MW/cm^2$. In order to ensure that no permanent photo induced change has occurred to the sample during laser irradiation, the experiments were repeated by illuminating the sample at the same position.

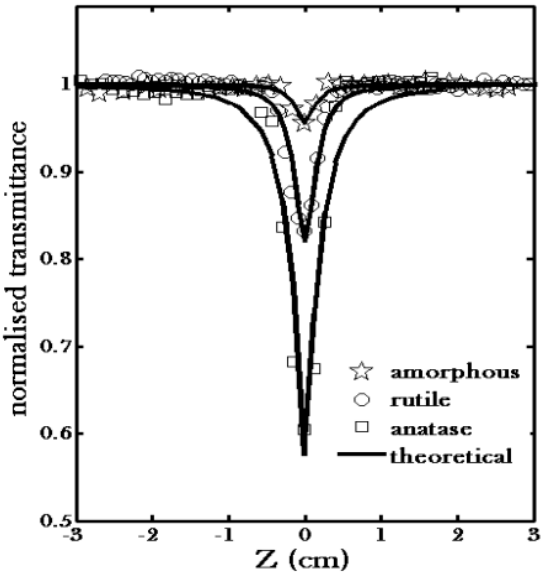

Figure 3.6: *Normalized transmittance as a function of the position in the open aperture scheme at 532 nm with a laser power of 196 MW/cm^2.*

Linear absorption coefficients of the samples were: 0.0238, 0.0113 and 0.0252 for amorphous, anatase and rutile respectively. The obtained curves follow reverse saturable absorption (RSA) nature.Under the experimental conditions, laser beam illumination at 532 nm usually corresponds to the two-photon absorption (TPA) process because the photon energy of the 532 nm laser is within the range $Eg < 2h\nu < 2Eg$, where $h\nu=2.33$ eV. The Z-scan traces were made for all the different phases of TiO_2 by varying input power densities. The open aperture Z-scan traces are shown in figure 3.6, the fits to the experimental data are depicted in the figure by the solid curve.The induced absorption in the samples are indicated by the transmittance valley.

Figure 3.7 represents the closed aperture Z-scan traces of the samples.The closed aperture curve exhibited a peak to valley shape, indicating a negative value for the non linear refractive index n_2. It is observed that the peak –valley of the closed aperture Z-scan satisfies $\Delta z \sim 1.7 z_0$, thus confirming the presence of cubic non linearity.

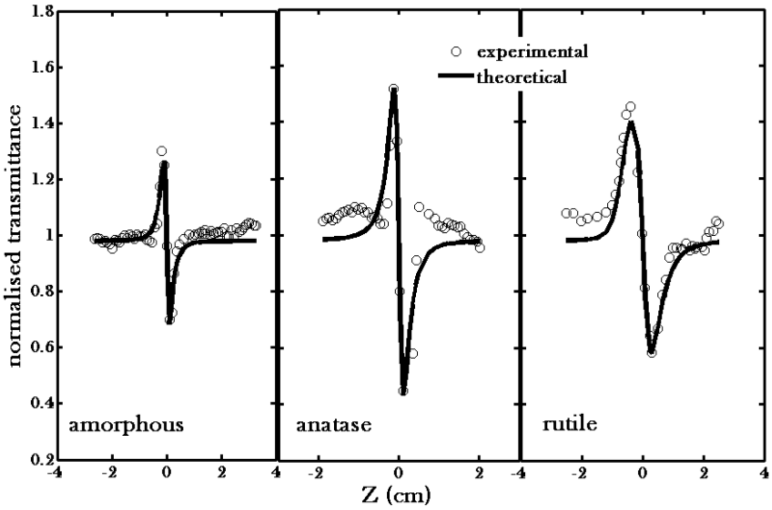

Figure 3.7: *Normalized transmittance as a function of the position in the closed aperture scheme at 532 nm at a laser power of 196 MW/cm* ^{2}.

From the figures 3.6 and 3.7 it is clearly evident that as the annealing temperature increases the non-linearity increases .This can be attributed to the fact that with increase in the annealing temperature, size of TiO_2 increases. This enhancement of nonlinear optical properties with increasing dimension in the weak confinement regime originates from the size dependent enhancement of oscillator strength of coherently generated excitons[24] .

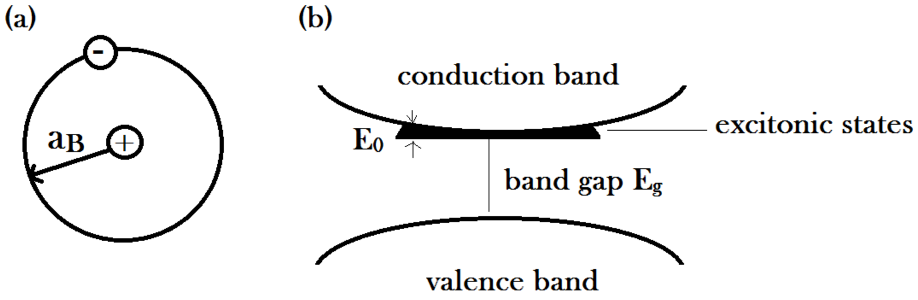

Figure 3.8: *(a) Model for the electron–hole pair for exciton states.(b) Location of the exciton states relative to the conduction and valence bands.*

Excitons are electronic excitations of semiconductors and insulators comprising of electron-hole pairs linked through Coulomb correlated force as represented in figure 3.8. Exciton polaritons are composite quasi-particles formed by the coupling of light and dipole-active excitons[25].

(a) Bound exciton (b) Free exciton

Figure 3.9: *(a) Bound excitons: electron is strongly bounded and confined to within a single lattice constant. (b) Free excitons: electron is weakly bounded with an average radius larger than the lattice constant.*

Sometimes the generation of excitons leads to ionic relaxation which eventually traps the excitons within a single lattice constant thus localising it and hence they are known as bound excitons. Bound and free excitons are pictorially represented in figure 3.9. The confinement of excitonic wave function is expected to give rise to enhancement of the oscillator strength by a factor of R^3/a_B^3, where R is the particle size and a_B is exciton effective Bohr radius. But as expected rutile phase does not have larger non linearity than the anatase phase. This may be due to the fact that anatase has bound excitons and hence larger excitonic binding energy whereas the rutile phase is characterised by free excitons with negligible binding energy. In both polymorphs, the excitonic wave functions are two dimensional and this planar distribution is localized in just one atomic layer in the anatase case. This stronger localization probably supports the possibility of experimentally reported self-trapping[26]. Usually nonlinear optical effects are enhanced when the associated optical transition has large optical oscillator strength. As reported by Rashba and Gurgenishivili, excitons weakly bounded to impurities, have giant oscillator strengths that are many orders of magnitude larger when compared to the oscillator strength per molecule of the free excitons [27]. A free exciton, can be considered as a quasi-particle moving in the field of the centre as a single entity. The radius of this state exceeds that of the internal motion in the excitons and hence it possesses weaker oscillator strength and consequently lower magnitude of nonlinearity. Also, from the fluorescence spectra, it has been observed that anatase has more imperfections and disorder which also contribute to the nonlinear effects to a major extent.

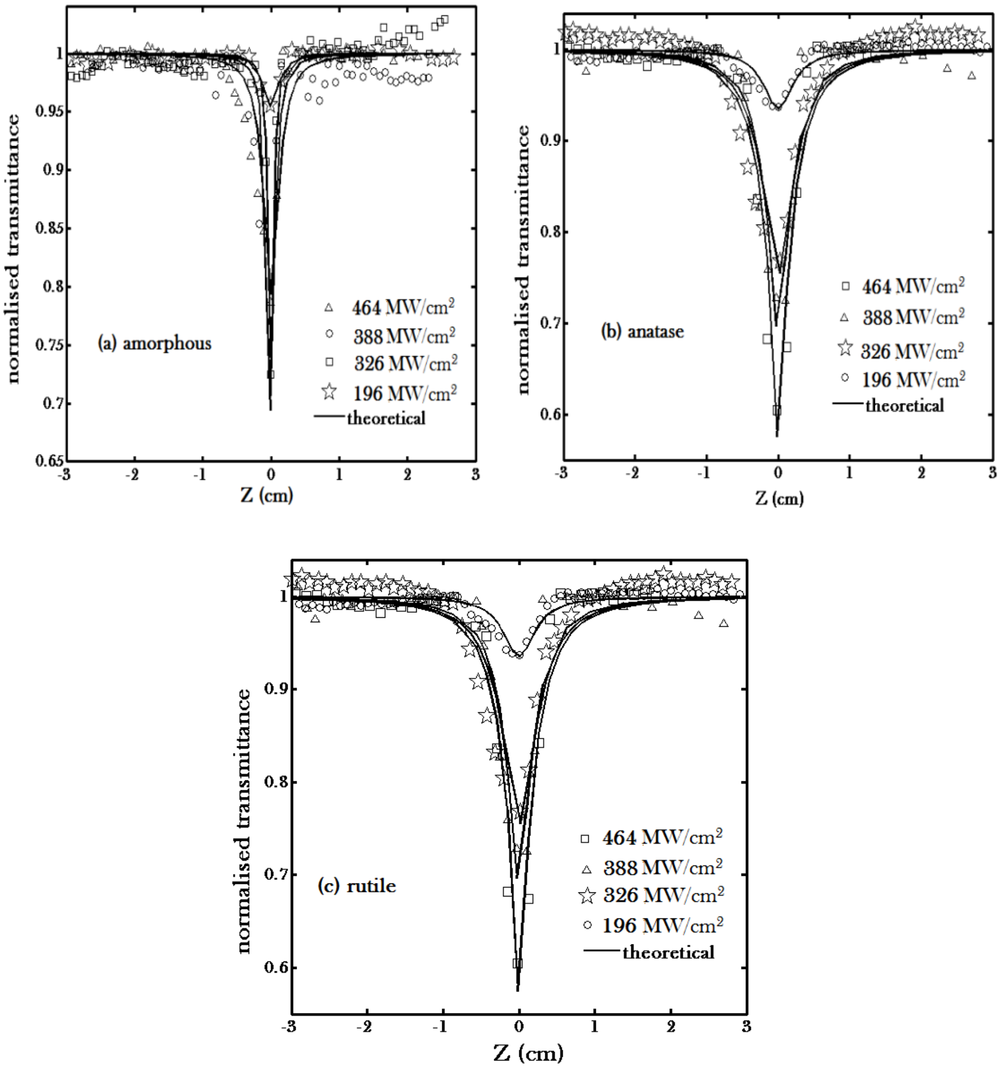

Figure 3.10: *Open aperture Z-scan curves of amorphous, anatase and rutile* TiO_2 *at different laser powers (in MW/cm*^{2}*). Solid line represents the theoretical curve.*

Figure 3.10 represents the open aperture Z-scan of amorphous, anatase and rutile TiO_2 at different powers. It is found that as the power increases the nonlinearity decreases, as indicated by the decreasing value of β in figure 3.11. This may be due to the removal of an appreciable fraction of photocarriers from the ground state. Thus when the incident intensity exceeds the saturation intensity, the nonlinear absorption coefficient of the medium decreases. Similar results were obtained for other phases of TiO_2 nanoparticles.

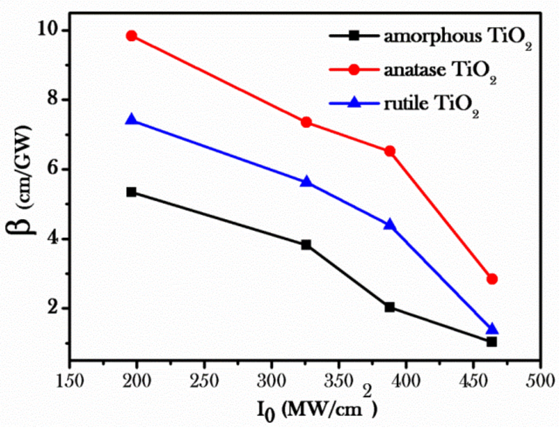

Figure 3.11: *Variation of nonlinear absorption coefficientβ with input irradiance intensity* I_0.

When we plot the $\chi^{(3)}$ with corresponding band gap, we get a nonlinear curve which is shown in figure 3.12.

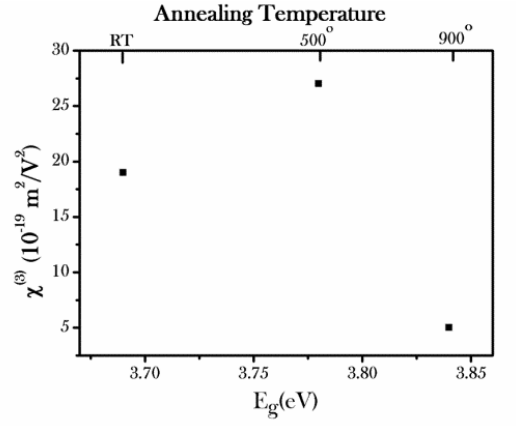

Figure 3.12: *Dispersion of* χ^3 *with band gap Eg and annealing temperature of* TiO_2 *nanoparticles.*

v. Optical Limiting Studies

Figure 3.13 illustrates the optical limiting response of samples at an input laser intensity of 196 MW/cm^2. The optical limiting threshold is seen to decrease with increase in temperature and hence particle size. But as expected rutile phase does not have lower threshold than anatase phase and that may be due to its reduced non linearity. The optical limiting threshold is the corresponding fluence value at which the deviation from linearity in the normalized transmittance is observed[28]. It is obvious that lower the optical limiting threshold better the optical limiting material. Thus it is concluded that annealing temperature and hence particle size has a significant effect on the optical limiting performance of TiO_2 samples. The optical constants of different phases of TiO_2 nanoparticles are summarised in table 3.1.

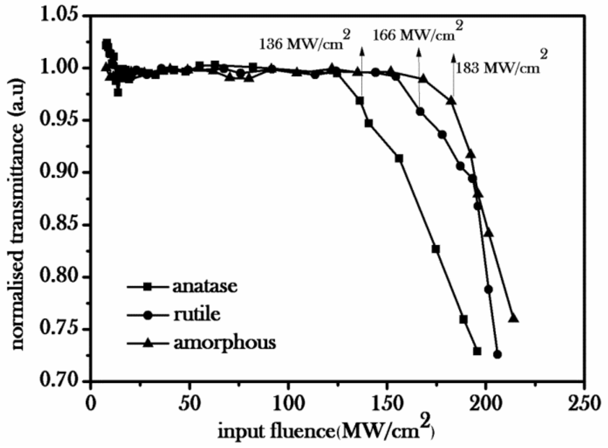

Figure 3.13: *Optical limiting response of various forms of TiO_2.Anatase is found to have superior limiting ability than amorphous and rutile TiO_2.*

Crystalline phase of TiO_2 nanoparticles	**Nonlinear absorption coefficient (m/W) (β)x10^{-10}**	**Nonlinear refractive index (m^2/W) (n_2)x10^{-17}**	**Im $\{\chi\}^3$ x 10^{-20} (m^2/V^2)**	**Re $\{\chi\}^3$ x10^{-19} (m^2/V^2)**	**$\{\chi\}^3$ x10^{-19} (m^2/V^2)**	**Optical limiting threshold (MW/cm^2)**
amorphous	4.509	3.646	4.316	5.412	5.43	183
anatase	6.953	8.235	7.841	27.108	27.12	136
rutile	5.802	6.937	6.008	19.300	19.31	166

Table 3.1: *Measured values of optical constants for various phases of TiO_2 nanoparticles.*

vi. Thermal Diffusion Studies

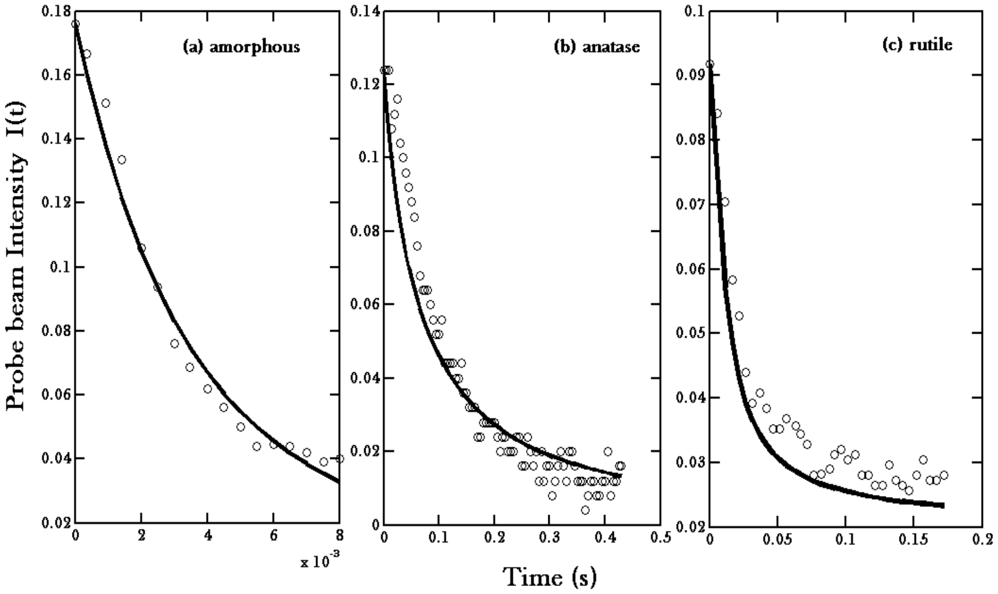

Figure 3.14: *Decay curve using probe beam intensity in thermal lens experiment for TiO_2 nanoparticles (a) amorphous (b) anatase (c) rutile.*

In order to confirm the role of thermal non linearity thermal lens experiment was performed [29].The excitation source used was a continuous wave (CW), diode pumped solid state laser (DPSS) emitting 532 nm radiation with a maximum power of 150 mW. A 2 mW He–Ne used as the probe, is arranged to be collinear with the pump, using a dichroic beam splitter. Figure 3.14 shows the experimental thermal lens development curve and theoretical curve fitting for amorphous, anatase and rutile TiO_2. The solid curve represents the theoretical fitting while the circles represent the experimental data. Thermal diffusivity values obtained from the experiment are calculated and are given in the table 3.2.

Samples	Thermal diffusivity T_D (mm^2/s)
Amorphous TiO_2	0.0124
Anatase TiO_2	0.0076
Rutile TiO_2	0.0114

Table 3.2: *Measured values of thermal diffusivity for various phases TiO_2 nanoparticles.*

Studies show that thermal diffusivity of TiO_2 nanoparticles varies with the subjected temperature. Anatase TiO_2 nanoparticles has the lowest value of thermal diffusivity followed by rutile and amorphous phases respectively. Non-radiative recombination gives rise to the origin of thermal energy. Defect states often acts as such non-radiative recombination centres. As the density of defect states increases number of such non-radiative recombination centres also increases resulting in the scattering of thermal waves by phonon motion thereby resulting in the reduction of thermal diffusivity. As deduced from previous studies, anatase phase of TiO_2 has more number of such surface states and oxygen vacancies which consequently act as defect states.

3.4 Conclusions

TiO_2 nanoparticles were synthesised using sol-gel method. The as obtained nanoparticles were subjected to thermal treatment to obtain the anatase and rutile phase of TiO_2. The optical absorbance spectra indicated a relative red shift with respect to the amorphous phase indicating an increase in size of the nanoparticles with annealing temperature. The fluorescence emission studies showed four peaks, which were found to be generated from excitonic as well as surface state transitions. Nonlinear optical response studies using nanosecond laser displayed RSA explained through two photon absorption followed by the dominant role played by excitons. The optical limiting thresholds were calculated for all the three phases and results displayed that anatase showed better limiting capability than the amorphous or rutile phase of TiO_2. The values for nonlinear susceptibility of amorphous, anatase and rutile phases were found to be $5\text{x}10^{-19}\text{m}^2/\text{V}^2$, $27\text{x}10^{-19}\text{m}^2/\text{V}^2$ and $19\text{x}10^{-19}\text{m}^2/\text{V}^2$, respectively. Thermal lens experiment was performed to confirm the role of thermal effects in optical non linearity of the TiO_2 samples. Anatase TiO_2 nanoparticles has the lowest value of thermal diffusivity followed by rutile and amorphous phases respectively which can be attributed to presence of more defect states.

3.5 References

---

[1] D.F. Eaton. (1991). “Nonlinear optical materials”. *Science* , 253, 281–287.

[2] “Molecular Nonlinear Optics”, edited by J. Zyss (Academic, New York, 1994).

---

[3] Divya, S., Sebastian, I., Nampoori, V. P. N., Radhakrishnan, P., & Mujeeb, A. (2014). "Non-resonant excitonic effects on the third order nonlinear properties of TiO_2: From amorphous to rutile phase". *Opt. Laser Technol., 56,* 207-210.

[4] G.J. You, P. Zhou, Z.W. Dong, C.F. Zhang, L.Y. Chen, S.X. Qian, (2007) . "Ultrafast third-order nonlinear optical response of Cu:Bi_2O_3 nanocomposite films". *Phys. B,* 393 , 188-194.

[5] Lee, H. W., Lee, K. M., Lee, S., Koh, K. H., Park, J. Y., Kim, K., & Rotermund, F. (2007). "Ultrafast third-order optical nonlinearities of vertically-aligned ZnO nanorods". *Chem. Phys. Lett.*, *447*(1), 86-90.

[6] Han, Y. B., Han, J., Ding, S., Chen, D., & Wang, Q. (2005). "Optical nonlinearity of ZnO microcrystallite enhanced by interfacial state". *Opt. Express, 13*(23), 9211-9216.

[7] Zhou, Y., Ma, R., Ebina, Y., Takada, K., & Sasaki, T. (2006). "Multilayer hybrid films of titania semiconductor nanosheet and silver metal fabricated via layer-by-layer self-assembly and subsequent UV irradiation". *Chem. Mater., 18*(5), 1235-1239.

[8] Kuang, D., Brillet, J., Chen, P., Takata, M., Uchida, S., Miura, H., & Grätzel, M. (2008). "Application of highly ordered TiO_2 nanotube arrays in flexible dye-sensitized solar cells". *ACS nano., 2*(6), 1113-1116.

[9] Umezawa, N., Janotti, A., Rinke, P., Chikyow, T., & Van de Walle, C. G. (2008). "Optimizing optical absorption of TiO_2 by alloying with TiS_2". *Appl. Phys. Lett., 92*(4), 041104.

[10] Park, N. G., Van de Lagemaat, J., & Frank, A. J. (2000). "Comparison of dye-sensitized rutile-and anatase-based TiO_2 solar cells". *J. Phys. Chem. B., 104*(38), 8989-8994.

[11] Tan, Y. N., Wong, C. L., & Mohamed, A. R. (2011). "An Overview on the Photocatalytic Activity of Nano-Doped-TiO_2 in the Degradation of Organic Pollutants". *ISRN Mater.Sci., 2011.*

[12] Banerjee, A. N. (2011). "The design, fabrication, and photocatalytic utility of nanostructured semiconductors: focus on TiO_2-based nanostructures". *Nanotechnol. Sci. Appl., 4,* 35.

[13] E. Haro-Poniatowski, R. Rodriguez-Talavera, M. de la Cruz Here- dia, O. Cano-Corona, and R. Arroyo-Mudllo. (1994). "Crystallization of nanosized titania particles prepared by the sol-gel process" *J. Mater. Res.* 9(8), 2102-2108.

[14] Liu, Pei-Sheng, Wei-Ping Cai, Li-Xi Wan, Ming-Da Shi, Xiang-Dong Luo, and Wei-Ping Jing T (2009). "Fabrication and characteristics of rutile TiO_2 nano particles induced by laser ablation" *Nonferr. Metal Soc.* 19 743-747.

[15] Iliopoulos, K., Kalogerakis, G., Vernardou, D., Katsarakis, N., Koudoumas, E., & Couris, S. (2009). "Nonlinear optical response of titanium oxide nanostructured thin films". *Thin Solid Films, 518*(4), 1174-1176.

[16] Tang, H., Berger, H., Schmid, P. E., & Levy, F. (1994). "Optical properties of anatase (TiO_2)". *Solid State Commun., 92*(3), 267-271.

---

[17] Mo, S. D., & Ching, W. Y. (1995). “Electronic and optical properties of three phases of titanium dioxide: rutile, anatase, and brookite”. *Phys. Rev. B, 51*(19), 13023.

[18] Sheik-Bahae, M., Said, A. A., Wei, T. H., Hagan, D. J., & Van Stryland, E. W. (1990).“Sensitive measurement of optical nonlinearities using a single beam”. *IEEE J. Quantum. Elect, 26*(4), 760-769.

[19] Nithyaja, B., Misha, H., & Nampoori, V. P. N. (2012). “Synthesis of silver nanoparticles in dna template and its influence on nonlinear optical properties”. *Nanoscience and Nanotechnology, 2*(4), 99-103.

[20] Wood, D. L., & Tauc, J. S. (1972). “Weak absorption tails in amorphous semiconductors”. *Phys. Rev. B, 5*(8), 3144.

[21] Mathew, S., kumar Prasad, A., Benoy, T., Rakesh, P. P., Hari, M., Libish, T. M., ... & Vallabhan, C. P. G. (2012). “UV-visible photoluminescence of TiO_2 nanoparticles prepared by hydrothermal method”. *J. Fluoresc., 22*(6), 1563-1569.

[22] Tang, H., Berger, H., Schmid, P. E., Levy, F., & Burri, G. (1993). “Photoluminescence in TiO_2 anatase single crystals”. *Solid State Commun., 87*(9), 847-850.

[23] J.Lima-de-Faris. (1994)“Structural Mineralogy”, *Kluwer AcademicPublishers, Dordrecht,*682

[24] Hanamura, E. (1988). “Rapid radiative decay and enhanced optical nonlinearity of excitons in a quantum well”. *Phys. Rev. B, 38*(2), 1228.

[25] E. S. Koteles, in Excitons, E. I. Rashba and M. D. Sturge, 1982 eds. (North-Holland, New York,) 83.

[26] Chiodo, L., García-Lastra, J. M., Iacomino, A., Ossicini, S., Zhao, J., Petek, H., & Rubio, A. (2010). “Self-energy and excitonic effects in the electronic and optical properties of TiO_2 crystalline phases”. *Phys. Rev. B, 82*(4), 045207.

[27] Rashba, E. I., & Gurgenishvili, G. E. (1962). “Edge absorption theory in semiconductors”. *Sov. Phys. Solid State, 4*(4), 759-760.

[28] Divya, S., Sebastian, I., Nampoori, V. P. N., Radhakrishnan, P., & Mujeeb, A. (2014). “Tailoring optical properties of TiO_2 in silica glass for limiting applications”. *Chinese Phys. B, 23*(3), 034210.

[29] Joseph, S. A., Hari, M., Mathew, S., Sharma, G., Hadiya, V. M., Radhakrishnan, P., & Nampoori, V. P. N. (2010). “Thermal diffusivity of rhodamine 6G incorporated in silver nanofluid measured using mode-matched thermal lens technique”. *Opt. Commun., 283*(2), 313-317.

Chapter 4

Morphology Dependent Fluorescence and Nonlinear Studies on TiO_2 Nanostructures

---

Abstract

Nanostructured TiO_2 in different shapes such as nanowires, nanosheets, nanospheres as well as nanoflowers have been prepared and characterized. Photoluminesence studies showed that for the nanoflower, its petal like structures act as light collecting organs and the emitted wavelengths get eventually absorbed after multiple reflections suggesting that the special structures have significant influence on the optical properties of TiO_2 crystals. Nonlinear optical properties were measured at 532 nm using open and closed aperture Z-scan technique with respect to the shape. NLO behaviour of the nanostructured TiO_2 is found to be shape dependent in suspensions at the investigated wavelengths and is accounted in terms of effective surface-to-volume ratio of the structures. The values of different optical constants, viz ; β,n_2, $\chi^{(3)}$ for different morphological structures were evaluated and compared. The optical limiting thresholds of the samples were also investigated and were found to decrease with increase in the net light matter interaction area of the sample.

Results of this chapter are published in :

i. S. Divya et.al. (2014) *Appl. Phys. A* 114(4) 1079-1084.
ii. S. Divya et.al. (2013) *Adv. Electrochem.*1(2), 124-127.

4.1 Introduction

Characteristic properties of a material are determined by the type of motion being undertaken by its governing electrons, which in turn is determined by the allowed space in which they are confined. Once the confinement process sets in, quantization occurs and hence energy levels become well defined and distinct. Quantum confinement effects are sensitive to the size and shape of the nanoparticle. Such size and shape dependent confinement systems have been under continuous scientific attention from past few years due to their morphology dependent physical properties such as large binding energy, giant oscillator strength, large non linearity and short decay time. With the variation in the size and shape of the nanomaterials, electronic structure of the material also varies. Unlike the change in size, the change in shape often leads to a change in electronic state symmetries and their characteristics, thus the relevant phenomena are much promising. At its basic level, the change in electronic structure is the change in single-particle electronic states. This includes the state energy, the overall shape of the wave function, the symmetry, the polarization, and the localization. Scientific community has been continuously engaged in the synthesis of novel structures and shapes eg. nanorods, nanoribbons, nanocubes, nanospheres, nanoflower, nanoprism etc. of various nanoparticles for harnessing their potential applications [1,2,3,4]. One of the main attractions of such confined electronic system is that the nonlinear responses of such materials show remarkable dependence on particle morphology. Materials with large nonlinear susceptibilities and fast response time are widely reconnoitred for their potential application in the field of photonic devices such as all-optical switches and optical correlators. The linear and nonlinear optical (NLO) properties of nanostructured materials are believed to be drastically influenced by quantum confinement effect and therefore are very different from their respective bulk form and are among the widely investigated area by the researches due to their promising applications in optoelectronic field. The dependence of optical properties on morphology can be termed as non-local response. When a material is exposed to an intense beam, the density of induced dipole moment at a point is a cumulative effect of the electric fields at surrounding points as well due to the confined extension of wave functions of relevant energy states [5,6,7]. This should be described as the relationship between the internal field and induced dipole density in the nonlocal form. Along these lines, the spatial distribution of the internal field is determined reliably with that of induced polarization. Thus, for a resonant light, the spatial variation of the internal field becomes analogous with that of induced polarization, and in a mesoscopic system where the polarization wave is coherent in the whole sample, the magnitude and the spatial distribution of the internal field significantly depends on the “size, shape and internal structure’’ of the sample. Hence induced polarization depends on the magnitude and spatial distribution of internal fields, which in turn depends on the overall morphology and internal structure of the sample.

TiO_2 with its unique characteristics such as high direct band gap and surface structure has promising applications in fields such as photocatalysis, environmental pollution control, solar cells and so on[8,9,10,11]. Usually, the performance of TiO_2 nanomaterials for these applications is governed by its morphological, structural and textural characteristics. By undertaking morphology controlled synthesis and growth, size and shape of the nanoparticles can be tailored which in turn controls the structural properties of the semiconductor for various technological applications. In this chapter, we emphasize on the dependence of nonlinear optical property on different shapes viz, nanowire, nanosheet, nanosphere and nanoflower of TiO_2 and henceforth on its linear and third order nonlinear optical susceptibility.

4.2 Experimental

TiO_2 nanowires, nanosheets, nanoflower and nanospheres were synthesised as reported by other groups[12,13,14,15].

TiO_2 nanowires: TiO_2 nanowires with pure anatase phase were prepared from a modified hydrothermal process. 6g of TiO_2 nanopowder was mixed with 33 mL NaOH (15 M) aqueous solution with stirring at room temperature for 10 min. The mixture was then heated at 170°C for 3 days in a 125 mL Teflon-lined autoclave. The precipitates so obtained were washed with dilute HCl and water for several times. The final product was obtained by calcining the washed precipitates at 700°C for 2hour.

TiO_2 nanosheet: The synthesis of anatase TiO_2 nanosheets was carried out by a modified hydrothermal method. Tetrabutyl titanate ($Ti(OBu)_4$) and hydrofluoric acid (HF) were used as received without further purification. 5 mL of $Ti(OBu)_4$ was introduced into a dried 50 mL Teflon-lined stainless steel autoclave. Then 0.4–0.6 mL of HF solution was dropped into the above liquid slowly. The autoclave was then heated to 160–180ºC and kept for 24 h in an electric oven. The white precipitate so obtained was separated by using centrifugation method. The products were washed thoroughly with absolute ethanol, 0.1 M NaOH aqueous solution and deionized water for at least 3 times to remove the residual contamination and fluorine species. Finally the product was dried at 80ºC in vacuum overnight.

TiO_2 nanoflower: In a typical case, 1 mL tetrabutyl titanate (TBOT) and 5 mL glycerol were added separately in 15 mL each of ethanol under magnetic stirring. The two solutions were mixed together, followed by stirring for 10 min. The resulting clear solution was transferred into a 50 mL Teflon-lined stainless steel autoclave, which was heated to 180ºC and maintained for 24h .Subsequently, the autoclave was cooled to room temperature naturally. The obtained samples were filtered, washed with ethanol and dried at 80ºC in air. The as-prepared samples were then annealed at 450ºC in air for 3 h.

TiO_2 nanospheres: In a typical synthesis, 0.85 mL of titanium(IV) butoxide was injected to a mixture of 0.2 mL of aqueous solution of sodium chloride (4×10^{-4}M) and 50 mL of ethanol at ambient temperature in an inert atmosphere under magnetic stirring. Stirring was discontinued after sometime to prevent the agglomeration of the particles. After two hours, the nanospheres were collected by centrifugation.

To confirm the geometry of the obtained nanoparticles, scanning electron microscopy (SEM) measurements were performed. The prepared TiO_2 samples in powder form, dispersed in deionized water were characterised by optical absorption measurements using a (JascoV-570) UV/VIS/IR spectrophotometer. Nonlinear absorption coefficient (ß) and nonlinear refractive index (n_2) of the samples were calculated using open and closed aperture Z-scan technique comprising of Nd-YAG laser (532 nm, 7 ns, 10 Hz). Z-scan technique developed by Bahae.et al is a single beam method for measuring the sign and magnitude of nonlinear refractive index n_2 and has sensitivity comparable to interferometry methods. The sample was moved in the direction of light incidence near the focal spot of the lens with a focal length of 200 mm. The Rayleigh length z_0 is estimated to be 7.4 mm, much greater than the thickness of the sample cuvette (1mm), which is an essential prerequisite for Z-scan experiments. The data were analysed by using the procedure described by Sheikh Bahae et. al.[16] and the non-linear coefficients were obtained by fitting the experimental Z-scan plot with the theoretical ones.

4.3 Results and Discussions

i. Structural Studies: SEM, TEM and XRD

Figure 4.1(a, c, d & e) represents the SEM images of TiO_2 nanowire, nanosheets, nanospheres and nanoflower. SEM image of TiO_2 nanowires showed higher degree of accumulation and hence TEM analysis was performed and is shown in figure 4.1b. The degree of accumulation decreased by changing the shape of TiO_2 to nanosheets, nanospheres and nanoflower. Figure 4.1(f) shows the XRD pattern of the samples. The crystallite phase of TiO_2 was independent of shapes and only anatase phase was observed. The four main diffraction peaks at 2ϴ viz. 25.8º, 37.7º, 47.8º, 55.0º correspond to the (101), (004), (200) and (211) crystal phase of anatase TiO_2.

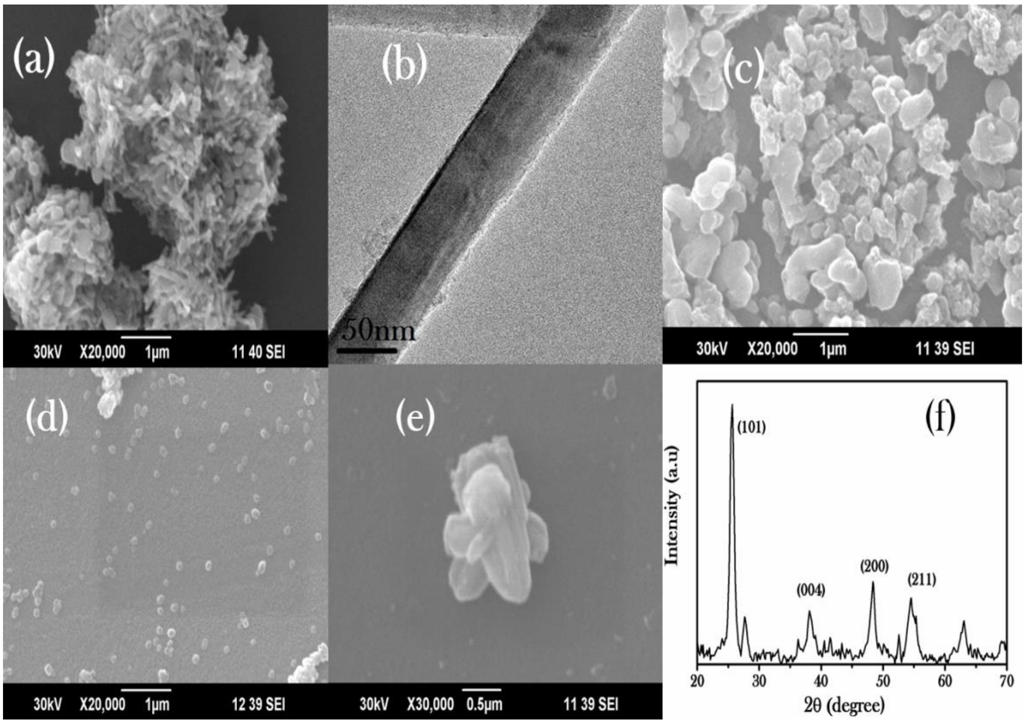

Figure 4.1: *Morphological images of the nanostructured TiO_2 (a) SEM of nanowire (b) TEM image of nanowire (c) SEM image of nanosheet (d) SEM image of nanosphere (e) SEM image of nanoflower. (f) XRD pattern of the sample. All the samples showed similar XRD pattern.*

ii. Absorption Studies

The absorption spectra of the different nanostructured TiO_2 suspended in de-ionized water were characterized with a UV-visible spectrophotometer and are shown in figure 4.2.

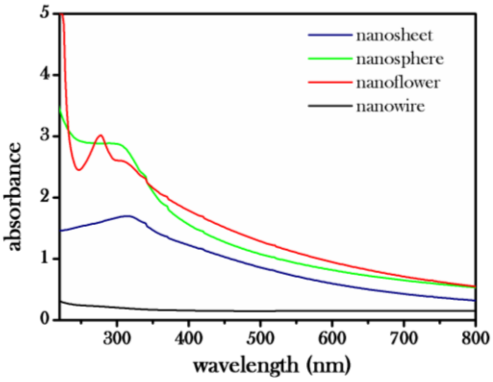

Figure 4.2: *Absorption spectra of the TiO_2 nanostructures.*

It is observed that the TiO_2 3D nanoflower showed the highest absorption in the UV light among all the samples. It could be due to the fact that absorption is significantly dependent on the morphological structure of the sample. It is possible that intertwined petal-like structures of the TiO_2 nanoflower sample allows multiple reflections of the light which eventually increases the density of photogenerated electrons. This is confirmed by the photoluminescence spectra.

iii. Photoluminescence Studies

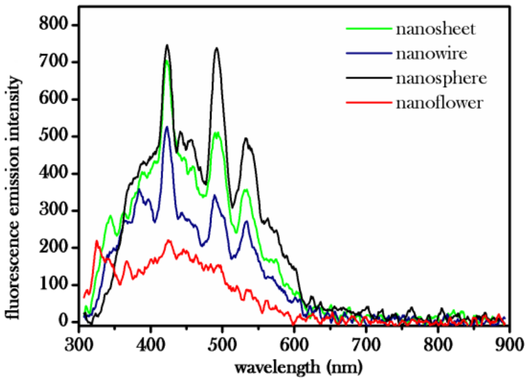

Figure 4.3: *PL spectra of the TiO_2 nanostructures at an excitation wavelength of 255 nm. Flower-like morphology has the lowest emission peak due to the absorption of emitted wavelengths after multiple reflections.*

Figure 4.3 represents the photoluminescence spectra of TiO_2 nanostructures. It shows the room-temperature photoluminescence (PL) spectra of the different TiO_2 nanostructures. Most of the samples in the figure show multiple emission peaks at 421 nm, 491 nm and 533 nm which are considered as characteristic peaks for the anatase phase of TiO_2. Emission at 387 nm is due to annihilation of excitons while remaining three peaks could be arising from surface states[17]. The surface state is generally localized within the band gap of the semiconductor and they can trap the excited state electrons and can lead to higher wavelength emissions. The oxygen vacancies and surface hydroxyl groups are the dominant sites for trapped electrons and holes. These trapped carriers which are captured by oxygen vacancies and surface hydroxyl groups, contribute to the visible luminescence in these nanoparticles. Peaks at 421 nm, 491 nm, and 533 nm are assigned to the surface state emissions and are due to the recombination of trapped electron–hole pairs arising from dangling bonds in the TiO_2 nanoparticles. For nanoflower, peaks are almost on the verge of disappearance and this could be due to the fact that its petal like structures acts as light collecting organs such that the emitted wavelengths eventually get absorbed after multiple reflections. These PL results indicate that the special structures have significant influence on the optical properties of TiO_2 crystals.

iv. Optical Nonlinear Studies

Figure 4.4 shows the open aperture Z-scan response of the samples at 532 nm for a power density of 388 MW/cm^2. All the samples exhibited reverse saturable absorption (RSA) with the depth of the valley indicating their nonlinear ability. Among the samples, nanoflowers showed the best nonlinear optical potential followed by nanospheres. As evident, nanoflowers have the largest absorption cross section and hence the largest RSA effect. In semiconductor nanocrystals, the surface chemistry of the localized trapping states contributes to the optical nonlinear properties in a major way. When the linear absorption cross-section of the trapped states is higher than that of the ground states, direct excitation from these surface-trapped states will promote the photocarriers to higher energy levels in the nanocrystal, giving rise to the optical nonlinearity[18]. Hence the nonlinear optical properties exhibited by these nanostructures depend on their linear absorption cross section, governed by their surface to volume ratios. The surface to the volume ratio of the prepared nanostructures follows the order nanowire<nanosheet<nanosphere<nanoflower. It is assumed that the random orientation of these nanostructures further strengthens the nonlinear optical phenomenon.

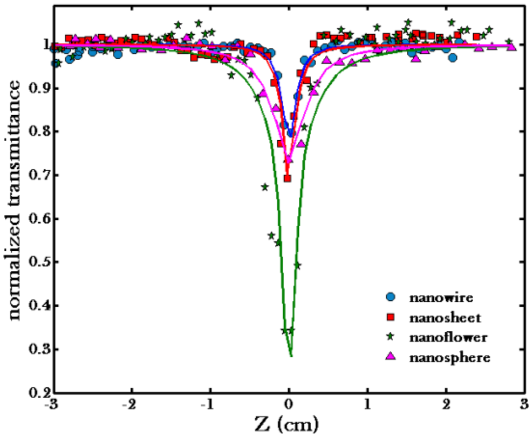

Figure 4.4: *Normalized transmittance as a function of position for different morphological TiO_2 nanostructures in the open aperture scheme at 532 nm with a laser power of 388 MW/cm^2. The solid line shows the theoretical fit.*

Apart from this, another major factor that could be attributed to RSA effect is the nonlinear scattering which was observed while on exposure to the laser beam. It might involve photon induced ionization and excitation of the Ti atoms, leading to the formation of rapidly expanding micro plasmas and microbubbles, that can strongly scatter the incident light leading to RSA[19,20]. In this case, the larger the scattering area, the more efficient the NLO scattering, and this further follows the RSA sequence of the nanostructured TiO_2 at 532 nm.

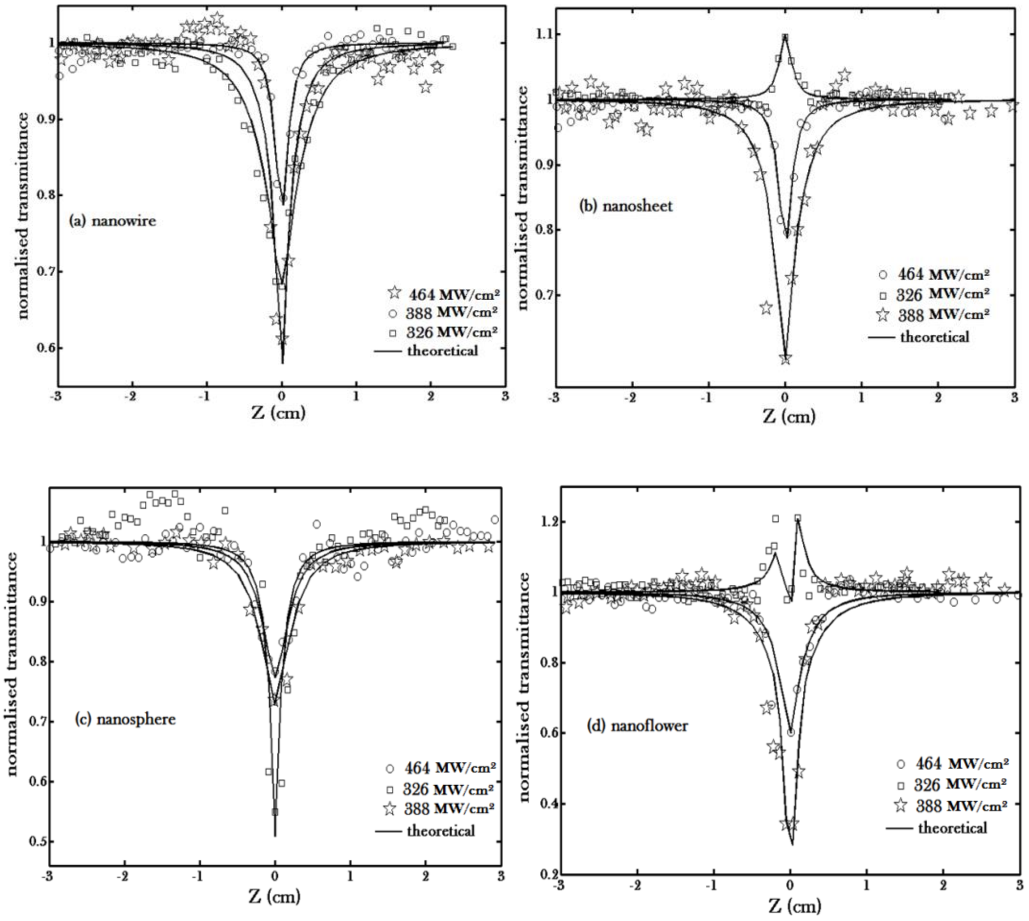

Figure 4.5: *Open aperture Z-scan curves of amorphous, anatase and rutile TiO_2 at different laser powers (in MW/cm^2). Solid line represents the theoretical curve.*

Table 4.1 gives the values of different optical constants of the samples at $388MW/cm^2$. The value so obtained trails our justifications. As evident from the figure 4.5 which shows the variation of open aperture Z-scan traces of different nanostructures at different powers, it can be inferred that the nonlinear response of the crystals depends on the pump power as well as on structural geometry of the sample. As the power increases, the nonlinear absorption coefficient decreases thereby diminishing the third order susceptibility. It is reported that the local field enhancement through the size and structure dependent interfacial interaction among the semiconductor TiO_2 crystals influences the magnitude of the nonlinear absorption[21]. When the Im $\chi^{(3)}$ is plotted with corresponding band gap, we get an almost linear curve which is shown in figure 4.6.

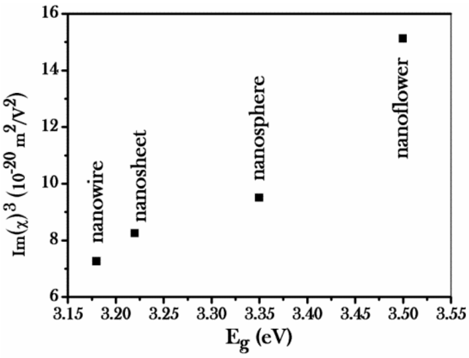

Figure 4.6: *Relationship between Im* χ^3 *and band gap* E_g *for different nanostructures.*

As seen from the figure 4.5, with power variation, switching behaviour occurs for nanoflower. As proved from absorption and photoluminescence studies the petal like structures of nanoflower leads to multiple reflections of the incident light providing an enhanced effective optical path length to confine the light and increases the interaction between the excitation light and TiO_2 crystals. Enhanced optical path length increases the excited state absorption and free carrier absorption leading to bleaching of the ground state band, i.e., in the case of the intraband transition, the ground-state electrons are pumped to the excited-state when the input fluence is increased. The excited electrons are free carriers possessing a whole spectrum of energies, both kinetic and potential; which relax to the ground-state through electron–electron, electron–phonon and phonon–phonon interactions.

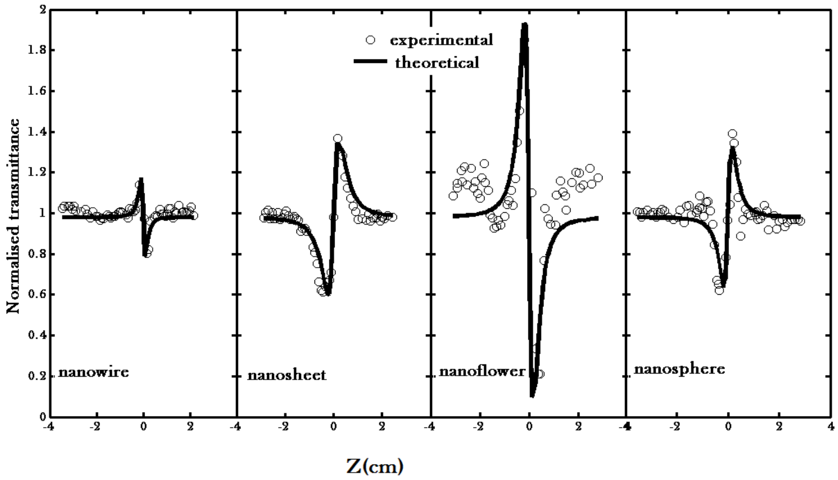

Figure 4.7: *Normalized transmittance as a function of the position for different morphologies in the closed aperture scheme at 532 nm with a laser power of 388 MW/cm*^{2}*. The solid line shows the theoretical fit.*

The closed aperture Z-scan experiment performed on the samples at a laser power of 388 MW/cm^2 is presented in figure 4.7. In order to obtain the phase distortion caused due to the change in refractive index, normalised closed aperture data was divided by the corresponding normalised open aperture data. It is observed that peak-valley as well as the valley-peak of closed aperture Z-scan satisfied the condition $\Delta z \sim 1.7 z_0$ thereby confirming the presence of cubic non linearity[22]. In the figure it is observed that nanowire and nanoflower has peak- valley trace signifying negative nonlinear refractive index whereas the other two structures viz, nanosheet and nanosphere follows a valley–peak trace depicting positive value of nonlinear refractive index. In the case of nanowire, this is a direct consequence of the electron-phonon relaxation in the medium, which is a nonradiative process[23,24]. During electron-phonon interactions, thermalization occurs when electrons lose their energy by externally thermalizing with the lattice. As a result of electron- phonon interaction the immediate vicinity of the irradiated volume is heated up leading to a reduction in the local refractive index, resulting in the self-defocusing of the beam. But as the surface area increases, as in the case of nanosheet and nanosphere, the probability of phonon-phonon interaction would be more than the electron-phonon interaction. Hence larger the surface to volume ratio the faster will be the heat dissipation to the solvent. So with decrease in the nanoparticle dimension thermal non linearity diminishes with the onset of electronic non linearity. In the case of nanoflower, closed aperture trace again switches back signifying negative nonlinear refractive index. This could be due to the fact that in nanoflower, laser excitation can cause radiative relaxation which eventually gets multiply reflected from its various intertwined petal-like structures. Due to the repeated reflection and absorption from its structures thermalization takes place by causing electrons to lose their energy by externally thermalizing within the lattice and hence negative nonlinear refractive index.

v. Optical Limiting Studies

Figure 4.8 represents the optical limiting curve of the TiO_2 nanostructures. The optical limiting threshold is the fluence value at which the deviation from linearity in the normalized transmittance is observed[25,26].The optical limiting threshold is seen to decrease with increase in the light matter interaction area of the sample. Table 4.1 gives the values of optical limiting thresholds of various nanostructures.

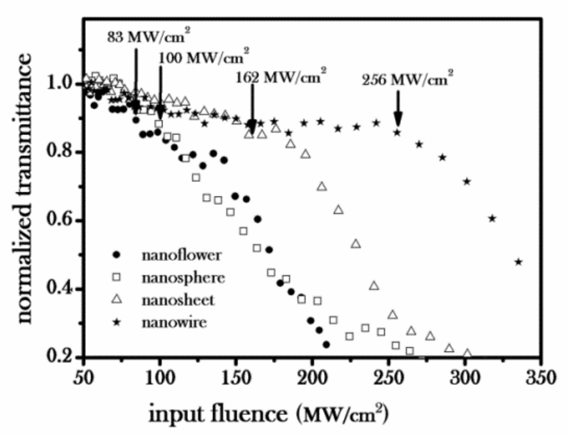

Figure 4.8: *Optical limiting response of the TiO_2 nanostructures with different morphologies. The limiting threshold is found to decrease with increase in the effective light matter interaction area.*

Sample	Nonlinear absorption coefficient (m/W) (β)x10^{-10}	Nonlinear refractive index (m^2/W) (n_2)x10^{-17}	Im $\{\chi\}^3$ x10^{-20} (m^2/V^2)	Re $\{\chi\}^3$ x10^{-19} (m^2/V^2)	$\{\chi\}^3$ x10^{-19} (m^2/V^2)	Optical limiting threshold (MW/cm^2)
nanowire	1.685	-1.738	7.258	-3.387	3.463	256
nanosheet	1.915	3.126	8.249	6.092	6.147	162
nanosphere	2.206	3.477	9.503	6.777	6.843	100
nanoflower	3.509	-6.937	15.118	-13.521	13.554	83

Table 4.1: *Values of different nonlinear optical constants of morphologically different TiO_2 nanostructures.*

vi. Thermal Diffusion Studies

In order to validate our argument justifying the imperative role of thermal non linearity, thermal lens experiment was performed[27]. Dual beam mode-matched thermal lens technique has been used to measure the thermal diffusivity among the different morphological structures of TiO_2.The experimental set up used for the study has been presented in chapter 2. The time evolution of thermal lens signal for the different samples has been shown in figure 4.9 .The solid line represents the theoretical work whereas the circles represents the obtained experimental data. Thermal diffusivity is directly related to thermal conductivity, depending on phonon mean free path which in turn is connected to the crystal structure.

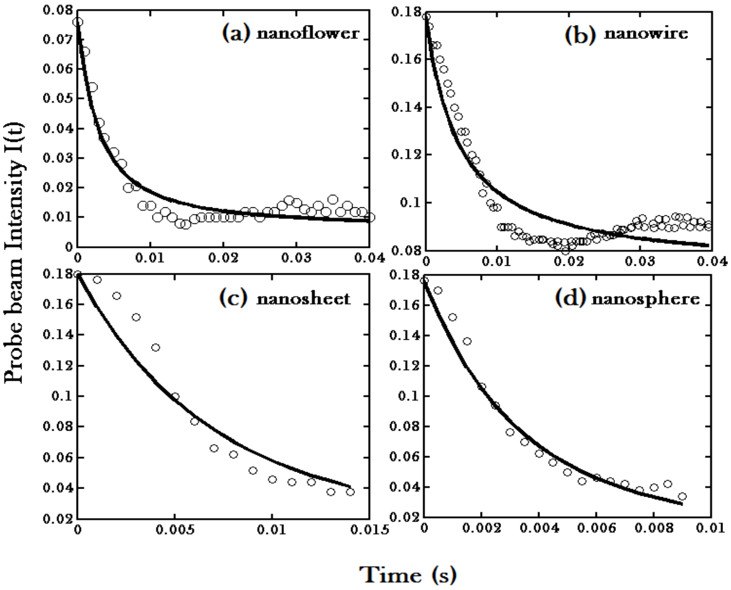

Figure 4.9: *Decay curve for* TiO_2 *nanostructures: (a) nanoflower (b) nanowire (c) nanosheet (d) nanosphere.*

From the table 4.2 it is evident that nanoflower has the lowest thermal diffusivity whereas the nanowire has the highest. Thermal energy mainly arises due to non-radiative recombination. Natural defects play an important role as non-radiative recombination centres. As the number of non-radiative recombination centres increases this leads to a proportional increase in the scattering of thermal energy. Here, hence as the surface area increases, defect centres also increases leading to decrease in the thermal diffusivity.

Samples	Thermal diffusivity T_D (mm^2/s)
nanowire	0.343
nanosheet	0.282
nanosphere	0.210
nanoflower	0.113

Table 4.2: *Measured values of Thermal diffusivity* T_D *for different* TiO_2 *nanostructures.*

4.4 Conclusions

Different TiO_2 nanostructures such as nanowire, nanosheet, nanosphere and nanoflower were synthesised. It was found that the degree of accumulation decreased by changing the shape of TiO_2 from nanowire to nanosheets, nanospheres and nanoflower. PL results showed that each structure had significant influence on the optical properties of TiO_2 crystals. Linear and nonlinear optical properties were studied using optical absorption and open as well as closed aperture Z-scan technique. The nonlinear properties of the nanostructured suspensions were found to be shape dependent. Optical constants for different structures were determined and compared. Among the different structures, nanoflowers showed the highest nonlinear absorption and nonlinear refraction. This phenomenon is explained by rendering the fact that due to its peculiar structure, nanoflower has highest surface to volume ratio and also, its intertwined petal-like structure causes repeated reflection and absorption causing thermal non linearity to take the lead. The optical limiting thresholds of the samples were also investigated and are found to decrease with the increase in the light matter interaction area of the sample. The crucial role played by thermal non linearity was validated by performing the thermal lens experiment.

4.5 References

---

[1] Cao, X., Lan, X., Guo, Y., Zhao, C., Han, S., Wang, J., & Zhao, Q. (2007). "Preparation and Characterization of Bifunctional ZnO/ZnS Nanoribbons Decorated by γ-Fe_2O_3 Clusters". *J. Phys. Chem.C*, *111*(51), 18958-18964.

[2] Cao, H., Wang, G., Zhang, S., & Zhang, X. (2006). "Growth and photoluminescence properties of PbS nanocubes". *Nanotechnology*, *17*(13), 3280.

[3] Xue, C., Millstone, J. E., Li, S., & Mirkin, C. A. (2007). "Plasmon-Driven Synthesis of Triangular Core–Shell Nanoprisms from Gold Seeds". *Angew. Chem.* , *119*(44), 8588-8591

[4] Tian, L., Yao Tan, H., & Vittal, J. J. (2007). "Morphology-controlled synthesis of Bi2S3 nanomaterials via single-and multiple-source approaches". *Cryst. Growth Des.*, *8*(2), 734-738.

[5] Ishihara, H., & Cho, K. (1990). "Cancellation of size-linear terms in the third-order nonlinear susceptibility: Frenkel excitons in a periodic chain". *Phys. Rev. B: Condens. Matter*, *42*(3), 1724.

[6] Ishihara, H., & Cho, K. (1993). "Nonlocal theory of the third-order nonlinear optical response of confined excitons". *Phys. Rev. B: Condens. Matter*, *48*(11), 7960.

---

[7] Cho, K., Ishihara, H., & Ohfuti, Y. (1993). “Resonant size enhancement of induced polarization with particular spatial distribution in optical response of mesoscopic systems”. *Solid State Commun.*, *87*(12), 1105-1108.

[8] Park, Y., Lee, S. H., Kang, S. O., & Choi, W. (2010). “Organic dye-sensitized TiO_2 for the redox conversion of water pollutants under visible light”. *Chem. Commun.*, *46*(14), 2477-2479.

[9] Liu, Z., Zhang, X., Nishimoto, S., Murakami, T., & Fujishima, A. (2008). “Efficient photocatalytic degradation of gaseous acetaldehyde by highly ordered TiO_2 nanotube arrays”. *Environ. Sci. Technol.*, *42*(22), 8547-8551.

[10] Xiong, Z., Dou, H., Pan, J., Ma, J., Xu, C., & Zhao, X. S. (2010). “Synthesis of mesoporous anatase TiO_2 with a combined template method and photocatalysis”. *Cryst. Eng. Comm*, *12*(11), 3455-3457.

[11] WookáKim, K., HeeáJang, Y., YeoláRyu, D., & HaáKim, D. (2010). “On the synergistic coupling properties of composite CdS/TiO_2 nanoparticle arrays confined in nanopatterned hybrid thin films”. *J. Mater. Chem*, *20*(4), 677-682.

[12] Tan,B., & Wu, Y. (2006). “Dye-sensitized solar cells based on anatase TiO_2 nanoparticle/nanowire composites”. *J. Phys. Chem.B*, *110*(32), 15932-15938.

[13] Yang, X. H., Li, Z., Liu, G., Xing, J., Sun, C., Yang, H. G., & Li, C. (2011). “Ultra-thin anatase TiO_2 nanosheets dominated with {001} facets: thickness-controlled synthesis, growth mechanism and water-splitting properties”. *Cryst. Eng. Comm.*, *13*(5), 1378-1383.

[14] Hu, Y., Ge, J., Sun, Y., Zhang, T., & Yin, Y. (2007). “A self-templated approach to TiO_2 microcapsules”. *Nano Lett*, *7*(6), 1832-1836.

[15] Tian, G., Chen, Y., Zhou, W., Pan, K., Tian, C., Huang, X. R., & Fu, H. (2011). “3D hierarchical flower-like TiO_2 nanostructure: morphology control and its photocatalytic property”. *Cryst. Eng. Comm.*, *13*(8), 2994-3000.

[16] Sheik-Bahae, M., Said, A. A., Wei, T. H., Hagan, D. J., & Van Stryland, E. W. (1990). “Sensitive measurement of optical nonlinearities using a single beam”. *IEEE J. Quant. Electron.*, *26*(4), 760-769.

[17] Mathew, S., kumar Prasad, A., Benoy, T., Rakesh, P. P., Hari, M., Libish, T. M.& Vallabhan, C. P. G. (2012). “UV-visible photoluminescence of TiO_2 nanoparticles prepared by hydrothermal method”. *J. Fluoresc.*, *22*(6), 1563-1569.

[18] Asunskis, D. J., Bolotin, I. L., Haley, J. E., Urbas, A., & Hanley, L. (2009). “Effects of surface chemistry on nonlinear absorption of PbS nanocrystals”. *J. Phys. Chem.C*, *113*(46), 19824-19829.

---

[19] Sun, X., Yu, R. Q., Xu, G. Q., Hor, T. S. A., & Ji, W. (1998). “Broadband optical limiting with multiwalled carbon nanotubes”. *Appl. Phys. Lett.*, *73*(25), 3632-3634.

[20] Vivien, L., Lancon, P., Riehl, D., Hache, F., & Anglaret, E. (2002). “Carbon nanotubes for optical limiting”. *Carbon*, *40*(10), 1789-1797.

[21] Lee, H. W., Lee, K. M., Lee, S., Koh, K. H., Park, J. Y., Kim, K., & Rotermund, F. (2007). “Ultrafast third-order optical nonlinearities of vertically-aligned ZnO nanorods”. *Chem. Phys. Lett.*, *447*(1), 86-90.

[22] Sheik-Bahae, M., Said, A. A., & Van Stryland, E. W. (1989). “High-sensitivity, single-beam n_2 measurements”. *Opt. Lett.*, *14*(17), 955-957.

[23] Divya, S., Nampoori, V. P. N., Radhakrishnan, P., & Mujeeb, A. (2014). “Morphology dependent dispersion of third-order optical nonlinear susceptibility in TiO_2”. *Appl. Phys. A*, *114*(4), 1079-1084.

[24] Divya, S., Nampoori, V. P. N., Radhakrishnan, P., & Mujeeb, A. (2013). “Morphological Dependence on the Nonlinear Optical Behaviour of TiO_2 Nanostructures”. *Adv. Electrochem.*, *1*(2), 124-127.

[25] Divya, S., Nampoori, V. P. N., Radhakrishnan, P., & Mujeeb, A. (2014). “Intermediate Ce^{3+} defect level induced photoluminescence and third-order nonlinear optical effects in TiO_2–CeO_2 nanocomposites”. *Appl. Phys. A*, 114(2), 315-321.

[26] Tintu, R., Nampoori, V. P. N., Radhakrishnan, P., & Thomas, S. (2011). “Nanocomposite thin films of $Ga_5Sb_{10}Ge_{25}Se_{60}$ chalcogenide glass for optical limiting applications”. *Opt. Mater.*, 33(8), 1221-1225.

[27] Joseph, S. A., Hari, M., Mathew, S., Sharma, G., Hadiya, V. M., Radhakrishnan, P., & Nampoori, V. P. N. (2010). “Thermal diffusivity of rhodamine 6G incorporated in silver nanofluid measured using mode-matched thermal lens technique”. *Opt. Commun.*, 283(2), 313-317.

Chapter 5

Studies on Optical Properties of TiO_2 Nanocomposites

Abstract

The spectral and nonlinear characterizations of various TiO_2 based nanocomposites prepared by sol gel synthesis were investigated. The optical band gap of TiO_2-SiO_2 and TiO_2-CeO_2 nanocomposites were found to be tuneable. For TiN nanoparticles the irradiated laser wavelength is at resonance with the SPR peak of the nanoparticle. Post excitation absorption spectra revealed interesting phenomenon of photo fragmentation leading to blue shift in band gap and red shift in the SPR. For TiN-PVA linear and nonlinear optical properties were studied using theoretical and experimental method. Theoretical method involved Tichy and Ticha relation pooled with generalised Miller's rule and Wemple –Di Domenico single oscillator model. Experimental tool comprised of Z-scan. The results derived from theoretical method deviated greatly from those obtained from the experimental studies. We believe that such incongruity is due to the SPR property of the TiN nanoparticle. Studies revealed that these nanocomposites could be used as optical limiters and are potential materials for other optoelectronic applications. They can also be employed for the development of efficient nonlinear optical devices with relatively smaller thresholds.

Results of this chapter are published in:

i. S. Divya et.al. (2014) *Chin. Phys. B*, 23(3), 034210.
ii. S. Divya et.al. (2014) *Chin. Phys. B*, 23(3), 034209.
iii. S. Divya et.al. (2014) *Appl. Phys. A*, 114(2), 315-321.
iv. S. Divya et.al. (2014*) Curr. Appl. Phys.*, 14, 93-98.
v. S. Divya et.al. (2014) *Laser Phys. Lett.*, 06,11(8)085401
vi. S. Divya et.al., (2014) *Opt. Mater*,37, 433–438

5.1 Introduction

The field of nanocomposites has been widely recognised as one of the most promising and rapidly evolving research areas. Substantial research has been done in relation to photophysical and photochemical behaviours of single and multicomponent metals and semiconductor nanoclusters. Such composite materials are especially of interest in developing efficient light-energy conversion systems, optical devices and microelectronics. Nanomaterials often have unique properties which enables us to realize composite materials with simultaneous multiple unique properties. In order to evaluate the potential candidature of nanocomposites, it is essential to determine the nanomaterials that can be effectively merged to form nanocomposites and the improved new properties that can be expected from the resultant product. With several advantages such as low cost, availability, non-toxicity and stability, TiO_2 has gained widespread scientific attention. In view of these advantages, TiO_2 can act as an excellent matrix for nanoparticle composite films. These composite films may lead to several advantageous functional optical characteristics. The properties of materials based on a modified TiO_2 matrix have been extensively studied, with special concern to their unique electrochemical, optical, catalytic, and semiconducting and redox properties.

Nonlinear optical effects, such as nonlinear optical absorption, nonlinear optical refraction, second and third optical nonlinearities can be used for making all-optical switches, optical memory, spectroscopy, imaging, ultrashort pulse generation, entangled photon generation and quantum cryptography etc. Generally, the nonlinear optical effects are prominent in high optical intensity regime due to the weak nonlinear optical response exhibited by most naturally occurring materials. As a result, materials possessing large third-order nonlinearities and fast temporal optical response are widely investigated by the scientific community. From the past few years TiO_2 has attracted the scientific attention because of its irreplaceable role in applications related to environmental cleaning and protection, photo catalysis, gas sensing, fabrication of solar cells and batteries. Besides, TiO_2 possesses high refractive index and fast as well as reasonably large nonlinear optical response. Hence to further improve the situation regarding nonlinear materials; it is of interest to tailor the nonlinear properties of TiO_2 by doping it with other potential candidates in relation to their various possible applications. The present chapter deals with the optical characterization of various TiO_2 based nanocomposites viz- TiO_2-SiO_2, TiO_2-CeO_2, TiO_2-N (TiN). Their linear optical studies are performed using absorption and fluorescence spectroscopy whereas nonlinear optical characterization is done using Z-scan. The detailed discussions regarding their material chemistry are presented in the following sections.

5.3 Studies on TiO_2-SiO_2 Nanocomposites

5.3.1 Introduction

The electronic properties of quantum sized semiconductors doped in glass matrix change drastically due to the dielectric confinement created by the glass matrix which in turn improves their nonlinear optical properties. It has been reported that such kind of dielectric confinement leads to remodelling of the electronic band structure which in turn is closely linked to the electronic trap states present either on the crystal surface or in the glass matrix[1]. The presence of excited electrons in these states permanently modifies the absorption and the electronic de-excitation routes[2]. In this chapter, the studies on the modification in the optical properties of TiO_2 caused by the incorporation of SiO_2, is presented. Their nonlinear optical absorption in the off-resonance region is studied by Z-scan technique. The obtained results are discussed in terms of the cumulative effects created due to the enhancement in the dielectric confinement with the amount of SiO_2.

5.3.2 Experimental

The synthesis of the composite is done by simple sol-gel process. Tetraethylorthosilicate (TEOS) [$Si(OC_2H_5)_4$] and Titanium tetrabutoxide (TTBO)[$Ti(OC_4H_9)_4$] were used as precursors for SiO_2 and TiO_2, respectively. TEOS and TTBO were dissolved in absolute ethanol separately to form two pre-solutions. TEOS was first mixed with absolute ethanol in a molar ratio of 1:4, hydrolysed by adding 0.1 N HCl to adjust the water to alkoxy molar ratio to 2:1, and then stirred with a magnetic stirrer at room temperature. For pure TiO_2, TTBO was hydrolysed in absolute ethanol by adding a few drops of concentrated HNO_3 and then stirred for 30 min. The two solutions were mixed with various TEOS/TTBO molar ratios and stirred for 1 h[3].Subsequently amorphous powders obtained from the prepared solutions were heated at 500ºC and 900ºC respectively to obtain the anatase and rutile crystalline counterparts of TiO_2. Various percentage compositions of TiO_2 and SiO_2 were synthesised. In the present discussion, 25T-75S composite refers to 25%TiO_2-75%SiO_2 in the composite. The nanocomposites were characterized by optical absorption recorded using a UV/VIS/IR spectrophotometer. In the present investigation, we have employed the single beam Z-scan technique with nanosecond laser pulses to measure the nonlinear optical absorptive and refractive properties of nanocomposites. The sample is moved in the direction of light incident near the focal spot of the lens with focal length of 20 cm. The Rayleigh length z_0 is estimated to be 7.4 mm, which is much greater than the thickness of the sample cuvette (1mm), which is an essential requirement for Z-scan experiments. The data were analysed using the procedure described by Bahae et. al., and the non-linear coefficients were obtained by fitting the experimental Z-scan plot with the theoretical curves.

5.3.3 Results and Discussions

i. FTIR Studies

Figure 5.1 represents the FTIR spectra of the 25T-75S nanocomposite. Similar results were obtained for all the nanocomposites. The peaks at 1082.69cm^{-1}, 961.15cm^{-1} and 796cm^{-1} are anamorphic stretches of Si-O-Si. The absorption peak at 3463.68cm^{-1} is due to the O-H stretching vibration of free water and its corresponding O-H bending vibration at 1640.94 cm^{-1} due to the chemically adsorbed water[4] . The IR band observed at 961 cm^{-1} indicates the existence of Ti-O-Si chemical bonding as the IR bands observed from around 910 cm $^{-1}$ to around 960 cm^{-1} are widely accepted as the characteristic vibration due to the formation of Ti-O-Si bond[5]. Thus from FTIR spectra it can be confirmed that Ti-Si nanocomposites have been formed.

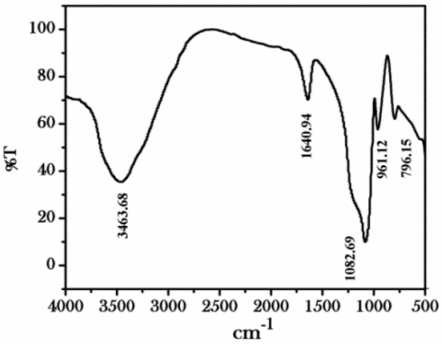

Figure 5.1 : *FTIR spectra of the 25T-75S nanocomposites. The IR band observed at 961 cm^{-1} the existence of Ti-O-Si bond in the nanocomposites.*

ii. Absorption Spectroscopy and XRD Pattern

Optical absorption measurement is an initial step to observe the nanocomposite behaviour. Figure 5.2a gives the room temperature absorption spectra of the nanocomposites. The absorption edge of TiO_2 is found to be blue shifted with respect to their bulk and could be attributed to the quantum confinement effects. The optical band gap can be estimated by plotting $(\alpha h\upsilon)^{2}$ versus photon energy (hυ) based on the relation

$$\alpha h\nu = A(h\nu - Eg)^{1/2} \qquad (5.1)$$

where α is the absorption coefficient, A is a constant and E_g is the band gap . According to this relation, the intercept of the tangent on the photon energy axis corresponds to optical band gap[6] .

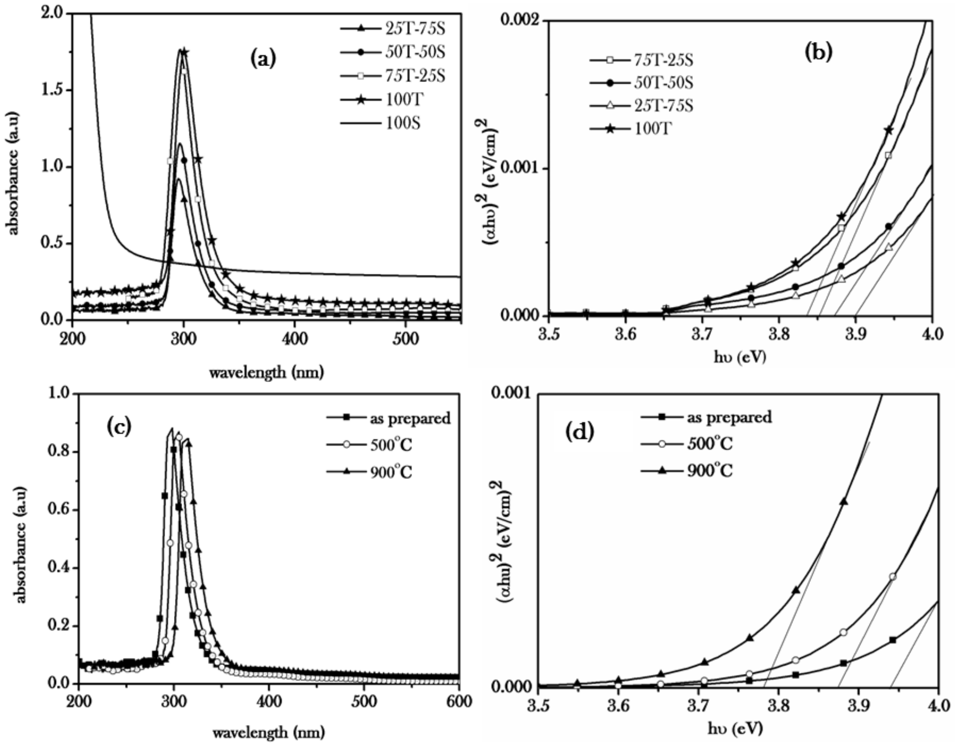

Figure 5.2: *(a). Absorption spectra of the nanoparticles. (b). $(\alpha h\upsilon)^2$ v/s hυ plot for determining the band gap of the nanoparticles.(c). Absorption spectra of the 25T-75S nanocomposite annealed at different temperatures. (d). $(\alpha h\upsilon)^2$ v/s hυ plot for determining the band gap of the nanoparticles.*

All samples have high transmittance in the visible region. Furthermore, higher SiO_2 content results in higher transparency in the visible region, due to the smaller particle size and higher dispersity. From the figure 5.2b, the optical band gaps E_g for 25T-75S, 50T-50S, 75T-25S, 100T are found to be 3.89 eV, 3.83 eV, 3.74 eV, 3.67 eV respectively. Here it is found that as the SiO_2 amount in the nanocomposites increases the band gap also increases. This signifies the diminishing size effect on TiO_2 in the SiO_2 matrix. Figure 5.2c and 5.2d represents the variation in the absorption and band gap of 25T-75S after annealing at 500º and 900ºC respectively. The graph shows that annealing induces the growth of TiO_2 particles dispersed in the glass matrix. The fact that an increasing SiO_2 content resulted in a decreasing particle size has been confirmed by the XRD analysis taken after annealing the samples at 500º and 900ºC is represented in figure 5.3 by using Debye–Scherrer equation.

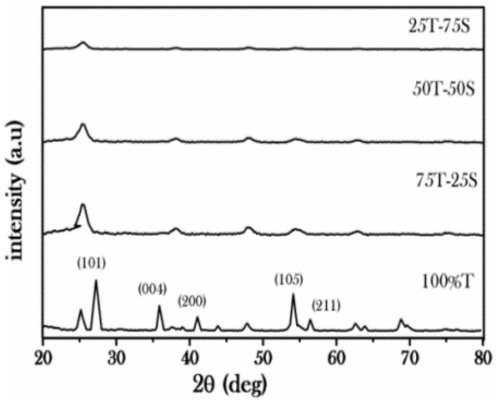

Figure 5.3 : *XRD patterns of composites prepared with various Ti:Si ratios after annealing at 500 ºC. The estimated size were 0.21 nm, 0.108 nm, 0.076 nm, 0.065 nm for 100T, 75T-25S,50T-50S and 25T-75S respectively.*

The pores in mesoporous SiO_2 matrix are highly dispersive and allow the probable flow of TiO_2 sol between adjacent pores. During gel progress, movement of TiO_2 is hindered due to the surface tension of the solution, which probably makes the TiO_2 particles in our sample less aggregated and well dispersed. Thus with increasing annealing temperature, the TiO_2 particles dispersed in the films become bigger, and hence TiO_2 has relatively higher mobility[7].

iii. Photoluminescence Studies

Figure 5.4 shows photoluminescence studies of TiO_2–SiO_2 nanocomposites at room temperature. Spectra show prominent peak at 400nm whose emission peak intensity depend on the volume fraction of TiO_2 in the sample.

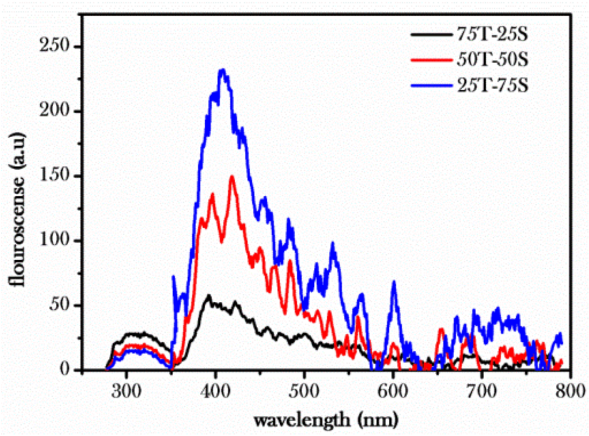

Figure 5.4 : *Pl spectra of TiO_2 –SiO_2 nanocomposites.*

iv. Nonlinear Optical Studies

The technique of Z-scan scheme was employed to study the nonlinear optical properties of the system. In order to ensure that no permanent photo induced change has occurred to the sample during laser irradiation, the experiment was repeated by illuminating the sample at the same position. Under the experimental conditions, laser beam illumination at 532 nm usually corresponds to the two-photon absorption (TPA) process because the photon energy of the 532 nm laser is within the range $E_g < 2h\nu < 2E_g$, where $h\nu = 2.33$ eV. TPA takes place when TiO_2 nanoparticles absorb the energy of two photons to get excited to the higher energy state. The Z-scan traces were made for all compositions with four different input power densities. The Z-scan traces obtained at 465 MW/cm^2 are shown in figure 5.5, and the theoretical fits of equation (as discused in chapter 2) to the experimental data are depicted in the figure by the solid curves.

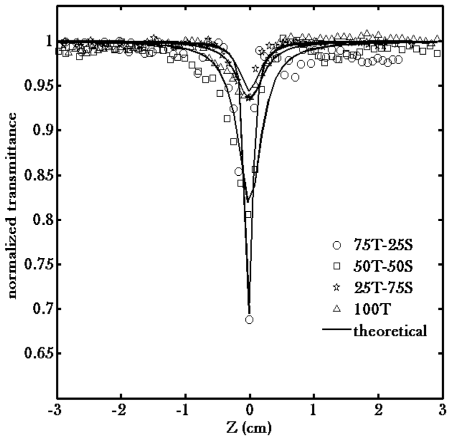

Figure 5.5: *Normalized transmittance as a function of the position in the open aperture Z-scan scheme at 532 nm with a laser power of 465 MW/cm^2 for different nanocomposites.*

Figure 5.6 represents the dispersion of nonlinear absorption coefficient β as a function of the parameter $x = h\upsilon/Eg$, where $h\upsilon$ is the incident photon energy. This form of presentation facilitates the discussion on the physical origin of the nonlinearity. From the Z-scan results, it is obvious that the nonlinear optical properties of nanohybrid thin films shows strong dependence on the titanium oxide loading. The nonlinear absorption coefficient β is found to increase linearly with the percentage of TiO_2 and shows large enhancement in contrast to pure titania. Such large enhancement can be due to the fact that TiO_2 nanoparticles possess distinct surface structures and high surface activity, so that their optical properties will change with surrounding environment. When TiO_2 nanoparticles with large interface are embedded in SiO_2

matrix having smaller dielectric coefficient, there will be a strong charge interaction between them consequently resulting in an electric dipole layer formation at the nanoparticle surface. This effect also depends on the permittivity ratio between particles and the surrounding medium. This surface polarization commonly known as dielectric confinement effect further accelerates the separation of excited charges and thus finally enhances the electric field inside the nanoparticles[197]. Also, it can change the charge density distribution of nanoparticle surface, which further strengthens the anharmonic vibration of surface electron.

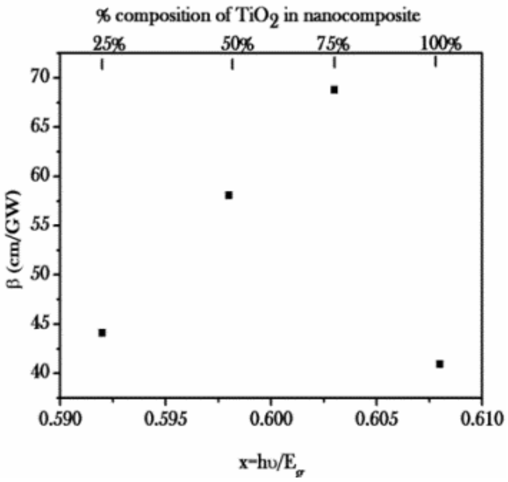

Figure 5.6: *Dispersion of nonlinear absorption coefficient (β) of nanocomposites as a function of the parameter x =hυ/Eg, where hυ is the incident photon energy with percentage of* TiO_2 *in the composition.*

It is reported that enhanced Raman scattering is produced at the interface due to the different permittivity, so that the light intensity inside particles is different from that of surrounding medium. This leads to local-field effect and is responsible for the enhanced nonlinear optical response[8]. Another contributing factor to the enhancement of non-linearity can be imperfect surface modification of titania nanoparticles. There are a lot of physically trapped states or chemical dangling bonds within as well as on the surface of the nanoparticles. Hence surface states are easily formed due to large number of defects at the surface of TiO_2 nanoparticles which eventually make an important contribution towards the enhanced nonlinearity of nanocomposites. The decay time of surface states are sufficiently long enough to induce several trapped electrons, which gets transferred to higher surface states.

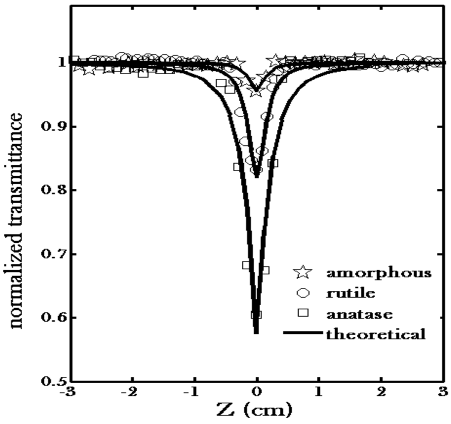

Figure 5.7: *Normalized transmittance as a function of the position in the open aperture scheme at 532 nm with a laser power of 464.8 MW/cm* ^{2} *of 25T-75S for different crystalline forms.*

Figure 5.7 and 5.8 represent the open aperture Z-scan plot for different crystalline forms of TiO_2, anatase and rutile form of 25T-75S formed at 500° and 900°C respectively. It is observed that β increases as TiO_2 changes its phase from amorphous to crystalline. This can be attributed to the fact that as it transforms to crystalline phase with increase in the annealing temperature, size of TiO_2 nanoparticles increases. The resultant enhancement of nonlinear optical properties with increasing dimension in the weak confinement regime originates from the size dependent enhancement of oscillator strength of coherently generated excitons[9].

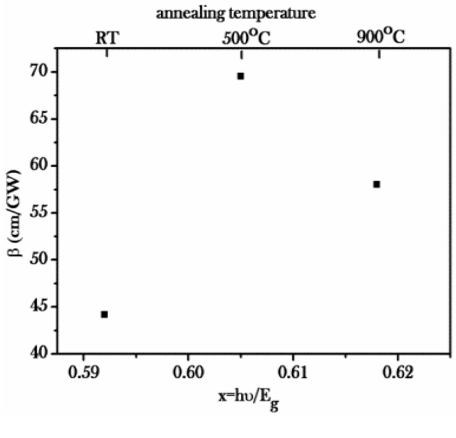

Figure 5.8: *Dispersion of nonlinear absorption coefficient (β) of 25T-75S nanocomposites as a function of the parameter x = hυ/Eg, where hυ is the incident photon energy with temperature. RT represents room temperature.*

The confinement of excitonic wave function is expected to give rise to enhancement of the oscillator strength by a factor of R^3/a_B^3, where R is the particle size and a_B is exciton effective Bohr radius. Interestingly, instead of expected rutile phase, anatase film annealed at 500ºC showed better nonlinear absorption. This is attributed to the fact that anatase is characterised by the presence of more imperfections and disorder. This favours impurity diffusion and disorder creation in anatase crystals[10]. Additionally, anatase phase has self-trapped excitons whereas the rutile phase has free excitons. Nonlinear optical effects are usually enhanced when the associated optical transition has large optical oscillator strength and hence anatase has larger TPA coefficient than the rutile phase[11] .

The curves in figure 5.9 shows closed aperture Z-scan plots for the different samples. In order to obtain the phase distortion caused due to the change in refractive index, normalised closed aperture data was divided by the corresponding normalised open aperture data. It is observed that peak –valley trace of closed aperture Z-scan satisfied the condition $\Delta z \sim 1.7z_0$ thereby confirming the presence of cubic non linearity. The curve follows peak valley trace indicating negative nonlinear refractive index due to self-defocussing. The self –defocussing phenomenon is believed to arise due to thermal nonlinearity. The self-defocussing effect has been reported in most of the semiconductors and is believed to contribute towards optical limiting property.

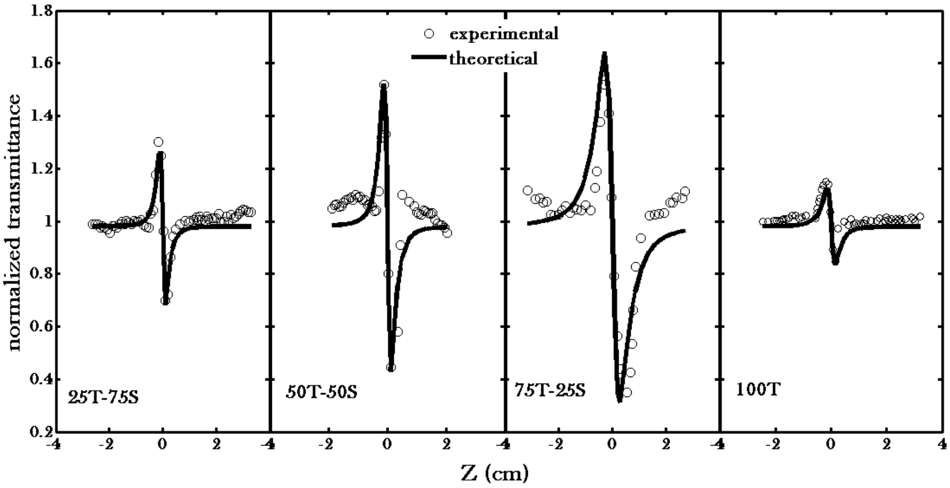

Figure 5.9.: *Normalized transmittance as a function of the position in the closed aperture scheme at 532 nm with a laser power density of 465 MW/cm ^{2} for different nanocomposites.*

Figure 5.10 represents Z-scan plot for different crystalline forms of 25T-75S, anatase and rutile form of TiO_2 formed at 500º and 900ºC respectively. Similar to the results obtained in open aperture, anatase phase has the highest nonlinear refraction.

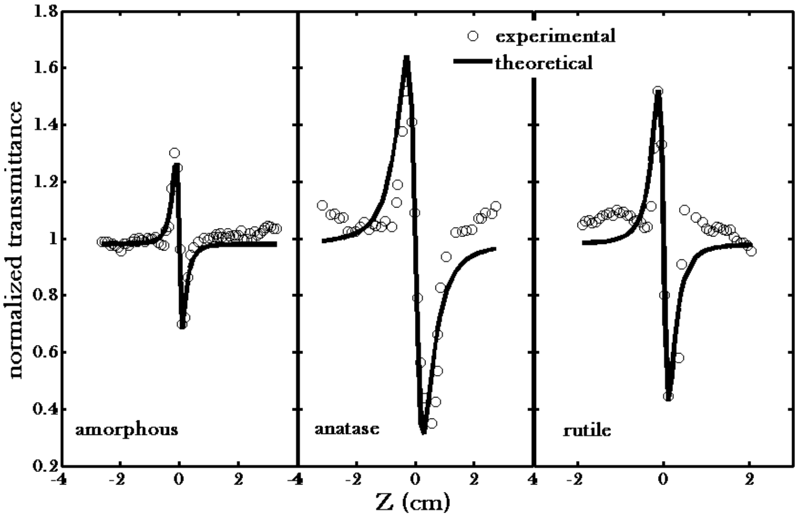

Figure 5.10: *Normalized transmittance as a function of the position in the open aperture scheme at 532 nm with a laser power density of 465 MW/cm ^{2} of 25T-75S for different crystalline forms.*

Table 5.1 gives the values of different optical constants of the samples in amorphous form whereas table 5.2 represents the values of optical constants of 25T-75S in different crystalline forms.

Sample	**Nonlinear absorption coefficient (m/W) (β)x10^{-10}**	**Nonlinear refractive index (m^2/W) (n$_2$)x10^{-17}**	**Im {χ}^{3} x10^{-20} (m^2/V^2)**	**Re {χ}^{3} x10^{-19} (m^2/V^2)**	**{χ}^{3} x10^{-19} (m^2/V^2)**	**Optical limiting threshold (MW/cm^2)**
100T	4.068	1.708	33.569	3.329	4.727	444
25T-75S	4.509	3.646	35.845	6.845	7.726	425
50T-50S	5.715	4.237	45.883	8.035	9.253	345
75T-25S	6.720	6.937	54.789	13.359	14.434	320

Table 5.1: *Values of different optical constants of the TiO_2 nanocomposites in amorphous form.*

Crystalline phase of 25T-75S	Nonlinear absorption coefficient (m/W) (β)x10^{-10}	Nonlinear refractive index (m^2/W) (n_2)x10^{-17}	Im $\{\chi\}^3$ x10^{-20} (m^2/V^2)	Re $\{\chi\}^3$ x10^{-19} (m^2/V^2)	$\{\chi\}^3$ x10^{-19} (m^2/V^2)	Optical limiting threshold (MW/cm^2)
amorphous	4.509	3.646	35.845	6.845	7.726	425
anatase	6.953	8.235	55.321	15.476	16.435	333
rutile	5.802	6.937	46.163	13.037	13.830	387

Table 5.2 : *Values of optical constants of 25T-75S in different crystalline forms of TiO_2 nanocomposites.*

v. Optical Limiting Studies

In recent time, commendable amount of research has been devoted to the field of optical limiting applications. Figure 5.11 represents the optical limiting performance of our nanocomposites. The optical limiting threshold is the corresponding fluence value at which the deviation from linearity in the normalized transmittance is observed. The limiting graph indicates that our nanocomposites show better performance than pure titania.

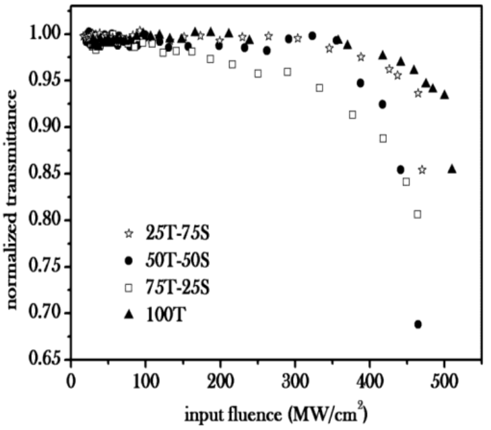

Figure 5.11: *Optical limiting response of nanoparticles at 532 nm for an input power density of 464.8 MW/cm^2. The optical limiting threshold is found to decrease with increasing percentage of TiO_2 in the composition.*

vi. Thermal Diffusion Studies

Properly designed thermal lens technique was used to study the heat transfer through diffusion in TiO_2 –SiO_2 nanocomposites. In the technique as discussed in chapter 2, a laser is used as the heat source and the speed of heat dissipation is measured directly. Thermal diffusivity values obtained from the experiment are calculated and are given in the figure 5.12 and table 5.3.

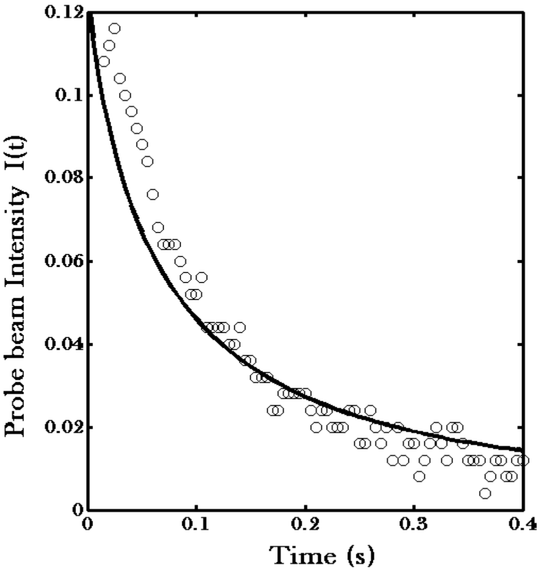

Figure 5.12: *Decay curve for the intensity probe beam for TiO_2 –SiO_2 nanocomposites: amorphous 50T-50S in thermal lens experiment.*

Samples	Thermal diffusivity T_D (mm^2/s)
25T-75S	0.450
50T-50S	0.391
75T-25S	0.326

Table 5.3: *Measured values of thermal diffusivity for the amorphous 50T-50S sample of TiO_2-SiO_2 nanocomposite.*

Studies show that thermal diffusion varies with composition of the nanocomposites. Similar to the non-linear studies thermal diffusivity is directly related to the titania loading. Thermal energy formation mainly takes place due to non-radiative recombination. Defect states play an important role as non-radiative recombination centres. An increase in the defect states results in an increase in such non radiative recombination centres. Local defects give rise to finite frequency modes resulting in the scattering of thermal waves by phonon motion causing reduction in the thermal diffusivity.

5.2 Studies on TiO_2-CeO_2 Nanocomposites

5.2.1 Introduction

Since 1970s extensive research has identified TiO_2 as a treasured material, because of its unique properties such as biocompatibility, low cost and ease of availability[12]. Due to its high band gap it can absorb only UV light making it difficult to harness its properties in the visible range[13,14,15]. Functionality in the visible range is achieved by doping TiO_2 with cations, anions or by coupling it with various other materials with lower band gap[16,17,18,19]. Studies have been conducted by doping TiO_2 with various rare earth elements[20]. Among them, Ce has shown promising results[21]. It has properties similar to that of TiO_2, such as nontoxicity, high stability etc[22,23]. It is reported that a well-coupled CeO_2–TiO_2 composite could produce a special electron transfer process, which could facilitate the separation of the electron–hole pairs[24]. CeO_2 has incompletely filled 4f orbital and empty 5d orbital[25]. Out of all the lanthanide elements, cerium has drawn the major attention because of the availability of Ce^{3+} / Ce^{4+} redox couple and display of different optical properties due to electronic alignment of Ce^{3+} with $4f^1 5d^0$ and Ce^{4+} with $4f^0 5d^0$ [21,24,26]. Medical diagnostics, optical storage, optoelectronic devices and displays are some of the examples which utilise the properties of such materials[27].

5.2.2 Experimental

TiO_2-CeO_2 nanocomposites were prepared by the sol-gel method. Here, cerium chloride $CeCl_3.7H_2O$ and titanium tetrabutoxide (TTBO) [$Ti(OC_4H_9)_4$] were used as the precursors for CeO_2 and TiO_2 respectively. $CeCl_3.7H_2O$ was dissolved in adequate amount of ethanol and TTBO was added drop wise followed by annealing at 500ºC. The procedure followed for the preparations of the samples were demonstrated in literature[28]. Various percentage compositions of the samples have been prepared.

Characterization techniques involved the recording of absorption and transmittance spectra using a spectrophotometer. The fluorescence was measured with a flourimeter. The nonlinear optical characterization was carried out using Z-scan experiment.

5.2.3 Results and Discussions

i. XRD Pattern

Figure 5.13 represents the XRD pattern of the nanocomposites samples. It is observed that as the CeO_2 amount increases there is reduction in diffraction peak intensity and increase in full width at half maximum (FWHM). This indicates that the crystallinity of the TiO_2 anatase phase deteriorates and the crystallite size of the TiO_2 anatase becomes smaller with the increase in CeO_2 amount. The crystallite size was measured using Scherrer equation and was found to be 10.7 nm, 11.3 nm and 13.4 nm for 75C-25T, 50C-50T and 25C-75T respectively. Ce $^{3+}$ has a larger size (115 pm) than that of Ti $^{4+}$ (75 pm), and hence it is difficult for the Ce^{3+} ion to penetrate the TiO_2 surface substituting Ti^{4+} inside lattice. In that case few Ce $^{3+}$ ion penetrate into the lattice and the rest sit on the grain boundary or on the nanocrystallites, distorting the crystal structure of TiO_2. Due to such charge difference between $Ti^{4+}$and Ce $^{3+}$, cerium also generates oxygen vacancies to maintain charge balance.

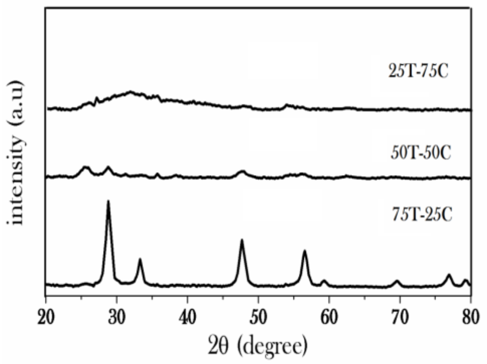

Figure 5.13 : *XRD pattern of the nanocomposites samples.*

ii. FTIR Studies

Figure 5.14a shows the FTIR spectra of the nanocomposites. Peak at 1625 cm^{-1} is due to the H-O-H bending vibration of physisorbed water. Figure 5.14b shows the enlarged view of the graph from 500 cm^{-1} to 400 cm^{-1}.The peak at 469 cm^{-1} for C25-T75 indicating the Ti–O–Ce bond gets shifted towards lower wavenumber region as the amount of CeO_2 increases in the nanocomposites.

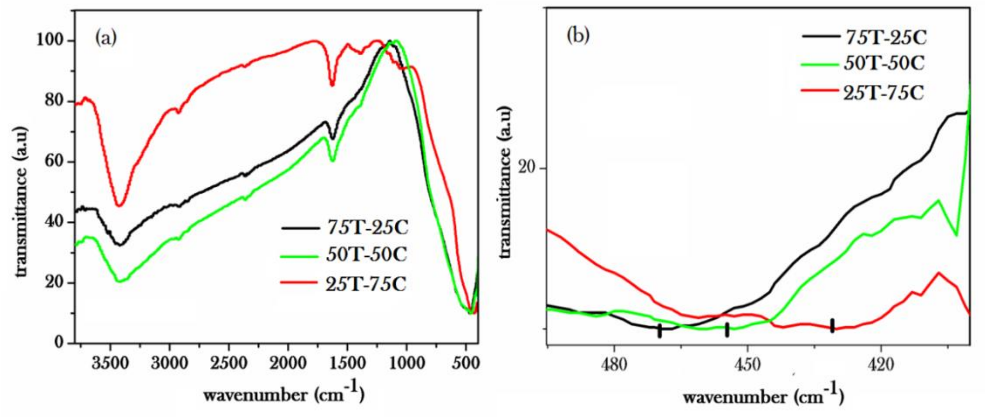

Figure 5.14: *(a) FTIR spectra of the nanocomposites (b) Enlarged view of the spectra within the 400-500nm range ; the black line shows the absorption band for Ti–O–Ce bond.*

iii. Absorption Spectroscopy

Figure 5.15 depicts the absorption spectra of the as prepared nanocomposites using a spectrophotometer (JascoV-570 UV/VIS/IR). Absorption spectroscopy helps in understanding the electronic transition of a particular valence state. From the figure it is seen that there is a broad absorption band located in the UV range and this can be due to the fact that Ce^{4+} substitutes Ti^{4+} in TiO_2 which then under the ligand field environment of O^{2-} of TiO_2, splits and forms Ce^{3+} and shows 4f-5d transition. Ce^{3+} has single optically active electron with the ground state configuration as $4f^15d^0$ [29,30].

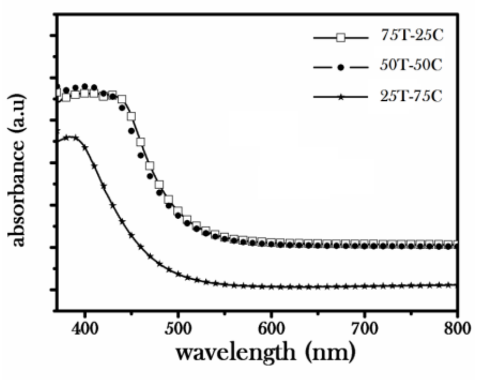

Figure 5.15: *Absorption spectra of the nanocomposites*

Figure 5.16 represents the band gap estimation of the nanocomposites. The direct band gap was determined from the graph of hυ vs $(\alpha h\upsilon)^2$ for the absorption coefficient α which is related to the band gap Eg as

$$(\alpha h\upsilon)^2 = \text{const}\,(h\upsilon - E_g) \tag{5.2}$$

where hυ is the incident light energy.

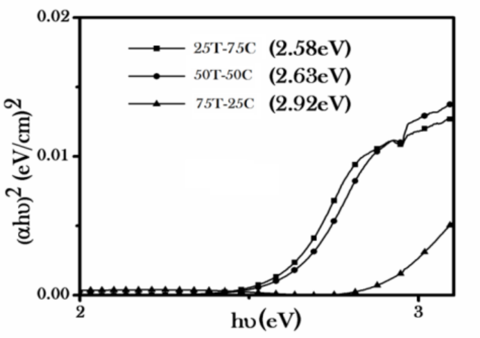

Figure 5.16: *Band gap estimation of the nanocomposites using Tauc's plot.*

It has been observed that as the CeO_2 amount increases, the band gap decreases. The narrowing of band gap can be due to the fact that presence of Cerium 4f level and oxygen defects present below the conduction band (CB) edge undergo hybridization to produce an impurity band as represented by a step shaped peak at around 380 nm in the absorption spectra of the nanocomposites. The localized band states produced by these 4f electrons and oxygen defect levels allow maximum electronic transitions to occur only to these levels [31] [32]. The localised states of CeO_2 smudges out to the forbidden energy gap of TiO_2 leading to the formation of Urbach tail. The energy associated with it is known as Urbach energy which can be calculated from the expression,$\alpha=\alpha_0 \exp(E/E_u)$ where E_u denotes Urbach energy. Table 5.4 gives the respective value of E_u. Due to the presence of dopant impurities, oxygen defects, and thermal disorders broadening of the Urbach tail can occur[33] [34]. It has been observed that E_u increases as band gap decreases. This increase in Urbach energy with the decrease in band gap indicates the presence of a large number of defects and Ce 4f related band states, below CB edge, producing localized electronic states which capture the electrons on irradiation[35].

Composition	Eg (eV)	Eu (eV)
T25-C75	2.58	0.2805
T50-C50	2.63	0.2346
T75-C25	2.92	0.1912

Table 5.4*:* *Values of band gap and Urbach energies.*

iv. Photoluminescence Studies

Figure 5.17 shows the photoluminescence spectra of the different compositions at an excitation wavelength of 240 nm. On excitation, strong green light is observed from the composite. This occurs due to the d electrons of Ce coupling differently to the lattice phonon in the cubic fluorite structure, leading to a higher Stokes shift. Emission at around 390 nm is due to interband transition in TiO_2. Presence of Cerium oxide reduces the interband transition in TiO_2 and hence decreases the corresponding fluorescence emission[36,37] . The peaks between 470 nm -580 nm are defects emission bands which increase non uniformly. Defects like anion and cation vacancies also decrease with CeO_2 concentration. The cations Ce^{3+} occupy the Ti^{4+} vacancy sites thereby reducing the number density of Ti^{4+} vacancies. As a result of charge compensation, presence of Ce^{3+} will result in the formation of O^{2-} at interstitial sites. Hence it can be confirmed that fluorescence in the visible band is due to its optical interaction with lattice defects like anion vacancies.

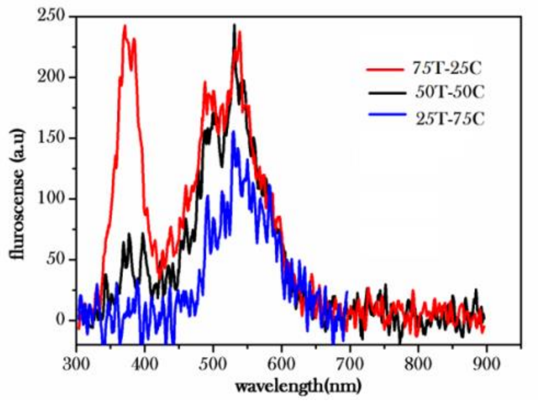

Figure 5.17: *Photoluminescence spectra with excitation wavelength at 240 nm.*

When the CeO_2 concentration is less it acts as a radiative recombination centre, increasing the charge carrier recombination. But as it increases, energy gets transferred among the neighbouring Ce^{3+} ions and hence intensity decreases.

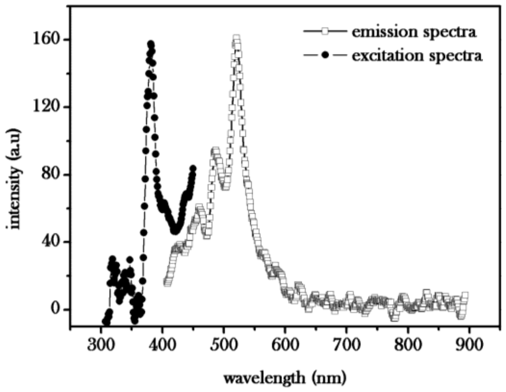

Figure 5.18: *Excitation and emission spectra of 25%TiO_2-75% CeO_2.*

Figure 5.18 shows the excitation and emission spectra of the 25T-75C. There is an excitation peak at around 380 nm and emission at around 521 nm. The occurrence of fluorescence emission along with a broad absorption peak at 380 nm in the absorption spectra confirms the argument of presence of localised defect states in the forbidden energy gap of the nanocomposites.

Figure 5.19 shows the photoluminescence spectra of 75T-25C with different molar concentration. It is found that with the increase in concentration, fluorescence quenching occurs. This happens because at high concentration the spatial distribution of the dopant is such that the energy gets dispersed among the Ce^{3+} ions. These act as recombination centres and energy ceases to come out as luminescence. Thus the role of Ce^{3+} ions as radiative or non-radiative centres depends on the position and distribution of dopants in TiO_2 lattice. As reported by Chen et al there occurs a red shift in photoluminescence peak due to band tailing effect as the Cerium 4f level and oxygen defects present below the CB edge undergo hybridization to produce an impurity band that produces band tailing[38]

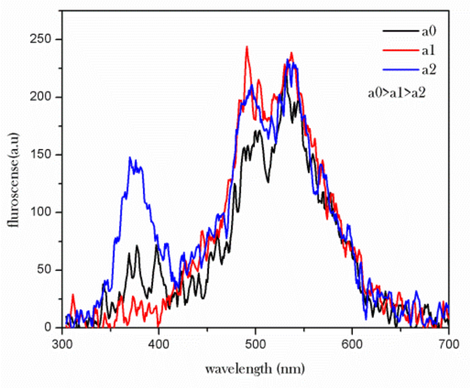

Figure 5.19: *PL spectra of 75T-25C where a_0 has the highest molar concentration.*

v. Nonlinear Optical Studies

In order to investigate nonlinear property of the prepared nanocomposites, Z-scan technique was employed. Figure 5.20 shows the open aperture Z-scan curve of the nanocomposite employing 532 nm at 326 MW/cm^2. It is observed that the graph so obtained follows RSA. Generally RSA can occur due to two-photon absorption or due to free carrier absorption.

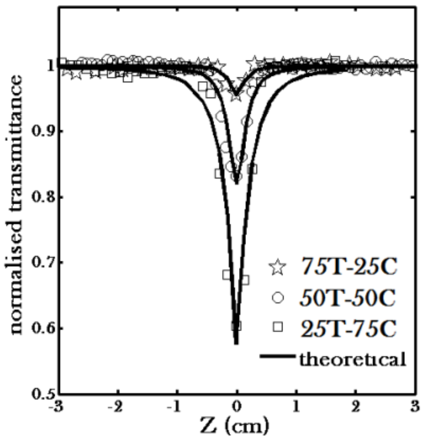

Figure 5.20: *Open aperture Z-scan of different nanocomposites composition at 326 W/cm^2. Solid line represents the theoretical curve.*

Two photon absorption (TPA) is one of the most important nonlinear processes in semiconductors and here TPA dominates as it satisfies the relation $Eg/2 < h\upsilon < Eg$. It is predicted that, electrons in the valence band can make transitions to the conduction band only through an intermediate state[39]. This result agrees very well with the TPA process as reported in bulk TiO_2 samples[40 ,41]. As evident from the PL peak, Ce^{3+} 4f level and oxygen defects present below the CB edge undergo hybridization to produce an impurity band and it is proposed that this level acts as the intermediate level enabling the two photon absorption to occur. This intermediate level has been pictorially represented in figure 5.21.

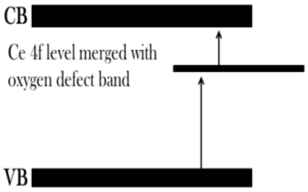

Figure 5.21: *Energy band diagram of TiO_2:CeO_2.*

It has also been observed that as the CeO_2 amount in the sample increases, non-linearity increases indicated by the dip in the curve. Here, intersubstituting of TiO_2 and CeO_2 occurs in each other's crystal lattice at the interface of two types of metal oxides, thus creating a charge imbalance. In order to balance the charges more hydroxide ions would be adsorbed on the TiO_2 surface, acting as hole traps that prevent electron-hole recombination and thus giving rise to higher non linearity. This means that Ce^{3+} modifies the local symmetry of TiO_2 thereby enhancing optical non linearity. Figure 5.22 shows the open aperture curve of the 50T-50C nanocomposites at various powers. Here it is observed that as the power increases the dip also increases but the calculated nonlinearity value decreases. This is due to the removal of appreciable amount of photo carriers from the ground state. Thus when the irradiated intensity increases the β value decreases. As per the expectations[42] table 5.5 shows the various values of β, Eg,, Im {χ^3}. In this report our values vary as per the prediction.

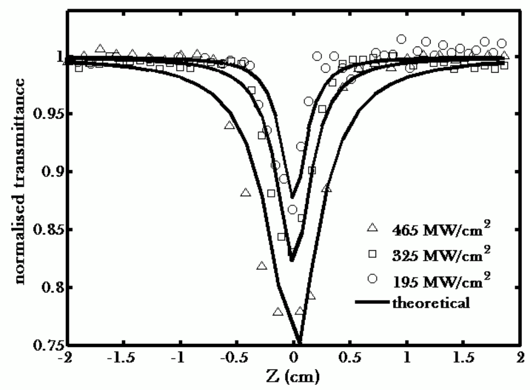

Figure 5.22: *Open aperture Z-scan at different powers (in MW/cm^2). Solid line represents the theoretical curve.*

Composition	Eg(eV)	Im {χ} at various powers × $10^{-19}m^2V^{-2}$				Optical limiting threshold at 196 MW/cm^2
		196 MW/cm^2	326 MW/cm^2	388 MW/cm^2	464 MW/cm^2	
T25-C75	2.58	6.56	5.37	4.40	3.54	136
T50-C50	2.63	4.97	3.26	3.03	2.27	166
T75-C25	2.92	2.75	2.78	2.63	1.58	183

Table 5.5: *Measured values of optical band gap and imaginary part of the third-order susceptibility (Imχ^3) at a wavelength of 532 nm for different irradiation intensities & optical limiting threshold.*

Figure 5.23 shows the closed aperture Z-scan curves of the nanoparticle with composition T75-C25 at the above mentioned wavelength of 532 nm at different laser intensities. Initially the closed aperture exhibited a peak to valley shape, depicting negative value of nonlinear refractive index n_2. In order to obtain the phase distortion caused due to the change in refractive index, normalised closed aperture data was divided by the corresponding normalised open aperture data. It is observed that peak-valley of closed aperture Z-scan satisfied the condition Δz~1.7z0 thus confirming the presence of cubic non linearity. The ΔT_{p-v} difference between peak and valley is obtained from the theoretical curve.

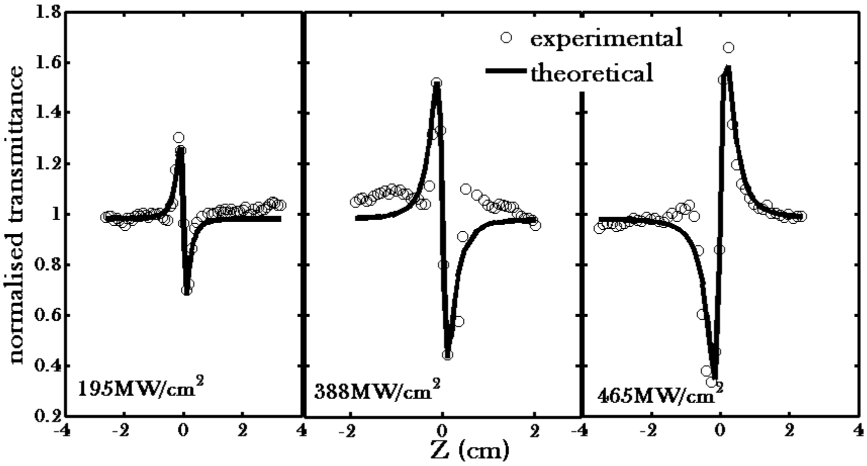

Figure 5.23: *Closed Aperture Z-scan results of T75-C25 at different exciting laser intensities. The solid curves show the theoretical fitting.*

The peak–valley trace in closed aperture Z-scan shows that these samples show switching between self-focussing ($n_2>0$) and self-defocusing ($n_2<0$) nonlinearity. From the model suggested by Sheik-Bahae et.al, the sign of nonlinear refraction is positive when the photon energy is smaller than 0.7 Eg where Eg is the band gap of the material. The n_2 becomes negative when the photon energy is in the range from 0.7Eg –Eg. In our case photon energy is 2.336eV which in all cases fall within the range 0.7Eg-Eg. But our results deviate from the proposed model. We suggest that this could be due to the fact that as the power is increased the concentration of excited electrons increases which in turn increases the nonlinear refraction resulting in self-focussing. Similar switching behaviour was obtained for other compositions also. It has been observed that as the amount of CeO_2 increases in the nanocomposites, switching from negative to positive nonlinear refraction occurs at much higher laser powers. This intensity-dependent nonlinear refraction described here is expected to have potential applications in optical information processing.

Figure 5.24 shows the closed aperture Z-scan curve of the nano composite of varied composition at the same power density (465 MW/cm^2). The corresponding values of n_2 are shown in table 5.6. It is observed that as the amount of TiO_2 increases in the composition nonlinear refraction increases. This can be credited to the fact that as the amount of CeO_2 increases RSA increases due to enhanced two photon absorption thereby reducing the possibility of positive nonlinear refraction[43] .Thus by varying the amount of CeO_2 in the nanocomposite switching phenomenon is conceivable, which has potential applications in the field of photonics technology.

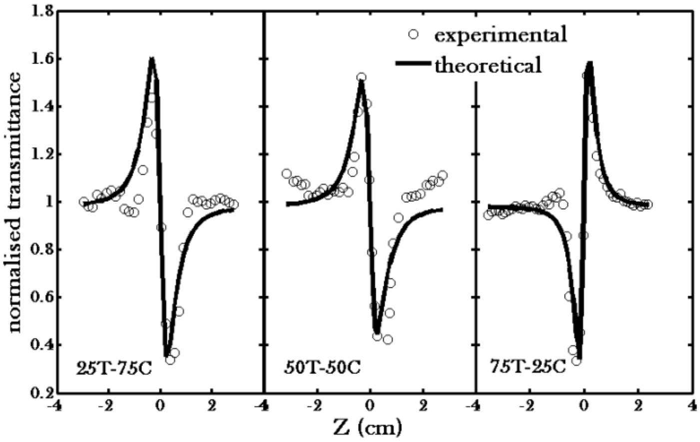

Figure 5.24: *Closed Aperture Z-scan results for different composition at 465 MW/cm^2. The solid curves show the theoretical fitting.*

vi. Optical Limiting Studies

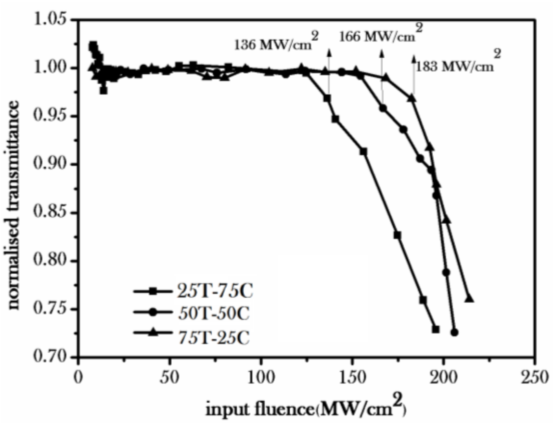

Figure 5.25: *Optical limiting response of the nanocomposites at 196MW/cm^2.*

One of the important applications of reverse saturable absorption is fabrication of devices based on optical limiters[41]. These devices transmit light at low input power densities but restrict them by becoming opaque at higher input fluences. They can be used for protection against intense light energy as well as highly sensitive detectors. Their optical limiting phenomenon can be analysed by estimating the imaginary part of susceptibility, which can be obtained from Z-scan measurements. Such a study has been presented here in figure 5.25. In the graph optical limiting ability of different composites has been plotted at 532 nm irradiated with an input fluence of 196MW/cm^2. The arrow indicates the limiting threshold of the composites. It is taken as the point at which the curve starts deviating from linearity. It has been found that as the dopant (CeO_2) concentration increases the composite performs better as an optical limiter by decreasing the optical limiting threshold. It is proposed that this can be due to the grain size variation caused by the presence of Ce^{3+} on the grain boundary.

Composition of T-C	$\beta\times10^{-10}$ (m/W)	$n_2 \times10^{-17}$ (m^2/W)	$Im\{\chi\} \times10^{-16}$ (m^2/V^2)	$R\{\chi\}\times10^{-18}$ (m^2/V^2)
T25-C75	5.18	-6.14	5.37	-1.36
T25-C75	2.65	-5.64	3.26	-1.46
T25-C75	1.64	7.44	2.78	1.66

Table 5.6: *Various nonlinear parameters of the TiO_2-CeO_2 nanocomposites at 465 MW/cm^2.*

vii. Thermal Diffusion Studies

Thermal diffusivity determines the thermal transport properties of materials. This method is mostly preferred due to its insensitivity to radiation loss. Dual beam mode matched thermal lens technique is employed to study the heat diffusivity of the TiO_2-CeO_2 nanocomposites. The time evolution of thermal lens signal for the composites is shown in the figure 5.26. The solid curve represents the theoretical fitting while the circles represent the experimental data. Table 5.7 gives the numerical values of thermal diffusivity obtained from the experiment.

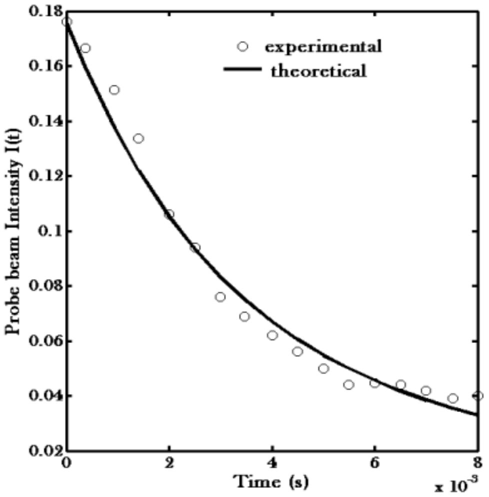

Figure 5.26: *Decay curve of intensity probe beam for TiO_2–CeO_2 nanocomposites: amorphous 50T-50C in thermal lens experiment.*

Samples	Thermal diffusivity T_D (mm^2/s)
25T-75C	0.020
50T-50C	0.382
75T-25C	0.433

Table 5.7: *Measured values of thermal diffusivity for the amorphous 50T-50C.*

It is observed that as the concentration of CeO_2 increases thermal diffusivity decreases. As observed from the previous studies, as the CeO_2 amount increases in the nanocomposites density of localised defect states within the forbidden gap also increases which offers enhanced resistance to propagating thermal waves due to increased scattering .This causes decrease in thermal diffusivity.

5.3 Studies on TiN

5.3.1 Introduction

In the past decades, great progress has been made in nanomaterials for nonlinear optics. Materials with large nonlinear susceptibilities and fast response time are widely reconnoitred for their potential application in the field of photonic devices. In particular, metal nanoparticles signified by surface plasmon resonance (SPR) are of considerable importance due to the enhanced optical nonlinear processes within their SPR region[44]. It is the coherent oscillation of free electrons, occupying states near the Fermi level in the conduction band, that gives rise to a surface plasmon absorption band for which peak and width depends on the size and shape of the nanoparticles. SPR leads to an increase in the electric field inside the particle, and the local field gives rise to enhancement of the third order optical non linearity. The most significant advances towards understanding the NLO properties of metal nanostructured materials have been through nonlinear transmission measurements[45] . Besides the application of noble metals in the field of plasmonics, few other materials are also well acclaimed for showing such marvellous SPR property, for example nanospheres of lithium, potassium and sodium etc[46,47]. Recent studies have proved that TiN can also be considered as a possible material for plasmonic devices[48,49]. Unlike conventional plasmonic materials like Gold and Silver, TiN is much more robust to the losses at optical frequencies. The merits of TiN as a plasmonic material have been reported by

Cortie et. al.[49]. The most expedient thing about the TiN as plasmonic material is that the optical properties can be tuned, unlike in the case of noble metals, simply by changing the processing conditions[50].

In the present section the nonlinear optical property of TiN using Z-scan experiment is discussed. We observed reverse saturable absorption (RSA) in the open aperture and interesting phenomenon of switching in the sign of nonlinear refractive index in the case of closed aperture Z-scan experiment with TiN nanoparticles at 532 nm. The present measurement of the real part ($\mathrm{Re}\{\chi\}$) and imaginary part ($\mathrm{Im}\{\chi\}$) of the third order susceptibility of TiN nanoparticles using Z-scan experiment reveals its potential application in the field of optoelectronic devices. In order to evaluate the suitability of the nanoparticle for all optical switching application figure of merit, namely two-photon figure of merit (FOM), $T=\beta\lambda/n_2$ was also evaluated[51].

5.3.2 Experimental

During the experiment TiN powder of average size 55 nm (purchased from Plasma Chem, Berlin) were used without any further processing. Experimental procedures involved recording the absorption and transmittance spectra of the nanoparticle suspended in de-ionized water by using a spectrophotometer (JascoV-570 UV/VIS/IR). The nonlinear optical characterization was carried out using Z-scan experiment. The sample (TiN suspended in de-ionized water) to be investigated were mounted on a translation stage controlled by a computer and was moved along the Z-axis through the focal point of a lens of focal length 20 cm.

5.3.3 Results and Discussions

i. Absorption Spectroscopy and Structural Characterization

The absorption spectrum of TiN nanoparticles suspended in de-ionized water was measured in the UV–visible region and are illustrated in figure 5.27.

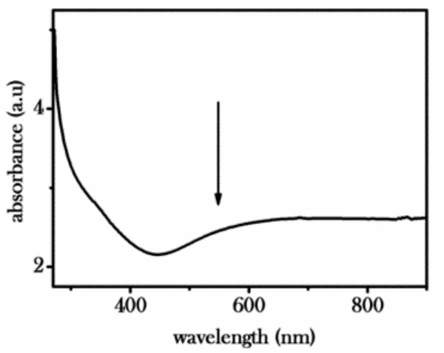

Figure 5.27: *Absorption spectra of Titanium nitride nanoparticles.*

TiN is comparatively absorptive at wavelengths <400 nm, apparently, due to interband transitions[52]. The graph shows the absorbance of the sample with an unusual step function at around 550 nm and this can be due to the surface plasmon resonance as reported[53] . These bands exhibit broad FWHM with their tails extending into the IR region. It is proposed that the interaction between the particles constituting the aggregate clusters with irregular sizes and shapes caused the excessive broadening of their SPR band. The presence of irregular shaped particles are clearly evident from the high resolution transmission electron microscopy (HRTEM) and Scanning electron microscopy (SEM) as shown in Figure 5.28. The distance between the between nanoparticles, either as discrete particles or as aggregates of varying size, has significant influence on the absorbance spectra. The oscillating electron in one particle feels the electric field due to the oscillations in a second particle, which can lead to a collective plasmon oscillation of the aggregated system. This leads to higher energy plasmon modes being excited by light at closer separations. Thus, the plasmons of a complex nanoparticle result from hybridization of the plasmons of individual nanoparticles, and the strength of the hybridization depends on the geometry of the composite particle[54,55].

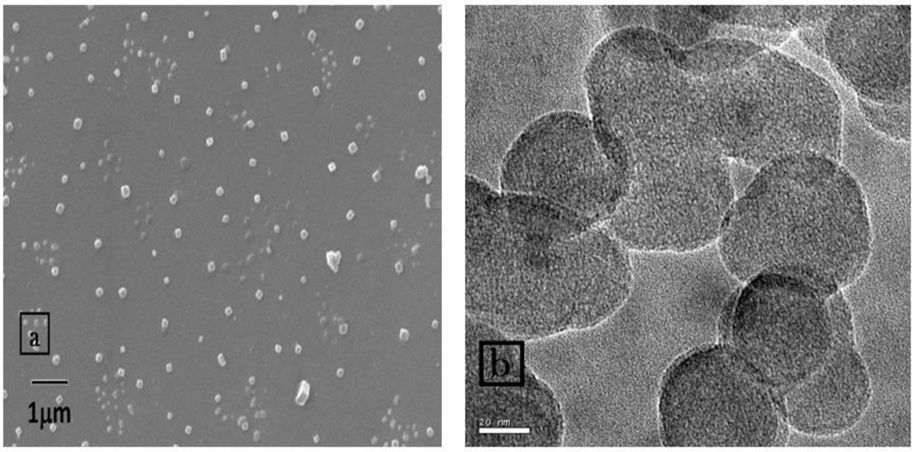

Figure 5.28: *(a) SEM images of the nanoparticle. Figure shows that there are particles of various size and shape. (b) TEM images of TiN nanoparticles.*

Figure 5.29 represents the band gap calculation of the TiN nanoparticle as per Tauc's plot. The optical absorption edge was analysed with Tauc equation[56] ,

$$\alpha h\upsilon = A(h\upsilon - Eg)^{0.5} \tag{5.3}$$

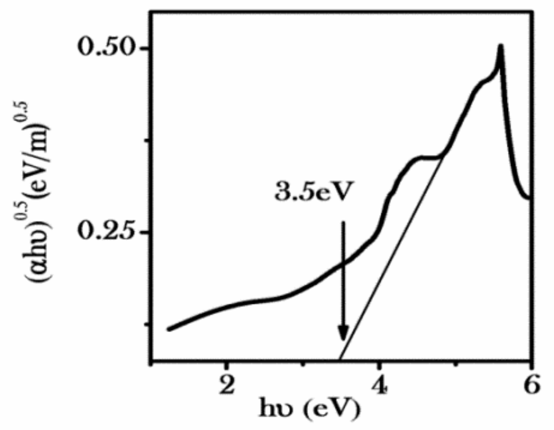

Figure 5.29: *Optical Bandgap estimation of TiN using Tauc's plot.*

ii. XRD Pattern

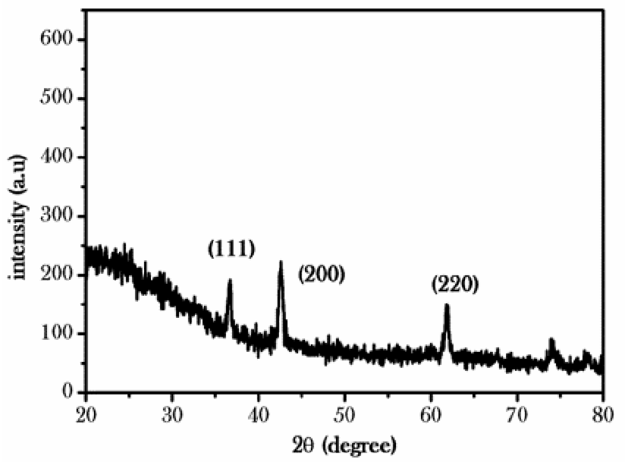

Figure 5.30: *XRD pattern of TiN samples.*

Figure 5.30 shows the XRD pattern of TiN samples. The graph shows the nanoparticles are crystalline in nature. Peaks at 2Θ of 36° and 62° are characteristic peaks of TiN. The samples can be indexed as a face-centred cubic structure.

iii. Nonlinear Studies

Figure 5.31 shows the absorptive nonlinearity observed at 532 nm at four different laser intensities, 217, 290, 363, 508 MW/cm^2 respectively. Nonlinear absorption curves are indicated by a smooth valley-shaped curve, symmetric about the focal position.

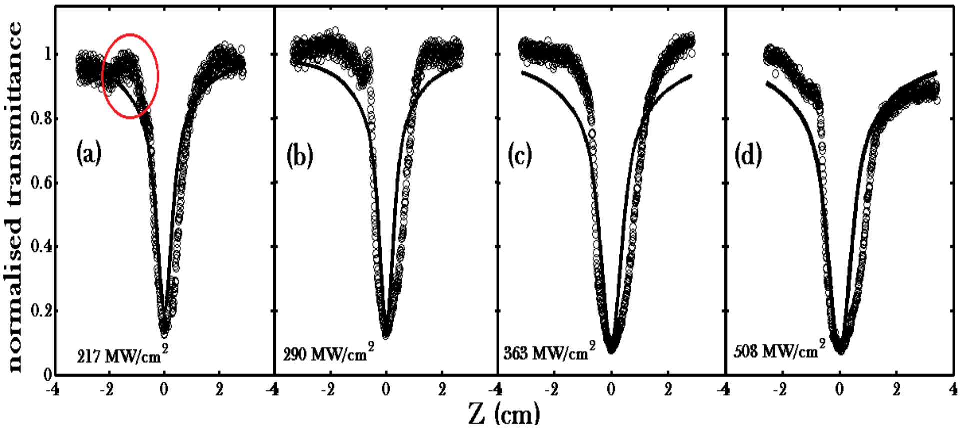

Figure 5.31: *Open aperture Z-scan curve of TiN nanoparticle at various powers. Solid curve indicates the theoretical simulation. The encircled portion portrays the "hump" resulting from the ground state bleaching.*

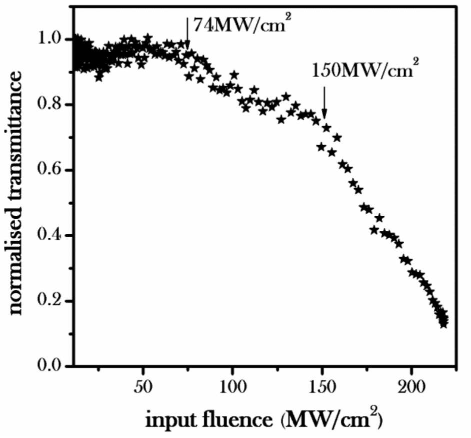

Figure 5.32: *Optical limiting threshold of the sample at 219 MW/cm^2.*

Figure 5.32 corresponds to the optical limiting curve of the TiN samples at 217 MW/cm^2; the arrow indicates the limiting threshold. Optical limiters are those materials for which transmittance falls down with an increase in the incident laser fluence after a threshold value of the incident fluence, which is due to several phenomena such as free-carrier absorption, two-photon absorption, three-photon absorption, and nonlinear scattering. Here, the figure shows an additional slope change at 150 MW/cm^2 apart from that at 74 MW/cm^2. This implies that the material work as an optical limiter at low fluence of 74 MW/cm^2. However more efficient optical limiting will be shown at 150 MW/cm^2. Optical limiting threshold is taken as the point at which the curve starts deviating from linearity. They are of special concern in nonlinear optics and optoelectronics for their possible application for the protection of eyes and sensitive detectors against intense radiation. In Titanium Nitride the optical properties are due to Ti 3d and conduction electrons constituting the N2s and N2p electrons. Similar to noble metals the band gap analysis of TiN the outermost d and s electrons of the constituent atoms must be treated as six bands. Five of them are fairly flat and lie a few electron volts below the Fermi level; they are usually denoted as d bands. The last sixth one being an almost free electron is roughly parabolic, with an effective mass close to that of a free electron. This last band is called s–p band or conduction band. Hence we can conclude that the conduction electrons as well as d electrons through TPA contribute to the nonlinear response near SPR. Experimental data fitted well with the theory of two-photon absorption which further strengthens the assumption.

Interestingly, in the open aperture Z-scans obtained from the present samples we observed unusual ‘‘humps’’ flanking the valley and it is believed that they arise from the bleaching of the ground-state plasmon band prior to free-carrier absorption as reported[57]. When the sample is far away from the focal point, the pump intensity is too weak to induce any nonlinearity and the transmittance is almost equal to unity. As the sample is moved further towards the focus, the intensity increases so that ground-state plasmon bleaching resulting in saturable absorption (SA) hence more light is transmitted and the transmittance becomes higher than unity. At higher pump intensities encountered by the sample as it nears the focal point, free carrier absorption dominates in this region resulting in reverse saturable absorption (RSA) causing limiting. Consequently less light is transmitted and the transmittance falls drastically to values less than unity. Hence the increase in transmittance from unity followed by a decrease will produce a local ‘‘hump’’ in the curve. In particular, it is realized that similar to metal nanoclusters TiN belongs to a group of materials where SA and RSA happen at the same pump wavelength for different pump intensities.

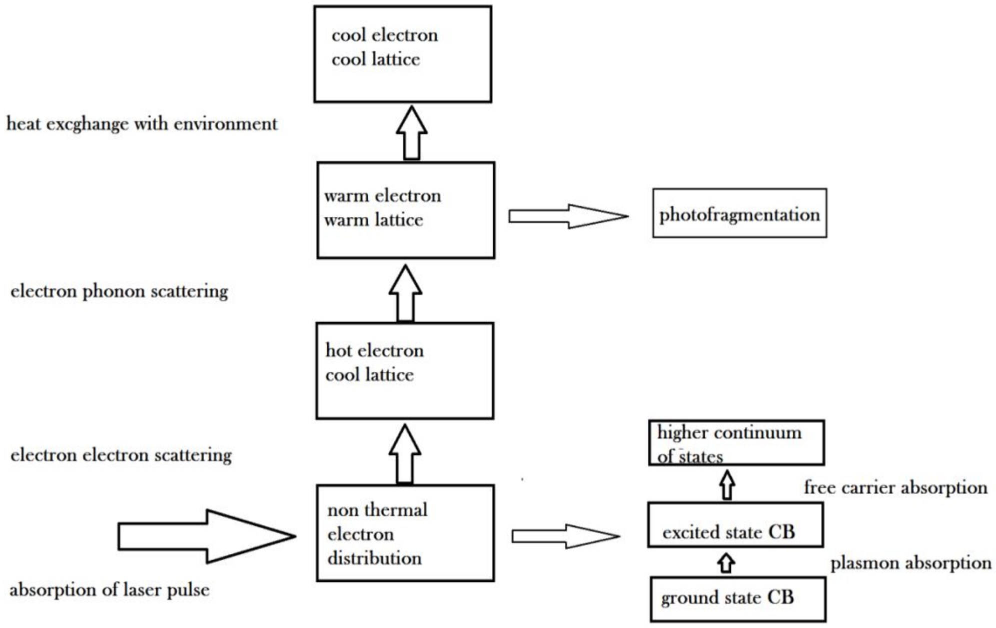

Figure 5.33: *Proposed internal dynamics in TiN nanoparticles on laser irradiation.*

In the present case, following electron dynamics as represented in figure 5.33 can be considered. Nanosecond excitation of the sample leads to intraband electron excitation within the conduction band. This is accompanied by broadband transient absorption by the free carriers within the conduction band, leading to ground-state plasmon bleach. In general, a laser pulse can cause an interband or intraband electron transition in the nanoparticle system, depending on the excitation wavelength and intensity. The electrons thus excited are free carriers possessing high energies, and hence are called hot electrons. The hot electrons get thermalized by dissipating excess energy through successive processes of electron–surface scattering, electron electron scattering and electron–phonon scattering[58,59]. During the process full recovery of plasmon bleach is delayed and transient absorption is observed till thermalization of hot electrons is complete. The component of transient absorption taking place in nanosecond timescale is mainly due to photochemical change induced absorption arising from photo-ejection of electrons from the sample on laser irradiation. Photo-ejection of electrons is a multi-photon process. The ejected electrons can charge the nanoparticle surface electrically, this in turn causes them to disintegrate and form smaller size particles, which results in a transient state generated by photo induced intraparticle charge separation. Hence in the present case the possibility of photoejection of electrons can also be considered as a contributing factor leading to optical limiting[60] .

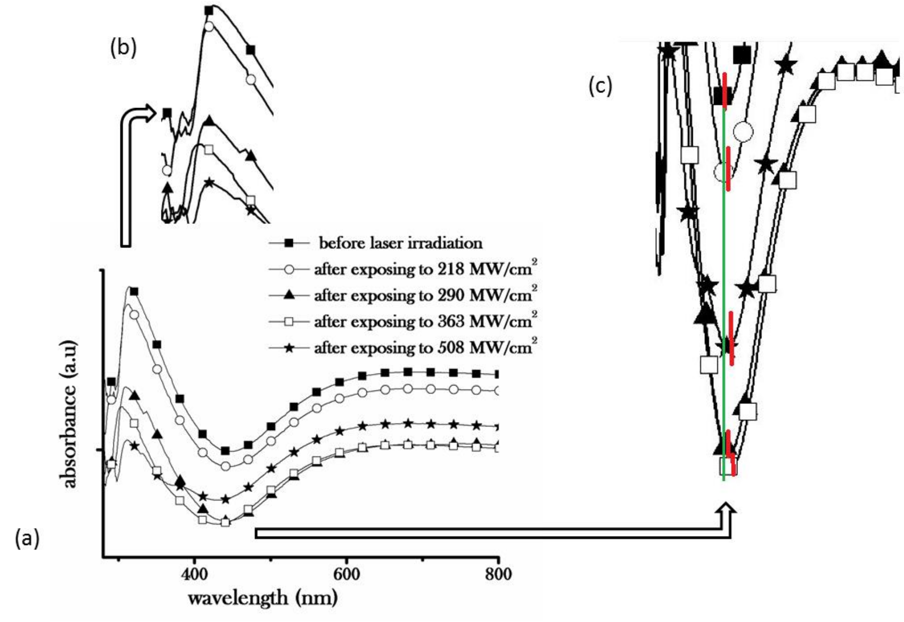

Figure 5.34: *(a) Post excitation absorption spectra of the nanocomposites.(b) enlarged view of the peak region depicting increase in the band gap.(c) enlarged view of the valley region to determine the shift in SPR (as the region around SPR at 550 nm is having large FWHM, shift is difficult to determine and for better clarity valley region has been enlarged). The shift is relatively small as the exposure to the laser during the experiment lasted only few seconds.*

Here, confirmation to such photofragmentation of clusters has been obtained from post-excitation absorption spectra as shown in figure 5.34. It has been observed that after irradiating the sample at the respective powers there occurs a blue shift in the absorption spectra indicating a decrease in the particle size with a corresponding increase in the band gap. To further confirm the argument TEM analysis was performed after the entire experiment. TEM analysis given in figure 5.35 shows that the average particle size was reduced from 55nm (figure 5.28 b) at the beginning to 46 nm at the end of the experiment.

In the figure 5.34 it is observed that at 363 MW/cm^2 and 508 MW/cm^2 there occur a cross-over in their SPR region leading to red shift .We believe that the reason for this could be due to the increased interparticle interaction thereby modifying the resonant condition[61]. At 363 MW/cm^2 the laser intensity becomes very high and it produces large number of irregular disintegrated nanoparticles. But due to surface plasmon excitation, charge accumulates in the vicinity of nanoparticles. Interparticle interaction comes into play when the head to tail interaction of induced dipoles in photo-fragmented constituents becomes highly energetic and there are chances that they get arranged in specific compact geometric patterns leading to enhanced interparticle interaction as illustrated in figure 5.36. When NPs are arranged in particular geometries it is possible to create controlled interferences that allow additional tuning of the surface plasmon excitation band.

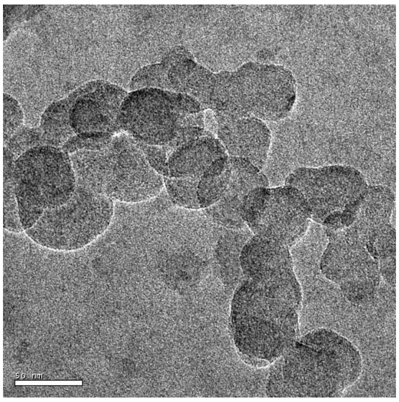

Figure 5.35: *TEM image of the nanoparticle at the end of the experiment.*

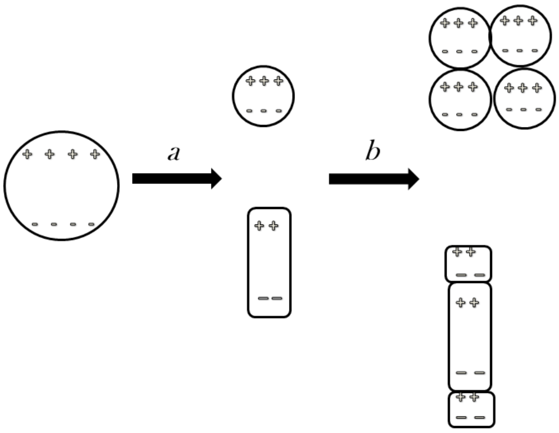

Figure 5.36: *Illustration of inter particle interaction between the particles leading to the arrangement of the particles in specific compact geometric patterns.(a) the phenomenon of photofragmentation (b) interparticle interaction.*

Figure 5.37 shows the closed aperture Z-scan curve of the nanoparticle at different laser intensities as mentioned in the figure at wavelength of 532 nm .The closed aperture scan exhibited a peak to valley shape ,depicting negative value of nonlinear refractive index n_2. In order to obtain the phase distortion caused due to the change in refractive index, normalised closed aperture data was divided by the corresponding normalised open aperture data. It is observed that peak –valley of closed aperture Z-scan satisfied the condition $\Delta z \sim 1.7 z_0$ thereby confirming the presence of cubic non linearity[62]. This is a direct consequence of the electron-phonon relaxation in the medium, which is a nonradiative process. During electron-phonon interactions, thermalization occurs when electrons lose their energy by externally thermalizing with the lattice. As a result of electron phonon interaction the immediate vicinity of the irradiated volume is heated up leading to a reduction in the local refractive index, resulting in the self-defocusing of the beam. The vibrational frequency of the electron phonon coupling vibrational modes has been found to be inversely proportional to the radius of the nanoparticles, and the frequency can be calculated quite accurately on the basis of classical mechanics. The electron phonon interaction is subsequently followed by phonon phonon interaction. During this process, excess thermal energy will be dumped into the solvent .In the present case as mentioned high laser intensities ie, 363MW/cm^2 and 508 MW/cm^2 lead to the formation of large number of small disintegrated nanoparticles for which surface to volume ratio is very large when compared to that of the nanoparticles before the laser irradiation, as a result the probability of phonon phonon interaction would be more than the electron phonon interaction. Larger the surface to volume ratio the faster will be the heat dissipation to the solvent. Hence, with decrease in the nanoparticle dimension, thermal non linearity diminishes with the onset of electronic non linearity.

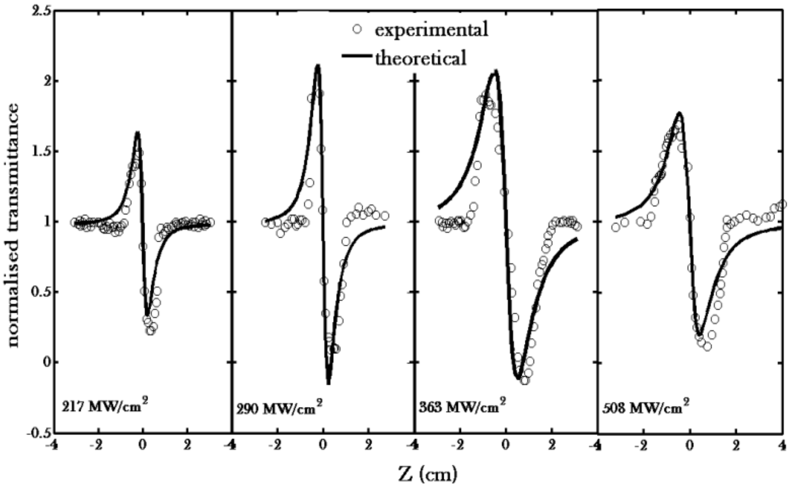

Figure 5.37: *Closed Aperture Z-scan curve of TiN nanoparticle at various powers.*

To evaluate the performance of the nanoparticles for all-optical switching devices, the figures of merit T, defined by $T=n_2/2\beta\lambda$ were calculated [63].It was found that the values of T of the obtained nanoparticles meet the requirement of T<1 for all-optical switching device applications.

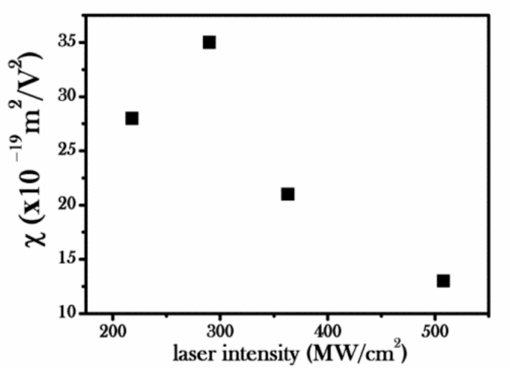

Figure 5.38: *Dispersion in third-order optical nonlinear susceptibility* $\chi^{(3)}$ *measured at a laser wavelength of 532 nm for various power densities.*

In table 5.8 it is seen that $\chi^{(3)}$ being an intrinsic constant for the TiN sample, varies with laser intensities. Figure 5.38 shows the dispersion of nonlinear susceptibility of the particle with varying intensity. It is well established that the enhancement of $\chi^{(3)}$ in the metal/dielectric composite strongly depends on the non-linearity of the metal particle itself and on the so-called local field factor $f = 3\varepsilon_d/(\varepsilon_m+ 2)$ where ε_m and ε_d are the dielectric constant of the metal and the dielectric matrix, respectively. Near resonance, the local field factor can be written as $f = 3\varepsilon_d/(i\varepsilon_{m2})$ where ε_{m2} is the is the imaginary part of the metal dielectric constant, which increases with decreasing particle size. So, smaller the particle size, smaller the local field factor, and smaller the value of $\chi^{(3)}$. Hence because of these aspects there arises the dependence of $\chi^{(3)}$ on the size and hence in the present case on the irradiated laser intensities as there occurs causes photo fragmentation with increasing laser intensity.

I/p Laser intensity (MW/cm^2)	ß ×10^{-10} (m/W)	n_2 ×10^{-16} (m^2/W)	Im{χ} ×10^{-19} (m^2/V^2)	R{χ} ×10^{-19} (m^2/V^2)	χ×10^{-19} (m^2/V^2)	Figure of merit T
218	8.308	-1.335	7.046	-2.675	27.67	0.15
290	6.338	-1.712	5.378	-3.43	34.70	0.25
363	5.08	-1.034	4.308	-2.072	21.17	0.19
508	3.641	-0.610	3.088	-1.223	12.62	0.16

Table 5.8: *Values of different optical parameters in the case of TiN sample.*

5.4 Studies on PVA –TiN Nanocomposites

Nonlinear optical effects have an important role in modern photonics technology which includes generation of ultra-short technology pulses, ultrafast switching, controlling the frequency spectrum of laser light, all-optical signal processing[64]. The suitability of a material for these device applications requires a large magnitude of the third-order nonlinear optical susceptibility. Optical nonlinearities are fundamentally weak, because they are governed by photon–photon interactions enabled by materials. They are linearly dependent on the electromagnetic field and can be strengthened in material environments that provide mechanisms for field enhancement. An increased effective nonlinear optical response can be achieved through plasmonic effects. Such effects arise from coherent oscillations of conduction electrons near the surface of noble metal structures. The resonance frequency of surface plasmons depends on parameters such as nanoparticle morphology, concentration, and dielectric constant of the host where the nanoparticles are embedded. These nanoparticles when embedded in a suitable dielectric host matrix, they achieve better stability compared to a colloidal solution. If the dielectric matrix hence used offers ease of flexibility, like production of free-standing films, which can be mechanically manipulated for device applications, then it is an additional advantage. Apart from this, the incorporation of nanoparticles in a polymer matrix is found to change the optical properties of both materials. From a device point of view, polymer nanocomposites have found many potential applications in the fields of optics, electrics, mechanics, and photoconductors. Poly Vinyl alcohol (PVA) is one such polymer which has recently been demonstrated to be a useful alternative to the bulk polymer, as its high surface area and mechanical properties are interesting for various applications[65,66].

In this section we report a comparative evaluation of the optical characterization of TiN/PVA composites deduced from Z-scan experiment as well as from theoretical method entailing Tichy and Ticha relation pooled with Miller's generalized rule[67]. Simple semi-empirical relation based on generalized Miller's rule allows an estimation of nonlinear susceptibility ($\chi^{(3)}$) and non-linear refractive index (n_2) from linear refractive index and from the dispersion energy and the energy of effective oscillator of the Wemple-Di Domenico model. Z-scan is one of the simple experimental methods employed for these studies. Among other experimental methods it is one of single experiment that completely determines the physical processes behind the nonlinear response of a given material. Here, the results obtained from the experimental method were very large when compared to the results obtained from the theoretical method. The possible reasons for such large deviations are discussed in the present section. These results are discussed in terms of multipolar interactions among particles and enormous local resonance effects that appear due to particle coalescence and the increase in size of the nanoparticles, these aspects cannot be taken into consideration while evaluating the nonlinear parameters theoretically.

5.4.1 Experimental

TiN nanoparticles of average size 100 nm were purchased from Plasma Chem, Berlin and were used without any further processing. The PVA/TiN composite membranes were prepared by a sol-gel casting method. Appropriate weight of PVA (4.5gm) was dissolved in 20ml of distilled water under stirring and heated (70°C) for 1 hour and then the PVA solution was left for 15min to get cooled at room temperature, then the solution of water comprising TiN powder (0.15g) was added slowly to the PVA solution with stirring. The nanocomposites were further obtained as a free standing film by using the Tape casting instrument. These films were then used for further investigation. Experimental procedures consisted of recording the absorption and transmittance spectra by using a spectrophotometer (JascoV-570 UV/VIS/IR). The nonlinear optical characterization was carried out using Z-scan experiment.

5.4.2 Results and Discussions

i. Theoretical Evaluation

The absorption spectrum of the composite is presented in Figure 5.39 with the inset graph showing the absorption spectrum of PVA film alone. Analysis of optical absorption spectra is one of the most productive tools for understanding the band structure and energy band gap, Eg. The inset graph clearly indicates that PVA film does not possess significant optical absorption in the visible region. The absorption coefficient (α) of these materials is determined from the absorption spectra.

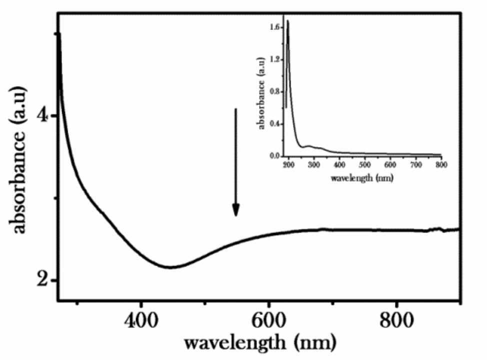

Figure 5.39: *Absorption spectra of the titanium nitride nanoparticle embedded in PVA matrix. Inset graph shows the absorption spectrum of pure PVA film.*

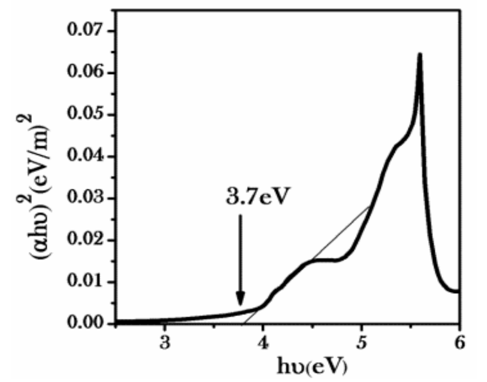

Figure 5.40: *Band gap calculation of the nano particle as per Tauc's plot.*

The optical energy gap (Eg) of thin films is determined from absorption coefficient data represented in Figure 5.40 as a function of photon energy as proposed by Tauc et.al. The optical absorption edge was analysed with Tauc equation,

$$\alpha h\upsilon = A(h\upsilon - Eg)^m \qquad (5.4)$$

Here, A is the optical constant, α is the absorption coefficient and m=0.5. Eg is the optical band which corresponds to 3.7 eV.

The complex refractive index for the film, with uniform thickness, d, is defined by the relation $n_c = n - i.k$[68], where n is the refractive index and k is the extinction coefficient. The extinction coefficient (k) and refractive index (n) are important parameters for assessing photonic materials .Values of n and k can be calculated from absorption spectra using the relation

$$k = \frac{\alpha\lambda}{4\pi} \tag{5.5}$$

where λ is the wavelength.

The refractive index (n) can be calculated from the reflection spectra using the relation[69]

$$R = \frac{(n-1)^2 + k^2}{(n+1)^2 + k^2} \tag{5.6}$$

The real part and imaginary part of the dielectric constant characterises the loss factor. The real part of the dielectric constant determines the measure by which it will slow down the speed of light in the material and the imaginary part displays the dielectric energy absorbed from an electric field due to dipole motion. The dielectric constant (ε_r) and dielectric loss (ε_i) are determined from

$$\varepsilon_r = n^2 - k^2 \tag{5.7}$$

$$\varepsilon_i = 2nk \tag{5.8}$$

Optical conductivity can also be calculated from,

$$\sigma = \frac{\alpha n c}{4\pi} \tag{5.9}$$

where c is the velocity of light. Based on the single-oscillator model, Wemple- Di Domenico (WDD)[70], semi-empirical relation for determining the refractive index, n at photon energies (hν) can be written as

$$n^2(h\upsilon) - 1 = \frac{E_0 E_d}{E_0^2 - (h\upsilon)^2} \tag{5.10}$$

where h is the Plank constant, υ is the frequency, E_0 is the oscillator energy and E_d is the dispersion energy which is measure of the average strength of inter-band optical transition or the oscillator strength. The oscillator energy, E_0, is related to the optical band gap, Eg in approximation given as $E_0 \approx 2Eg$. The dispersion energy (E_d) refers to the average strength of interband optical transitions and is related to the chemistry of a material ie, E_d is related to ionicity, anion valency, coordination number, whereas E_0 is related to bond energy or band gap. From WDD dispersion parameters E_0 and $E_{d,}$ the linear refractive index dispersion (n_0) is given by the formula[71,72]

$$n_0 = (1 + E_d/E_0)^{0.5} \tag{5.11}$$

Simple empirical relation based on generalized Miller's rule can be used for the determination of the nonlinear refractive index (n_2) and susceptibility ($\chi^{(3)}$). These values are calculated by combining Miller's generalized rule and the relation concerning linear susceptibility ($\chi^{(1)}$) and third order nonlinear susceptibility ($\chi^{(3)}$) involving parameters from WDD single oscillator model[73,74]. The ($\chi^{(3)}$) value is given as

$$\chi^{(3)} = A\,(\chi^{(1)})^4 \tag{5.12}$$

Optical susceptibility then is given by (in esu)

$$\chi^{(1)} = \frac{E_d}{4\pi E_0} \tag{5.13}$$

Non-linear refractive index (n_2) is related to the third-order susceptibility by

$$n_2 = \frac{12\pi\chi^{(3)}}{n_0} \tag{5.14}$$

where n_0 is the static refractive index.

The various values of the optical parameters calculated using the above relations are tabulated as in table 5.9.

Sl.No	Optical parameters	Estimated values
1	Band gap (E_g)	3.7 eV
2	Extinction coefficient (k)	1.0187×10^{-5}
3	Dielectric constant (ε_r)	3.629
4	Dielectric loss (ε_i)	3.8812×10^{-5}
5	Optical Conductivity (σ)	1.09436×10^{10}
6	Oscillator energy (E_o)	7.46 eV
7	Dispersion energy (E_d)	19.626 eV
8	Static refractive index (n_0)	1.90526
9	Linear susceptibility (χ^1)	0.20929
10	Third order nonlinear susceptibility (χ^3)	3.2617×10^{-13} (esu)
11	Nonlinear refractive index (n_2)	6.4538×10^{-12} (esu)

Table 5.9: *Estimated values of different optical parameters of TiN/PVA nanocomposite at 532nm.*

ii. Experimental Evaluation

UV-Vis spectrum recorded using a spectrometer is shown in Figure 5.38. The step like function corresponds to the surface plasmon resonance band (SPR) of the sample at around 550 nm. Here, such an enormous SPR Bandwidth in the absorption spectrum can be due to increase in the concentration of titanium nitride in PVA matrix beyond the percolation threshold. Because of such high concentration of the nanoparticles, particles start interacting within the aggregates and hence sample shows a transmission window in the resonant region. This phenomenon is consistent with the theoretical prediction[75]. Figure 5.41 (a&b) shows the SEM and TEM images of the TiN nanoparticles embedded in PVA matrix. It is seen that instead of separated individual particles they lay in the matrix as a continuous network. Such a growth occurs when the smallest stable clusters nucleate on the substrate and grow in three dimensions to form a continuous network.

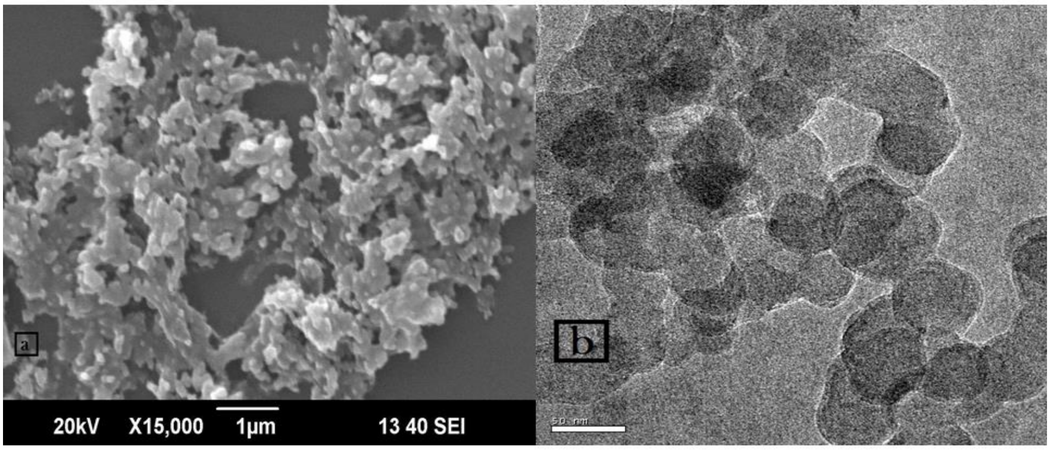

Figure 5.41: *SEM (a) and TEM (b) images of the TiN nanoparticles.*

The technique of open-aperture Z-scan scheme was employed to study the nonlinear optical properties of the system. The normalized transmittance for the open-aperture condition is given as

$$T = q^{-1}(1+q) \tag{5.15}$$

$$\text{where, } q = \frac{\beta I_0 L_{eff}}{\left(1+{Z^2}/{Z_0^2}\right)} \tag{5.16}$$

Here I_0 is the laser intensity in the focal plane, β is the nonlinear absorption coefficient and L_{eff} is the effective thickness with linear absorption coefficient α. L_{eff} is given by

$$L_{eff} = \frac{1 - e^{-\alpha l}}{\alpha} \tag{5.17}$$

Open aperture Z-scan curves recorded at wavelength 532 nm with laser power density of 290 MW/cm^2 is shown in Figure 5.42a. The Curve shows Reverse Saturable Absorption curve (RSA). The reason proposed is that two-photon absorption (TPA) leads to direct pumping of the electrons to free carrier band via the surface plasmon state. The values of nonlinear absorption coefficient, calculated by fitting Eq. (13) to experimental data were found and are given in the table 5.10. In order to ensure the role of PVA in the nonlinear optical property of nanocomposite Z-scan was performed with pure PVA film and as expected no significant output signal was obtained. The imaginary part of susceptibility Im $\{\chi^{(3)}\}$ is given by:

$$\beta = \left(\frac{2\pi^2}{n_0} \varepsilon_0 c\lambda\right) \mathrm{Im}\,\{\chi^3\} \tag{5.18}$$

Here the transmission of the sample was measured without an aperture in the far field of the lens as the sample was moved through the focal point. This enables the nonlinear refractive index (closed aperture) to be separated from that of the nonlinear absorption (open aperture). Figure 5.42 b shows the closed aperture Z-scan of the sample. For samples with considerable refractive and absorptive nonlinearities, closed-aperture measurements comprise contributions from both the intensity-dependent changes in the transmission and in refractive index .By dividing the normalized closed-aperture transmittance by the corresponding normalized open-aperture data, phase distortion created due to the change in refractive index can be retrieved. Curve revealed that the nanoparticle has negative nonlinear refractive index indicated by the peak–valley shape satisfying the condition $\Delta z \sim 1.7 z_0$ thus confirming the presence of cubic non linearity. Similar results were obtained when the procedure was repeated at various laser power densities.

The value of n_2 can be found from the theoretical fit as per Eq. (17)

$$T(z, \Delta\varphi_0) = 1 - \frac{4\Delta\varphi_0 x}{(x^2 + 9)(x^2 + 1)} \tag{5.19}$$

Here, $x = z/z_0$

The nonlinear refractive index n_2 and the real part of nonlinear susceptibility Re $\{\chi\}$ are related as

$$\mathrm{Re}\{\chi^3\} = 2n_2\, \varepsilon_0 n_0^2 c \tag{5.20}$$

where n_2

$$n_2 = \frac{\Delta\varphi_0\lambda}{2\pi I_0 \mathrm{Leff}} = \frac{\Delta T_{p-v}}{0.406(1-s)^{0.25}\, k\, L_{eff}\, I_0} \tag{5.21}$$

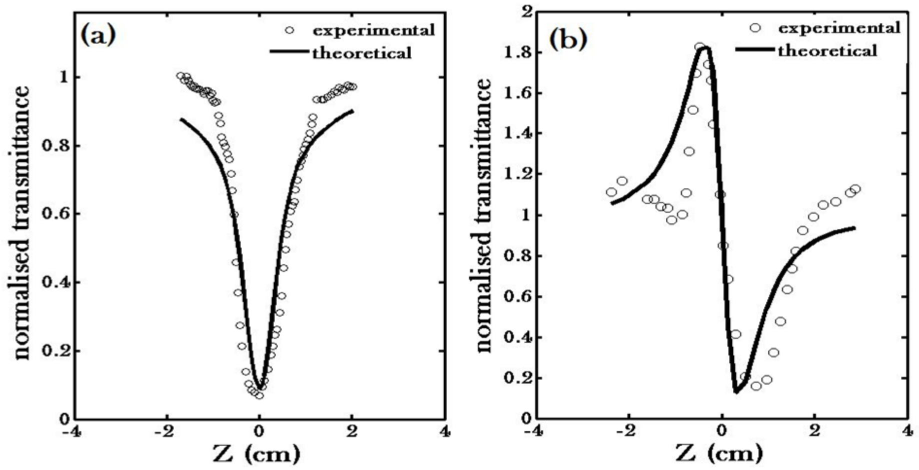

Figure 5.42: *(a) Open aperture and (b) closed aperture Z-scan experiment of the TiN nanoparticles in PVA matrix at 290 MW/cm^2.The solid line represent the theoretical curve. .Similar results were obtained at other laser power intensities as well.*

Different optical parameters Im{$\chi^{(3)}$}, n_2, Re{ $\chi^{(3)}$} were calculated and are listed in the table 5.10.

Optical parameters	Theoretically estimated values (esu)	Experimental values from Z-scan Experiment (esu)
Third order nonlinear susceptibility (χ^3)	3.2617×10^{-13}	$1.905 \pm 0.5 \times 10^{-9}$
Nonlinear refractive index (n_2)	6.4538×10^{-12}	$9.122 \pm 1.5 \times 10^{-9}$

Table 5.10: *Comparison of values of optical parameters of TiN/PVA nanocomposites at 532nm obtained theoretically and from Z-scan Experiment.*

It was observed that the values of the optical parameters calculated from Z-scan experiment were much larger than that calculated theoretically from Tichy and Ticha relation combined with generalised Miller's rule. The reason for such an incongruity can be ascribed to the role of Surface Plasmon Resonance which gets boosted during Z-scan experiment. The theoretical method doesn't take into effect the influence of SPR property of the nano particles. The significant nonlinear optical response can be attributed to the plasmon resonance, which largely enhances the local field in the particle. The local field inside a particle, E_{loc} , is related to the applied field, E_0,by[76].

$$\mathrm{E_{loc}} = \frac{E}{E_0} = \frac{3\varepsilon_m(\omega)}{\varepsilon_m(\omega) + 2\varepsilon_d(\omega)}\mathrm{E_0} \tag{5.22}$$

where $\varepsilon = \varepsilon_R + i\varepsilon_{im,}$ ε_d is the dielectric function of the host matrix and ε is of the nanoparticle. For SPR, $\varepsilon_m(\omega) + 2\varepsilon_d(\omega) = 0$ .The effective third order nonlinear susceptibility is given as

$$\chi_{\mathrm{eff}}^{(3)} = \frac{\int \chi^{(3)}\, |\mathrm{E_{loc}}|^2 \mathrm{E_{loc}^2 dV}}{\mathrm{V}\left||\mathrm{E_0}|\right|^2 \mathrm{E_0^2}} \tag{5.23}$$

Thus the net third-order susceptibility $\chi^{(3)}$ results from the susceptibility of the nanoparticles, which gets strongly enhanced through the amplification of the local field E_{loc} near the SPR frequency. Interestingly such an enormous enhancement factor cannot be accounted merely by the presence of SPR. Here, as mentioned before it has been observed that the particles are above coalescence threshold, as evident from the chain like network formation in figure 5.41. Hence both the linear absorption in the near-infrared and the third order nonlinear optical susceptibility at the SPR wavelength are greatly enhanced. Beyond the percolation threshold coalescence becomes significant. Hence electromagnetic coupling within the coalesced particles behave as electromagnetically coupled entities[77]. It has been reported that multipolar extinction and multiple particle interactions increase the absorption coefficient of nanocomposites at photon energies lower than that of the SPR and are responsible for the anomalous IR absorption very often reported in metal-dielectric composites[78,79,80,81]. Around the percolation threshold, the presence of multiple particle scattering leads to an enhancement of the local electric field and hence a corresponding increase in $\chi_{\mathrm{eff}}^{(3)}$. Scattering from such percolated particles is denoted as percolation-enhanced nonlinear scattering (PENS)[82]. PENS is caused by the giant scale field fluctuations resulting from plasmon localization .This effect is enriched by the presence of a particle network, that concentrate the electric field leading to local giant field enhancement effects of $\chi_{\mathrm{eff}}^{(3)}$ as reported [83,84,85,86]. There are reports related to ''granular metal microstructure'' effective medium theory and the wide theoretical work about giant surface- enhanced optical nonlinearities in semi continuous metal-dielectric films. These results predicts an enhancement of the effective third order nonlinear optical susceptibility of several orders of magnitude at high metal volume fractions leading to the appearance of localized sharp electric fields associated with the localization of surface plasmon modes. The plasmon localization leads to the electromagnetic energy being concentrated in sharp nm-sized peaks, namely ‘‘hot spots’’. The local fields in such hot spots have been shown to be enhanced enormously, with the intensity I_{loc} exceeding the applied intensity I_0 by four to five orders of magnitude. Such local-field enhancements associated with the hot spots are important for amplifying nonlinear optical processes such as surface-enhanced Raman scattering (SERS)[87,88].

5.5 Conclusions

- ☐ TiO_2-SiO_2 semiconductor doped glass systems of various compositions were synthesised. Linear and nonlinear optical properties were studied using optical absorption, and open as well as closed aperture Z-scan technique. Structural characterizations were done using XRD. The nanocomposites showed enhanced nonlinear optical properties compared to pure TiO_2 and this can be attributed to the surface states and weak dielectric confinement of TiO_2 nanoparticles by SiO_2 matrix.The nanocomposites were thermally treated and similar studies were performed. The anatase form of TiO_2 in the nanocomposites showed superior properties relative to the amorphous and rutile phase of the composite. The involved mechanism is explained by taking into account the dominant role played by the excitons in the TiO_2 nanoparticles. Optical limiting characteristics were also studied and their potential candidature for optical limiting applications was confirmed.

- ☐ TiO_2-CeO_2 nanocomposites with different compositions were synthesized using sol gel method. Their band gap variation has been studied. It has been observed that as the dopant concentration increases the band gap decreases and this narrowing of band gap can be attributed to the formation of Ce 4f and oxygen defect levels smearing out to the forbidden energy gap of the host. Photoluminescence spectra were also studied and quenching phenomenon was found to occur. It is proposed that it might be due to the increase in interaction among Ce^{3+} ions and thus energy gets dissipated among them and intensity decreases accordingly. Nonlinear studies were carried out using Z-scan. It was observed that the nanocomposites showed commendable non linearity owing to two photon absorption and their β coefficient decreased with the increase in input power. Finally their optical limiting ability was also analysed and it showed their potential applicability in the fabrication of nonlinear devices such as optical switches, power limiters and phase conjugators and so on. Nonlinear refractive index of the nano composite was also estimated. Variation of the nonlinear index of refraction was studied with respect to power as well as composition. Switching in the sign of refractive index occurred in both cases and possible reasons for the same were discussed as well.

- By using Z-scan technique, we have determined the third-order nonlinear optical susceptibility of TiN nanoparticles. The large third-order nonlinear optical susceptibility of the nanoparticles is due to the surface plasmon resonance and the thermal effects are discussed. The enhancement of nonlinear optical response makes it a promising material in photonics applications. The optical limiting curves are also obtained for which limiting thresholds are clearly portrayed. Post excitation absorption spectra revealed interesting phenomenon of photo fragmentation leading to blue shift in band gap and red shift in the SPR. The results are discussed in terms of enhanced interparticle interaction coupled with size reduction. Here, the optical constants being intrinsic constants for a particular sample changes unusually with laser power intensity .The dependence of $\chi^{(3)}$ are discussed in terms of size variation caused by photo fragmentation .The studies proved that the TiN nanoparticles are potential candidates in photonics technology offering huge scope of unexplored research for various expedient applications.

- The optical constants (refractive index n, absorption coefficient α and extinction coefficient, k) of TiN/PVA nanocomposites thin films were determined by simple calculations using only the absorption spectra. The oscillator energy (E_0) was found to follow the empirical relation with the optical energy gap. The nonlinear susceptibility $\chi^{(3)}$, non-linear refractive index (n_2), the dispersion energy (E_d) were calculated. Simultaneously the nonlinear parameters were also calculated using Z-scan Experiment. Z-scan results gave much larger values of nonlinear optical parameters and this discrepancy in values can be attributed to the role of SPR of TiN nanoparticles which lies close to the irradiated laser beam wavelength of 532 nm. Studies showed that particles are above the percolation threshold leading to particle coalescence and hence their optical response are greatly influenced by the multiple particle interaction and giant local resonance effect leading to high values of optical non linearity.

5.6 References

---

[1] Divya, S., Sebastian, I., Nampoori, V. P. N., Radhakrishnan, P., & Mujeeb, A. (2014). "Band gap tuning and nonlinear optical characterization of TiO_2-SiO_2 nanocomposites with respect to composition and phase". *Opt. Mater.*, *37*, 433-438.

[2] Martucci, A., Fick, J., Schell, J., Battaglin, G., & Guglielmi, M. (1999). "Microstructural and nonlinear optical properties of silica–titania sol-gel film doped with PbS quantum dots". *J. Appl. Phys.*, *86*(1), 79-87.

[3] Hemissi, M., and H. Amardjia-Adnani. (2007) "Optical and structural properties of titanium oxide thin films prepared by sol-gel method". *Dig J. Nanomater. Bios* 2(4) 299-305.

[4] Wu, X., Wang, R., Zou, B., Wu, P., Wang, L., Xu, J., & Huang, W. (1997). "The effects of different interfacial environments on the optical nonlinearity of nanometer-sized CdO organosol". *Appl. Phys. Lett.*, *71*(15), 2097-2099.

[5] Dutoit, D. C. M., M. Schneider, and A. Baiker. (1995) "Titania-silica mixed oxides I. Influence of sol-gel and drying conditions on structural properties". *J. Catal.*, 153(1), 165-176.

[6] Oral, A. Y., Menşur, E., Aslan, M. H., & Başaran, E. (2004). "The preparation of copper (II) oxide thin films and the study of their microstructures and optical properties". *Mater. Chem. Phys.*, *83*(1), 140-144.

[7] Zhang, Xiaojun, and Huagui Zheng. (2008) "Synthesis of TiO_2-doped SiO_2 composite films and its applications". *Bull. Mater. Sci.* ,31(5), 787-790.

[8] Schmitt-Rink, Stefan, D. A. B. Miller, and D. Si Chemla. (1987) "Theory of the linear and nonlinear optical properties of semiconductor microcrystallites". *Phys. Rev. B: Condens. Matter* 35(15), 8113.

[9] Wang, Y., Suna, A., McHugh, J., Hilinski, E. F., Lucas, P. A., & Johnson, R. D. (1990). "Optical transient bleaching of quantum-confined CdS clusters: The effects of surface-trapped electron–hole pairs". *J. Phys. Chem.* , *92*(11), 6927-6939.

[10] Tang, H., Berger, H., Schmid, P. E., & Levy, F. (1994). "Optical properties of anatase (TiO_2)". *Solid State Commun.*, *92*(3), 267-271.

[11] Bagnall, D. M., Chen, Y. F., Zhu, Z., Yao, T., Koyama, S., Shen, M. Y., & Goto, T. (1997). "Optically pumped lasing of ZnO at room temperature". *Appl. Phys. Lett.*, *70*(17), 2230-2232.

[12] A.Fujishima and K.Honda. (1972)."Electrochemical Photocatalysis of Water at a Semiconductor Electrode". *Nature*, 238 (5358) 37-38.

[13] Ohtani, B., Bowman, R. M., Colombo, D. P., Kominami, H., Noguchi, H., & Uosaki, K. (1998). "Femtosecond diffuse reflectance spectroscopy of aqueous Titanium (IV) oxide suspension: Correlation of electron-hole recombination kinetics with photocatalytic activity". *Chem. Lett.*, *27*(7), 579-580.

---

[14] A. Fujishima, X. T. Zhang and D. A. Tryk. (2008). “TiO_2 Photocatalysis and Related Surface Phenomena”. *Surf. Sci. Rep*. 63(12) 515-582.

[15] J. C. Zhao, C. C. Chen and W. H. Ma. (2005). “Photocatalytic Degradation of Organic Pollutants under Visible Light Irradiation”. *Top. Catal*., 35(3-4), 269-278

[16] S. Klosek, D. Raftery. (2001). “Visible-light driven V-doped TiO2 photocatalyst and its photooxidation of ethanol”. *J. Phys. Chem. B, 105, 2815* -2819.

[17] M Satish, B Vishwanathan, R P Vishwanath & C S Gopinath.(2005). “ Synthesis, characterization, electronic structure, and photocatalytic activity of nitrogen-doped TiO_2 nanocatalyst”. *Chem. Mater*., 17, 6349-6353.

[18] Y Bassekhouad, N Chaoui , M Trzpit, N Ghazzal, D Robert, & J V Weber. (2006) . “UV-Vis versus visible degradation of Acid Orange II in a coupled CdS/TiO_2 semiconductors suspension.films” *J. Photoch. Photobio. A*,183, 218 -224.

[19] Magesh, G., Viswanathan, B., Viswanath, R. P., & Varadarajan, T. K. (2009). Photocatalytic behavior of CeO_2-TiO_2 system for the degradation of methylene blue. *Indian J. Chem. A*, *48*(4), 480-488.

[20] Y Xie & C Yuan. (2004). “ Photocatalysis of neodymium ion modified TiO_2 sol under visible light irradiation.”*Appl. Surf. Sci*., 221,17-24.

[21] T Tong, J Zhang, B Tian, F Chen, D He & M Anpo. (2007). “ Preparation of Ce-TiO_2 catalysts by controlled hydrolysis of titanium alkoxide based on esterification reaction and study on its photocatalytic activity”. *J. Colloid Interface Sci.*,351,382-8.

[22] P. F. Ji, J. L. Zhang, F. Chen and M. Anpo.(2009). “Study of Adsorption and Degradation of Acid Orange 7 on the Surface of CeO_2 under Visible Light Irradiation,” *Appl. Catal., B,* 85 (3-4), 148- 154.

[23] G. R. Bamwenda, K. Sayama and H. Arakawa. (1999). “The Photoproduction of O_2 from a Suspension Containing CeO_2 and Ce^{4+} Cations as an Electron Acceptor”. *Chem. Lett.,* 28(10), 1047-1048.

[24] S. Liu, X. J. Zhao, N. Z. Zhang, Q. N. Zhao, X. He, and J. Y. Feng.(2005) ‘‘Photocatalytic Mechanism of TiO_2–CeO_2 Films Prepared by Magnetron Sputtering under UV and Visible Light”, *Surf. Sci.,* 595, 203–11.

[25] A W Xu, Y Gao and H Q Liu .(2002). “The preparation, characterisation and their photocatalytic activities of rare earth doped TiO_2 nanoparticles”. *J. Catal.,* 207 151-157.

[26] Yen, W M, M. Raukas, S A Basun, W V Schaik and U Happek. (1996). “ Optical and photoconductive properties of cerium doped crystalline solids”. *J. Lumin.,* 69, 287–294.

[27] C Chinnock. (1994). “Laser-based systems easily find semiconductor defects ”Laser focus world, 30 28-34.

---

[28] Verma, A., & Joshi, A. G. (2009). Structural, optical, photoluminescence and photocatalytic characteristics of sol-gel derived CeO2-TiO2 films. *Indian J. Chem. A, 48*(2), 161-167.

[29] Li, F. B., X. Z. Li, M. F. Hou, K. W. Cheah and W. C. H. Choy. (2005). " Enhanced photocatalytic activity of Ce^{3+}-TiO_2 for 2-mer-captobenzothiazole degradation in aqueous suspension for odour control ". *Appl. Catal., A*,285,181–189.

[30] J Xiea , D. Jianga,M. Chena, D. Lia, J. Zhua, X. Lua and C. Yan. (2010) . "Preparation and characterization of monodisperse Ce-doped TiO_2 microspheres with visible light photocatalytic activity". *Colloids Surf., A*,372,107–114.

[31] Fu, C., T. Li, J. Qi, J. Pan, S. Chen and C. Cheng. (2010). "Theoretical study on the electronic and optical properties of Ce^{3+} doped TiO_2 photocatalysts". *Chem. Phys. Letters*, 494 ,117–122.

[32] Chen, S. W., Lee, J. M., Lu, K. T., Pao, C. W., Lee, J. F., Chan, T. S., & Chen, J. M. (2010). "Band-gap narrowing of TiO2 doped with Ce probed with x-ray absorption spectroscopy". *Appl. Phys. Lett., 97*(1), 2104.

[33] Deng, H., & Hossenlopp, J. M. (2005). "Combined X-ray diffraction and diffuse reflectance analysis of nanocrystalline mixed Sn (II) and Sn (IV) oxide powders".*J. Phys. Chem. B, 109*(1), 66-73.

[34] Yang, J., Y. Q. Gao, J. Wu, Z. M. Huang, X. J. Meng, M. R.Shen, J. L. Sun and J. H. Chu. (2010). " Temperature dependent optical properties of Mn doped (Pb,Sr)TiO3 foller electric films in absorption region: Electron phonon interaction". *J. Appl. Phys.*,108, 114102–114106.

[35] Choudhury, B., Borah, B., & Choudhury, A. (2012). "Extending photocatalytic activity of TiO_2 nanoparticles to visible region of illumination by doping of cerium". *J. Photochem. Photobiol., 88*(2), 257-264.

[36] Wang, Z., Quan, Z., & Lin, J. (2007). "Remarkable changes in the optical properties of CeO_2 nanocrystals induced by lanthanide ions doping". *Inorg. Chem., 46*(13), 5237-5242.

[37] Yin, L., Wang, Y., Pang, G., Koltypin, Y., & Gedanken, A. (2002). "Sonochemical synthesis of cerium oxide nanoparticles—effect of additives and quantum size effect". *J. Colloid Interface Sci.*, 246(1), 78-84.

[38] Chen, S. W., Lee, J. M., Lu, K. T., Pao, C. W., Lee, J. F., Chan, T. S., & Chen, J. M. (2010). "Band-gap narrowing of TiO_2 doped with Ce probed with x-ray absorption spectroscopy". *Appl. Phys. Lett., 97*(1), 2104.

[39] S. X. Wang, L. D. Zhang, H. Su, Z. P. Zhang, G. H. Li, G. W.Meng, J. Zhang, Y. W. Wang, J. C. Fan, and T. Gao. (2001). " Two-photon absorption and optical limiting in poly (styrene maleic anhydride) /TiO_2 nanocomposites" *Phys. Lett. A*, 281,59-63.

[40] D. Torres-Torres, M. Trejo-Valdez, L. Castañeda,C. Torres-Torres, L. Tamayo-Rivera, R. C. Fernández-Hernández, J. A. Reyes-Esqueda, J. Muñoz-Saldaña, R.Rangel-Rojo, and A. Oliver. (2010). "Inhibition of the two-photon absorption response exhibited by a bilayer TiO_2 film with embedded Au nanoparticles". *Opt. Express*, 18(16) 16406-16417.

---

[41] M. Sheik-Bahae, D. J. Hagan,and E. W. Van Stryland. (1990). " Dispersion and Band-Gap Scaling of the Electronic Kerr Effect in Solids Associated With 2-Photon Absorption " *Phys. Rev. Lett.*,65,96-99.

[42] B. S. Wherrett, A. C. Walker, and F. A. P. Tooley.(1988)." Optical Nonlinearities and Instabilities in Semiconductors". edited by H. Haug (*Academic, New York*) 239-272.

[43] B. T. Draine and P. J. Flatau, Flatau, P. J., & Draine, B. T .(1994)." Discrete-dipole approximation for scattering calculations". *JOSA*, 11, 1491.

[44] Chen, Feifei, Shixun Dai, Tiefeng Xu, Xiang Shen, Changgui Lin, Qiuhua Nie, Chao Liu, and Jong Heo. (2011). "Surface-plasmon enhanced ultrafast third-order optical nonlinearities in ellipsoidal gold nanoparticles embedded bismuthate glasses". *Chem. Phys. Lett.* 514(1), 79-82.

[45] West, R., Y. Wang, and T. Goodson III. (2003). "Nonlinear absorption properties in novel gold nanostructured topologies". *J. Phys. Chem. B* 107(15), 3419-3426.

[46] Blaber, M. G., Arnold, M. D., Harris, N., Ford, M. J., & Cortie, M. B. (2007). " Plasmon absorption in nanospheres: A comparison of sodium, potassium, aluminium, silver and gold". *Physica B: Condens. Matter, 394*(2), 184-187.

[47] Blaber, Martin G., Matthew D. Arnold, and Michael J. Ford. (2009). "Search for the ideal plasmonic nanoshell: the effects of surface scattering and alternatives to gold and silver". *J. Phys. Chem. C*, 113(8),3041-3045.

[48] Naik, G. V., Schroeder, J. L., Ni, X., Kildishev, A. V., Sands, T. D., & Boltasseva, A. (2012). Titanium nitride as a plasmonic material for visible and near-infrared wavelengths. *Opt. Mater. Express*, *2*(4), 478-489.

[49] M B Cortie, J Giddings and A Dowd. (2010). "Optical properties and plasmon resonances of titanium nitride nanostructures". *Nanotechnology,* 21, 115201.

[50] Naik, Gururaj V., and Alexandra Boltasseva. (2010). "Semiconductors for plasmonics and metamaterials". *physica status solidi* (RRL), 4(10), 295-297.

[51] Mizrahi, V., Saifi, M. A., Andrejco, M. J., DeLong, K. W., & Stegeman, G. I. (1989). Two-photon absorption as a limitation to all-optical switching. *Opt. Lett.*, *14*(20), 1140-1142.

[52] Reinholdt, A., Pecenka, R., Pinchuk, A., Runte, S., Stepanov, A. L., Weirich, T. E., & Kreibig, U. (2004). "Structural, compositional, optical and colorimetric characterization of TiN-nanoparticles". *EPJ D*, *31*(1), 69-76.

[53] Blaber, Martin G., Matthew D. Arnold, and Michael J. Ford. (2009). "Search for the ideal plasmonic nanoshell: the effects of surface scattering and alternatives to gold and silver". *J. Phys. Chem. C*,113(8),3041-3045.

[54] Ghosh, Sujit Kumar and Tarasankar Pal. (2007). "Interparticle coupling effect on the surface plasmon resonance of gold nanoparticles: from theory to applications". *Chem. Rev.-Columbus* 107(11),4797-4862.

[55] Zhong, Z., Patskovskyy, S., Bouvrette, P., Luong, J. H., & Gedanken, A. (2004). “The surface chemistry of Au colloids and their interactions with functional amino acids”.*J. Phys. Chem. B, 108*(13), 4046-4052.

[56] Tauc, J., R. Grigorovici, and A. Vancu. (1966). “Optical properties and electronic structure of amorphous germanium”. *physica status solidi (b),* 15(2),627-637.

[57] Philip, R., Kumar, G. R., Sandhyarani, N., & Pradeep, T. (2000). “Picosecond optical nonlinearity in monolayer-protected gold, silver, and gold-silver alloy nanoclusters”. *Phys. Rev. B: Condens. Matter*, *62*(19), 13160.

[58] Creighton, J. A., Alvarez, M. S., Weitz, D. A., Garoff, S., & Kim, M. W. (1983). “Surface-enhanced Raman scattering by molecules adsorbed on aqueous copper colloids”.*J. Phys. Chem., 87*(24), 4793-4799.

[59] Bigot, J. Y., Halté, V., Merle, J. C., & Daunois, A. (2000). Electron dynamics in metallic nanoparticles. *Chem. Phys.*, *251*(1), 181-203.

[60] Unnikrishnan, K. P., Nampoori, V. P. N., Ramakrishnan, V., Umadevi, M., & Vallabhan, C. P. G. (2003). Nonlinear optical absorption in silver nanosol. *J. Phys. D: Appl. Phys.*, *36*(11), 1242.

[61] Garcia, M. A. (2011).“Surface plasmons in metallic nanoparticles: fundamentals and applications”. *J. Phys. D: Appl. Phys*., 44(28), 283001.

[62] Sheik-Bahae, Mansoor, Ali A. Said, and Eric W. Van Stryland. (1989). "High-sensitivity, single-beam n_2 measurements”. *Opt. Lett.,* 14(17),955-957.

[63] Stegeman, G. I. (1993, July). Material figures of merit and implications to all-optical waveguide switching. In *OE/LASE'93: Optics, Electro-Optics, & Laser Applications in Science& Engineering* (pp. 75-89). International Society for Optics and Photonics.

[64] R. W Boyd, Nonlinear Optics,3rd ed. (Academic, 2008).

[65] Supaphol, Pitt, and Surawut Chuangchote. (2008). “On the electrospinning of poly (vinyl alcohol) nanofiber mats: A revisit”. *J. Appl. Polym. Sci.,* 108(2), 969-978.

[66] Shao, C., Kim, H. Y., Gong, J., Ding, B., Lee, D. R., & Park, S. J. (2003). Fiber mats of poly (vinyl alcohol)/silica composite via electrospinning. *Mater. Lett., 57*(9), 1579-1584.

[67] Ticha, H., and L. Tichy. (2002). “Semiempirical relation between non-linear susceptibility (refractive index), linear refractive index and optical gap and its application to amorphous chalcogenides”. *J. Optoelectron. Adv. Mater* 4.2: 381-386.

[68] Meng, Li-jian, M. Andritschky, and M. P. Dos Santos. (1993). “The effect of substrate temperature on the properties of dc reactive magnetron sputtered titanium oxide films”. *Thin Solid Films,* 223(2), 242-247.

[69] El-Raheem, MM Abd. (2007). “Optical properties of GeSeTl thin films”. *J. Phys.: Condens. Matter,* 19.21: 216209.

---

[70] Bhaskar, S., Majumder, S. B., Jain, M., Dobal, P. S., & Katiyar, R. S. (2001). “Studies on the structural, microstructural and optical properties of sol–gel derived lead lanthanum titanate thin films”. *Mater. Sci. Eng., B, 87*(2), 178-190.

[71] Tintu, R., K. Saurav, K. Sulakshna, V. P. N. Nampoori, P. Radhakrishnan, and Sheenu Thomas. (2010). “Ge28Se60Sb12/PVA Composite Films for Photonic Applications”. *J. Non-Cryst. Solids*, 2(4), 167-174.

[72] Ticha, H., and L. Tichy .(2002). “Semiempirical relation between non-linear susceptibility (refractive index), linear refractive index and optical gap and its application to amorphous chalcogenides”. *J. Optoelectron. Adv. Mater* 4(2),381-386.

[73] Wang, Charles C. (1970). "Empirical relation between the linear and the third-order nonlinear optical susceptibilities." *Phys. Rev. B: Condens. Matter,* 2, 2045-2048.

[74] Song, Shanshan, Janesha Dua, and Craig B. Arnold. (2010)."Influence of annealing conditions on the optical and structural properties of spin-coated As_2S_3 chalcogenide glass thin films." *Opt. Express* 18(6), 5472-5480.

[75] Sheng, Ping. (1980). “Theory for the dielectric function of granular composite media”. *Phys. Rev. Lett.,* 45(1),60-63.

[76] Debrus, S., Lafait, J., May, M., Pincon, N., Prot, D., Sella, C., & Venturini, J. (2000). Z-scan determination of the third-order optical nonlinearity of gold: silica nanocomposites. *J. Appl. Phys.*, *88*(8), 4469-4475.

[77] R. del Coso, J. Requejo-Isidro, J. Solis, J. Gonzalo, and C. N. Afonso.(2004). “Third order nonlinear optical susceptibility of Cu: AlO nanocomposites: From spherical nanoparticles to the percolation threshold”. *J. Appl. Phys.*,95, 2755-2762.

[78] Kreibig, U., & Vollmer, M. (1995). “Optical properties of metal clusters”.

[79] Wang, D. S., & Kerker, M. (1981). “Enhanced Raman scattering by molecules adsorbed at the surface of colloidal spheroids”. *Phys. Rev. B: Condens. Matter, 24*(4), 1777.

[80] Quinten, M. (2001). “Local fields close to the surface of nanoparticles and aggregates of nanoparticles”. *Appl. Phys. B,* 73(3), 245-255.

[81] Sarychev, Andrey K., V. A. Shubin, and Vladimir M. Shalaev. (1999). “Percolation-enhanced nonlinear scattering from metal-dielectric composites”. *Phys. Rev. E: Stat. Phys., Plasmas, Fluids,* 59(6), 7239-7242.

[82] Sarychev, A. K., & Shalaev, V. M. (2000). “Electromagnetic field fluctuations and optical nonlinearities in metal-dielectric composites”. *Phys. Rep., 335*(6), 275-371.

[83] Messinger, B. J., Von Raben, K. U., Chang, R. K., & Barber, P. W. (1981). “Local fields at the surface of noble-metal microspheres”. *Phys. Rev. B: Condens. Matter*, *24*(2), 649.

---

[84] Xu, H., Aizpurua, J., Käll, M., & Apell, P. (2000). "Electromagnetic contributions to single-molecule sensitivity in surface-enhanced Raman scattering". *Phys. Rev. E: Stat. Phys., Plasmas, Fluids*, *62*(3), 4318.

[85] Barber, P. W., Chang, R. K., & Massoudi, H. (1983). "Electrodynamic calculations of the surface-enhanced electric intensities on large Ag spheroids". *Phys. Rev. B: Condens. Matter*, *27*(12), 7251.

[86] Shalaev, V. M., & Sarychev, A. K. (1998). "Nonlinear optics of random metal-dielectric films". *Phys. Rev. B: Condens. Matter, 57*(20), 13265.

[87] Gadenne, P., Brouers, F., Shalaev, V. M., & Sarychev, A. K. (1998). " Giant Stokes fields on semicontinuous metal films". *JOSA B, 15*(1), 68-72.

[88] Breit, M., Podolskiy, V. A., Grésillon, S., Von Plessen, G., Feldmann, J., Rivoal, J. C. & Shalaev, V. M. (2001). "Experimental observation of percolation-enhanced nonlinear light scattering from semicontinuous metal films". *Phys. Rev. B: Condens. Matter*, *64*(12), 125106.

Chapter 6

Fabrication and Characterization of TiO_2 Based Dye Sensitised Solar Cells

Abstract

The performance of dye sensitized solar cells depends on the collective contributions from its constituents which include the nanoparticle film, dye, electrolyte, and the counter electrode. In this chapter, we elucidate the performance of the TiO_2 based DSSCs standardised using N719 dye and Platinum as counter electrode with various electrolytes including quasi static electrolytes. We have also evaluated the photovoltaic characteristics of the cells employing different morphologically structured TiO_2 photoanode. The DSSC based on the hierarchical anatase TiO_2 nanotree photoelectrode showed the highest optical-to-electricity conversion efficiency of 10.2%. The performance of the cell was found to be dependent on photoanode constituents which was studied by employing various TiO_2 based nanocomposites ie, TiO_2-CeO_2, TiO_2-SiO_2, TiO_2-N (TiN).

Results of this chapter are published in:

i. S. Divya et.al. *J. Appl. Phys.* 115 (2014): 064501-5

6.1 Introduction

There has been an active interest in dye-sensitized solar cells (DSSCs) since the primarily report on DSSC in 1991 by O’Regan and Grätzel due to their low cost and high energy conversion efficiency[1]. It possess the distinction of being the only photovoltaic device that uses molecules to absorb photons, converting them to electric charges without the need of intermolecular transport of electronic excitation. Also it’s the only photovoltaic device where two functions of light harvesting and charge-carrier transport occur separately. High light harvesting, rapid electron transport and the minimum electron-hole recombination are essential for the efficient working of a DSSC. Especially, the light-harvesting efficiency of the photoanode is the most important and central factor for the high-efficiency DSSC, which in turn is principally related to the molar extinction coefficient of the sensitizer, the dye-loading capacity of the porous electrode, and the optical path of the incident light in the electrode. There are mainly two components concerning the light-harvesting property of DSSC, the dye and the mesoporous electrode supporting the sensitizer. The development of novel sensitizers with higher molar extinction coefficient and better response to near-infra-red wavelength has been long studied since the first breakthrough of DSSC. The significance of the light scattering and/ reflection of the mesoporous electrode on the light-harvesting properties have been realized only in recent years. In view of the different optical and photoelectrical nanostructures involved in these studies and their rapid progresses, it is worth to make a comprehensive and in-depth review on the current status of the light-harvesting capacities of the photo anode in DSSC.

Although recently reported DSSC with power conversion efficiency of over 11% has set new landmark in the field of DSSC research[2]. The presently achieved value is very low when compared to the predicted value of 32% for single junction cells[3]. For efficient working of a DSSC, it should have low charge recombination as well as high light harvesting capacity (LHE). Introduction of light scattering layer of large TiO_2 particles increase the LHE compromising the surface area for dye loading. 1D TiO_2 nanoparticles have the advantages of excellent electron properties as well as efficient light scattering abilities. However, because of its low surface area its dye loading capacities are affected. Thus, a photoanode material with high surface area, fast electron transport and good light scattering ability is the emergent need for high efficiency DSSC. Hence, recent research has been focussed on TiO_2 photo anode materials overcoming the limitations in 1D nanostructure by introducing nanocomposites and hierarchical structures in DSSC. Efforts to increase the efficiency focuses on improving the spectral absorbance range by changing the dye, increasing the mobility of holes and stability of the cell by replacing the liquid electrolyte with solid and semi-solid electrolytes, and improving the electron transport by varying the photo anode or by using morphologically different structures. The present chapter discusses in detail about the effect of electrolyte and effect of variation in the morphology as well as constituents of photo anode on the cell efficiency.

6.2 Configuration of DSSC

A typical DSSC contains several different components as shown in figure 6.1: a conducting glass substrate, a mesoporous semiconductor film, a sensitizer, an electrolyte with a redox couple and a counter electrode. To improve the overall efficiency, optimization of each of them is of great importance.

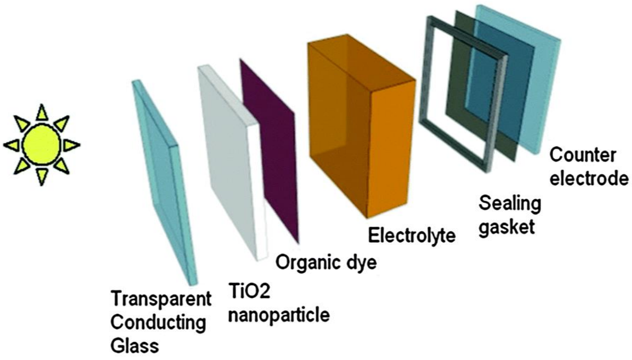

Figure 6.1: *Overview of the Dye sensitized Solar Cell (DSSC)*

6.3 Working of DSSC

The underlying principles of all photovoltaic devices while converting solar energy to electrical energy are:

- ☐ Radiation absorption with electronic excitation.
- ☐ Charge carrier separation.

The phenomenal mode of radiation absorption and charge carrier separation in DSSC differentiates it from other conventional p-n junction solar cells. In a conformist solar cell the driving principle relies on difference in the work function of the two electrodes, whereas the charge separation occurs at the depletion region built at the interface of p-n junction. In DSSC this happens in a distinguishingly unique way.

The working electrode of the cell consists of nanoporous wide band gap material on a transparent conducting glass (transparent conducting oxide) usually FTO/ITO. By the virtue of its nano size, semiconductor attains appreciably large surface area, helping it to effectively absorb the incident radiation. The dye which maximise the harvesting of light, would be adsorbed as a monolayer on the surface of TiO_2 nanoparticles and the sensitised film is intimately in contact with the electrolyte containing a redox couple (usually the iodide/tri-iodide couple (I^-/I^{3-})).The cell is sealed with another TCO electrode on to which thin layer of Pt is deposited. Figure 6.2 shows the basic schematic diagram of a typical nanoparticle based DSSC.

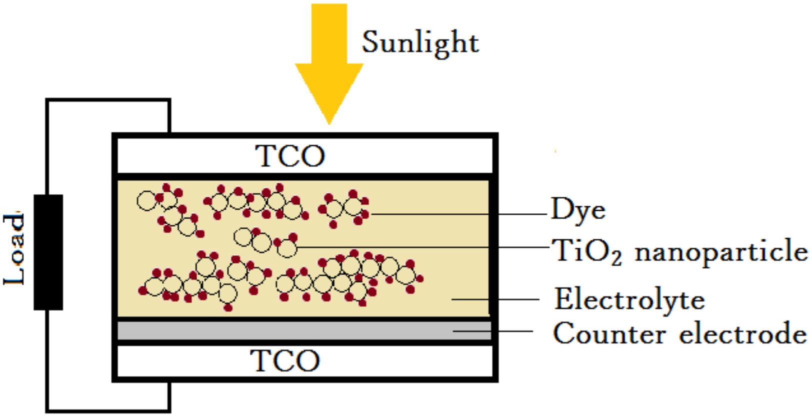

Figure 6.2: *Schematic of a nanoparticle-based DSSC structure*

The basic driving principle of a DSSC is the photo-excitation of the dye molecule and can be explained using a series of chemical reactions as given below:

$$TiO_2/Dye + h\upsilon \leftrightarrow TiO_2/Dye^*_{LUMO} \qquad (i)$$

$$Dye^*_{LUMO} + CB_{TiO2} \rightarrow TiO_2/Dye^+ + e_{CB}^- \qquad (ii)$$

$$Pt + [I_3]^- \rightarrow 3I^- \qquad (iii)$$

$$TiO_2/Dye^+ + 3I^- \rightarrow [I_3]^- + Dye \qquad (iv)$$

$$e_{CB}^- + Dye_{HOMO} \rightarrow Dye + CB_{TiO2} \qquad (v)$$

$$e_{CB}^- + [I_3]^- \rightarrow 3I^- + CB_{TiO2} \qquad (vi)$$

The incident light is absorbed by the dye and the electrons in the HOMO level of the dye are excited to its LUMO level by metal to ligand charge transfer (eq:i). Here the anchoring groups of the dye immobilize the dye adsorbed on TiO_2. From the excited state an electron can be injected into the conduction band (CB) of the semiconductor leaving the dye in its oxidized state (eq: ii). The injected electrons are then tranferred to the ITO electrode via diffusion through the disordered network of porous semiconductor. The extracted charge performs electrical work in the external circuit (eq:iii), before it reaches the counter electrode. The oxidized species in the dye are regenerated at the counter electrode by electron donation from the electrolyte, which is generally an organic solvent containing redox couple such as I^-/I^{3-} (eq:iv) and the circuit is closed by the regeneration of the dye by electron transfer from the electrolyte or hole-conductor. In the end, electric power is generated without undergoing permanent chemical transformation[45]. Unfortunately, in this process, some electrons can migrate from CB of TiO_2 to the HOMO level of the dye or electrolyte due to electron trapping effects resulting in electron recombination (eq:v & eq: vi). These processes can lower the cell performance. To achieve higher cell efficiency, the electron injection rate must be faster than the decay rate of the dye's excited state. Similarly the rate of reduction of the oxidized sensitizer (D^+) by the electron donor in the electrolyte (eq:iv), should be higher than the rate of back reaction of the injected electrons with the dye cation (eq:v), along with the rate of reaction of injected electrons with the electron acceptor in the electrolyte (eq:vi). Correspondingly the kinetics of the reaction at the counter electrode must be immediate enough to replenish the redox couple of the electrolyte instantaneously[6]. The oxidized dye must be regenerated by the redox couple at the speed of nanoseconds to kinetically compete with the metal oxide electrons for subsequent electron injection as well as to prevent the recombination, which depends on the energetics of metal oxide/dye/electrolyte interface[7].The above description has been pictorially represented in figure 6.3

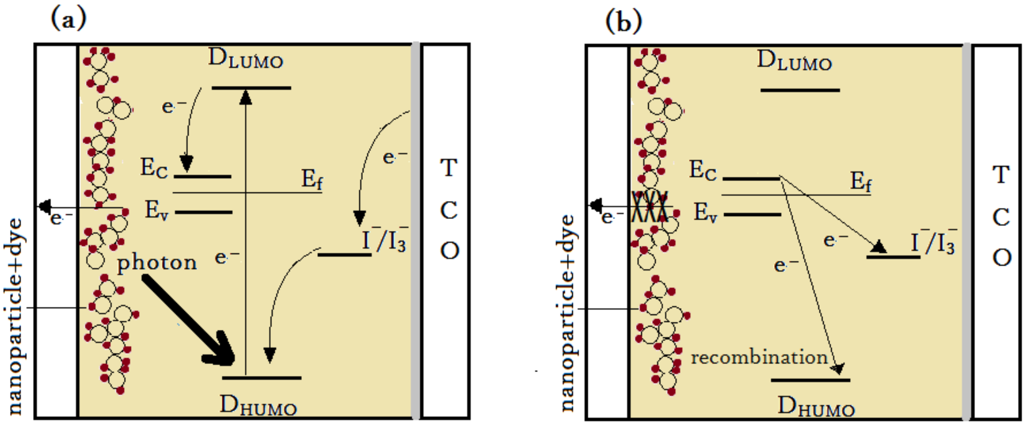

Figure 6.3: *(a) Schematics showing electron migration from dye molecules to the CB of TiO_2 (b) Possible recombination process.*

6.4 Constituents of DSSC

6.4.1 Working Electrode (TiO_2)

TiO_2 is the most favoured photo-electrode material because of its several advantages. TiO_2 does not absorb visible light radiation due to wide band gap and small absorption peak (388nm). Also, crystalline nano TiO_2 is easy to synthesise and can be sensitised using variety of dyes. TiO_2 when used in combination with Ruthenium (Ru) dye (described later) is thermodynamically well suited as the conduction band energy level of TiO_2 is ideally 0.2eV lower than that of Ru dye.

As mentioned in the previous chapters TiO_2 exists in three different forms: anatase, rutile and brookite. Both, anatase and rutile are well acclaimed in the evolution of DSSC research, however brookite is usually avoided as it is difficult to synthesis at low cost[8].Besides due to the advantage of simplicity in the synthesis of anatase phase, it is preferred over rutile phase mainly because:

- ☐ Absorption edge of anatase is at 388nm (Eg=3.2eV) and that of rutile is 413 nm (Eg=3 eV).Therefore some portion of the spectrum in the near UV region is absorbed by rutile unlike anatase. Stability of the cell is affected due to the generated holes by this absorption.
- ☐ The injected electrons to the conduction band of the semiconductor transfer more rapidly in anatase TiO_2 than in rutile phase due to the variation in the interparticle connectivity associated with the particle package density.

However, in spite of these factors rutile phase stills holds an eminent place in the DSSC research. N.G Park et.al. has studied and practically confirmed that rutile phase exhibited only 30% smaller J_{sc} than anatase and almost equal V_{oc}[9].

6.4.2 Sensitizer (Dye)

For efficient functioning of the cell, dyes used as sensitizer in the DSSC should meet various criteria [6,10,11,12,13,14,15,16]:

- ☐ Should harvest all photons below a threshold wavelength of 920 nm i.e., it should have broad absorption in the visible range.
- ☐ For efficient charge injection, the LUMO of the dye should be higher than the conduction band edge of the semiconductor .
- ☐ HUMO of the dye should be little below the redox potential of the electrolyte.
- ☐ Minimal deactivation of its excited state through the emission of heat and light.

- ☐ Strong irreversible adsorption to the semiconductor surface through suitable anchoring groups such as carboxylate, phosphonate or hydroxamate.
- ☐ Should be highly chemically stable such that efficiency of the cell is not affected with long exposure to intense illumination.

So far, variety of sensitizers including transition metal complexes and organic dyes have been employed in the study of DSSCs. The most efficient photo sensitizers studied hitherto are ruthenium (II) polypyridyl complexes particularly the prototype [cis-(dithiocyanato)-Ru-bis(2,20-bipyridine-4,40-dica- rboxylate)] complex (N3) and its doubly protonated tetrabuty- lammonium salt (N719)[17,18]. In these complexes, the thiocyanate ligands ensure fast regeneration of the photooxidized dye by the redox couple of the electrolyte while the two equivalent bipyridine ligands functionalized in their 4-4 positions by carboxylic groups ensure stable anchoring to the TiO_2 surface, allowing strong electronic coupling required for efficient excited-state charge injection[19]. Specifically, N719 dye has showed an efficiency of around 11%, reason for which could be the high open circuit potential which is so far unmatched by other dyes under comparable conditions[20]. The visible light absorption in Ru complex involves a metal to ligand charge (MLCT) transfer transition from the t_2g d orbitals localized on the Ru metal to π^* orbitals which are localised on the bypyridine ligand. The HOMO of the dye is localized near the Ru atom, whereas the LUMO is localized at the bipyridyl rings (Figure. 6.4b)[21]. Hence, photoexcitation leads to oxidation of Ru(II) to Ru(III) thus forming a bipyridine radical anion. The carboxylate substituents on the bipyridine ligands are covalently bound to the surface Ti(IV) ion of TiO_2, and the possible overlap of the accepting metal d orbitals of the TiO_2 conduction band and the N_3 carboxylate π^* orbitals may facilitate rapid electron transfer from the radical anion of bipyridine. These processes lead to ultrafast charge injection[22]. The molecular structure of N719 dye is shown in figure 6.4a, whereas 6.4b represents schematic representation of electron transfer in Ru dye and figure 6.4c represents its absorption spectra.

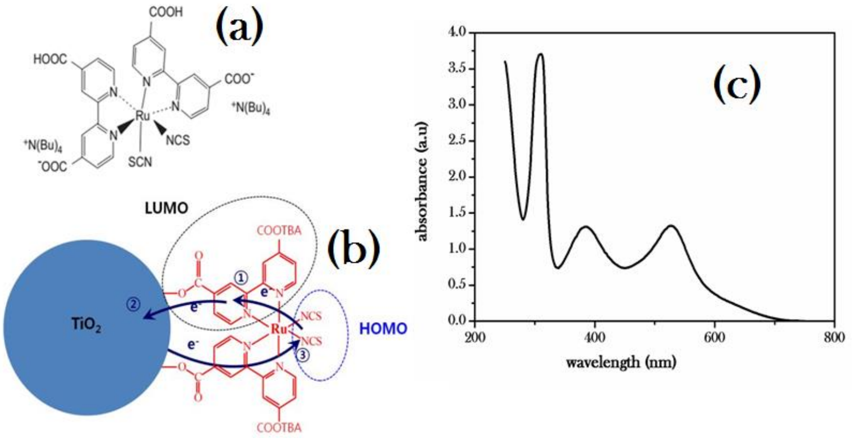

Figure 6.4: *(a) Molecular Structure of Ru N719 dye (b) Schematic representation of Electron transfer in Ru dye :- (1) MLCT excitation between dye and TiO_2 (2) Injection (3) Recombination (c) Absorption spectra of the Ru N719 dye.*

6.4.3 Electrolyte

An electrolyte is a solution that contains dissociated ions behaving as a conducting medium. Here, both types of positive and negative carriers are always present in equal concentrations. In DSSC the electrolyte transports the charge between the photo anode and the counter electrode during regeneration of the dye. It consists of the redox couple, solvent, and additives.

i. Redox Couple

Eg. Iodine/triodine, disulfide/thiolate

- The reversible potential for a redox couple should be negative when compared to the reversible potential for the dye but as positive as possible to avoid unnecessary loss of usable energy[23].
- Mostly redox couple in DSSCs is transported through diffusion. Hence high diffusion coefficient is desirable.
- Poor absorbance in the visible spectrum.
- Highly reversible redox couple to enhance electron transfer and avoid unwanted side reactions.
- Chemically inert.

ii. Solvent

Eg. acetonitrile, methoxyacetonitrile, methoxypropionitrile

- Must be liquid with low volatility at the operating temperatures.

- ☐ Should have low viscosity for the rapid diffusion of charge carriers.
- ☐ Redox couple should be soluble in the solvent.
- ☐ Should have a high dielectric constant.
- ☐ Must be stable against decomposition.

iii. Additives

- ☐ Additives such as different cations or 4-tert-butyl pyridine (TBP) can help by changing the conduction band level.

6.4.4 Counter Electrode

Counter electrode plays an important role in the electron transport and redox couple reduction. Efficient electrochemical activity is the prerequisite requirement for enhancing its performance. The open-circuit voltage is determined by the energetic difference between the Fermi-levels of the illuminated transparent conductor oxide (TCO) to the nano-crystalline TiO_2 film and the counter-electrode.

Platinum (Pt) is the most favoured counter electrode. Besides its high electro-catalytic activity it's another advantageous factor is increased light-reflection due to the mirror-effect of platinized TCO. Moreover, very low amount of Pt (less than $3\mu g/cm^2$) is sufficient to make it possible to be optically transparent and economical.

6.5 Effect of Electrolyte

The cell performance not only depends on the properties of the constituents individually but also on the interaction with each other, eg. the interaction between the redox electrolyte and a dye-adsorbed TiO_2 electrode. Under illumination, the maximum efficiency a cell can reach corresponds to the difference between the Fermi level of the nanoparticle and the redox potential of the electrolyte. The HOMO and LUMO of the dye should match well with the redox potential of the redox mediator in the electrolyte and the conduction band edge minimum of the semiconductor, respectively[24]. Here in the present study we have reviewed the performance of the cell based on various electrolytes including quasi static electrolytes.

6.5.1 Experimental

TiO_2 nanoparticles to be used as photoanode were prepared via very simple solvothermal processes involving Titanium tetrabutoxide (TTBO) and acetic acid (AcOH). The mixture solution of TTBO and AcOH was transferred into a 50 mL teflon-lined stainless steel autoclave and maintained at 120º–180ºC for 24h. Thus prepared powder samples were then washed and calcined at 500º C for 3h. Platinum was used as the counter electrode prepared from 7 mM solution of $H_2PtCl_6.6H_2O$ in 2-propanol coated on an ITO glass (Aldrich, 8-12Ω/sq). The N719 dye, purchased from Sigma Aldrich, was dissolved in dehydrated ethanol at a concentration of 0.5 mM. The ferrocene electrolyte was prepared from 0.05M ferrocenium hexafluorophosphate mixed with 0.1M ferrocene and 0.5M tert-butylpyridine in acetonitrile.0.3g of iodine and 1 g of KI were dissolved in acetonitrile for I_2 solution. 10% of PVA was dissolved with appropriate amount of iodine in tert-butyl pyridine for I_2-PVA electrolyte. The ITO coated counter electrode was placed on the top so that the conductive side of the counter electrode faced the dye adsorbed TiO_2 film.

Ultraviolet (UV)–visible absorption measurements of dye solutions were carried out using a Varian spectrophotometer. Current–voltage (J–V) characteristics of the cells were examined using a digital multimeter in the presence of a standard solar irradiation of 1000 W Xe lamp as the light source. To avoid the electrolyte being heated up by the infrared light, water column was used in front of the cell. Incident monochromatic photo-to-current conversion efficiency (IPCE) measurements were carried out using small band-pass filters to create monochromatic light. Input intensity was measured using a light meter (METRAVI 1332). In all the cases, input intensity was in the range of 1-10 klux.

6.5.2 Results and Discussions

Film thickness was measured using a digimatic micrometer and was found to be 0.033mm. XRD measurements were carried out on the TiO_2 nanoparticle sample and are shown in figure 6.5. All the peaks which are assignable to the anatase phase were clearly observed in the XRD patterns. The XRD peaks were intense and very well resolved, suggesting that the TiO_2 particles obtained have high crystallinity.

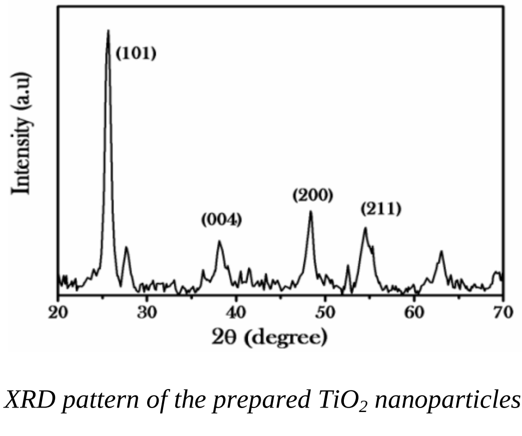

Figure 6.5: *XRD pattern of the prepared TiO_2 nanoparticles.*

Figure 6.6 and table 6.1 shows the short-circuit current density and efficiency obtained from the cells made of the titania nanoparticles with N719 dye, using three different electrolytes. It is found that the maximum efficiency is shown by the ferrocene electrolyte followed by the conventional iodine electrolyte.

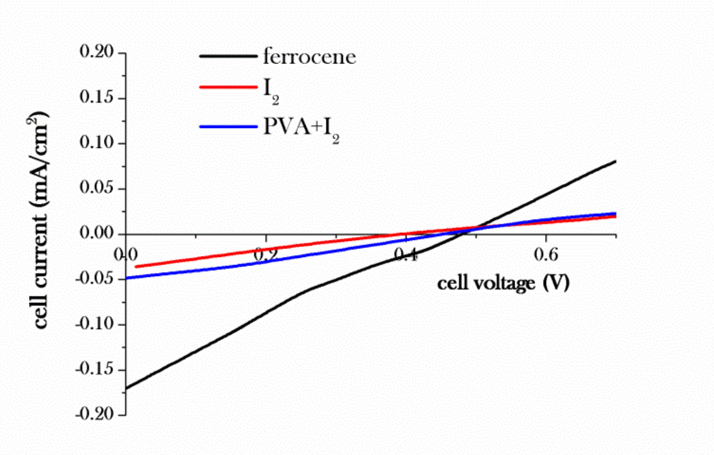

Figure 6.6: *J-V characteristics for N719 dye sensitised cell based on TiO_2 nanoparticles with various electrolytes.*

Electrolyte	**J_{sc} (mA/cm^2)**	**V_{oc} (V)**	**FF %**	**η %**
Ferrocene	0.171	0.481	20	2.82
I_2	0.036	0.389	23	1.2
PVA+I_2	0.050	0.464	24	0.52

Table 6.1: *Solar cell performance of DSSCs based on TiO_2 nanoparticles with various electrolytes.*

The efficiency, J_{sc} and V_{oc}, of the cell are highest for ferrocene which can be due to the enlarged energy level difference between the redox potential of the Fe^{2+}/Fe^{3+} and TiO_2 conduction and this can be pictorially represented as in figure 6.7. This difference solely depends on the nature of the redox couple, because the increase is independent of the dye structure[24]. It is generally believed that electrolytes containing different components have a strong effect on DSSC performance. In general, the photocurrent density of DSSC using the liquid electrolyte is proportional to the ionic conductivity of the electrolyte. In DSSCs, the dye is excited by the absorbing photon and then forms oxidized dye after injection of the electron into the conducting band (CB) of TiO_2. The oxidized dye then accepts electron from redox couple of the electrolyte and hence is regenerated. Therefore, to be effectively reduced by the electrolyte the HOMO level of the dye must be more positive than the reducing potential of the redox couple of the electrolyte.

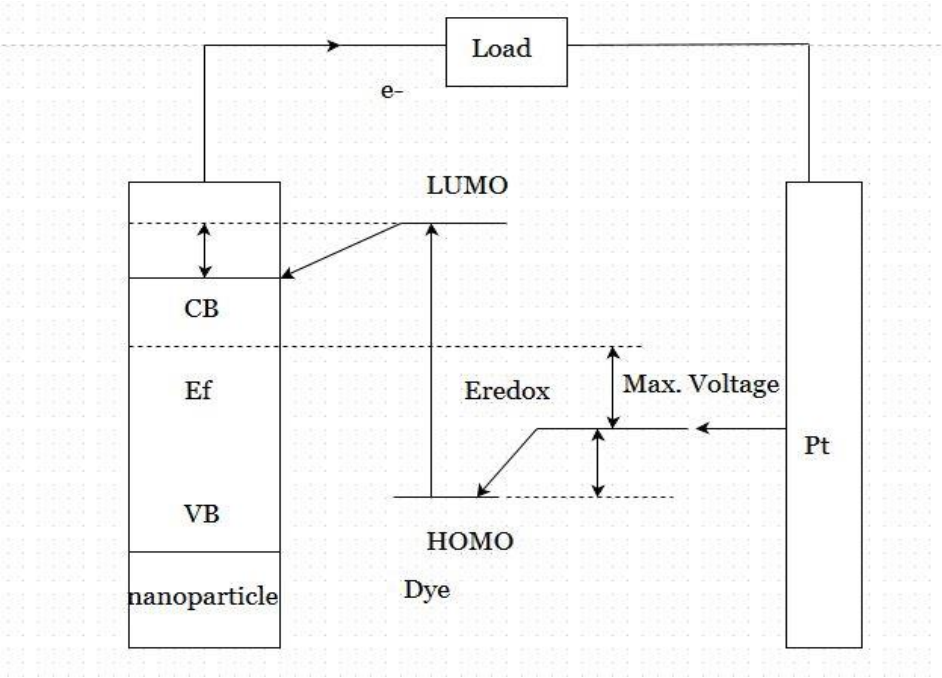

Figure 6.7: *Schematic diagram for various energy levels in a dye sensitised solar cell.*

Based on the above studies we can infer that ferrocene is the best of the three electrolytes used. Hence, hereafter we have evaluated the performance of the DSSC by varying the photoanode with ferrocence as the standard electrolyte keeping other constituents and condition same.

6.6 Effect of TiO_2 Morphology

It has been studied that electron transport through the nanoparticle film occurs through diffusion or hopping between different trap states[25]. Electron diffusion through the nanoparticle film should be faster than the electron recombination with oxidized dyes on the TiO_2 surface. Fabrication of one-dimensional TiO_2 related DSSCs, such as nanorod (NR) DSSCs and nanowire (NW)/ nanoparticle (NP) composite DSSCs, have recently been reported for improving the electron transport rate in anodes[26,27]. Other multidimensional structures have also been investigated due to their increased light scattering ability associated with their large surface area enabling efficient light harvesting that in turn maximizes the amount of photogenerated charge. Dependence of cell performance on the anode morphology has been investigated by many groups[28].

6.6.1 Experimental

Different morphological structures of TiO_2 namely nanorods, nanosheets, nanoflowers, and nanospheres were synthesised as described in the chapter 4 [29,30,31,32]. Nanotrees were synthesised as reported by Liu and Aydi[33]. During the synthesis, 30 mL of deionized water was mixed with 30 mL of concentrated hydrochloric acid in a Teflon-lined stainless steel autoclave. The resultant mixture was stirred at ambient conditions for 5 min followed by the addition of 1 mL of titanium butoxide. After stirring for another 5 min, one piece of ultrasonically cleaned ITO substrate, was placed at an angle against the wall of the Teflon-liner with the conducting side facing down. The hydrothermal synthesis was conducted at 80°-220°C for 24 h in an electric oven. After synthesis, the autoclave was cooled to room temperature under flowing water. The ITO substrate was taken out, rinsed extensively with deionized water and was allowed to dry in ambient air. Cell fabrication and instrumental details used is same as described earlier.

6.6.2 Results and Discussions

Figure 6.8 represents the SEM analysis of the different nanostructured TiO_2. Figure 6.9 represents absorption spectra of the different nanostructured TiO_2. It was observed that the TiO_2 3D nanoflower showed the highest absorption in the UV region among the samples. It could be due to the fact that absorption is significantly dependent on the morphological structure of the sample. Film thickness was measured using a digimatic micrometer and was found to be 0.033mm. XRD measurements were carried out for all the samples and the observed patterns are shown in figure 6.10. All the peaks assignable to the anatase phase were clearly observed in the XRD patterns. The XRD peaks were intense and very well resolved, suggesting that the TiO_2 particles obtained have high crystallinity.

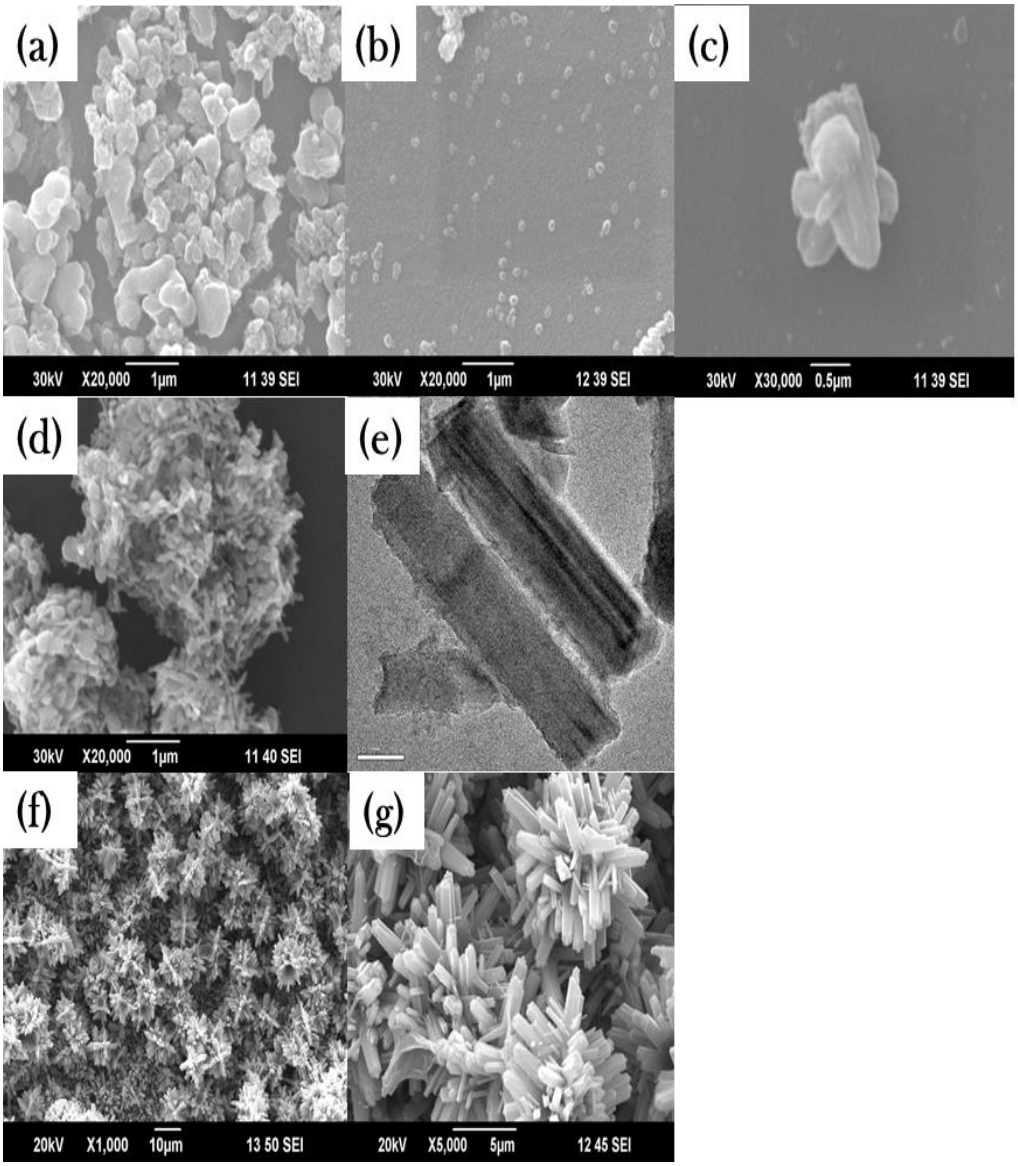

Figure 6.8: *SEM images of different nanostructured* TiO_2. *(a) nanosheet (b) nanosphere (c) nanoflower (d) nanowire (e) TEM images of nanowire (f) nanotree (g) magnified image of nanotree.*

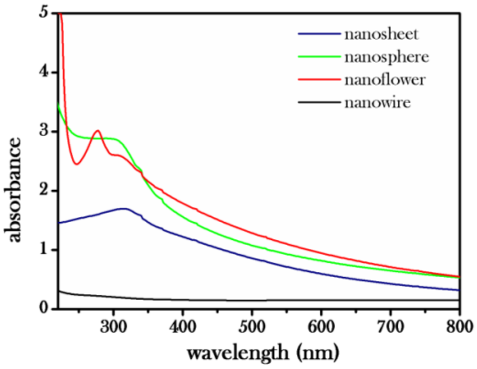

Figure 6.9: *Absorption spectra of TiO_2 nanostructures.*

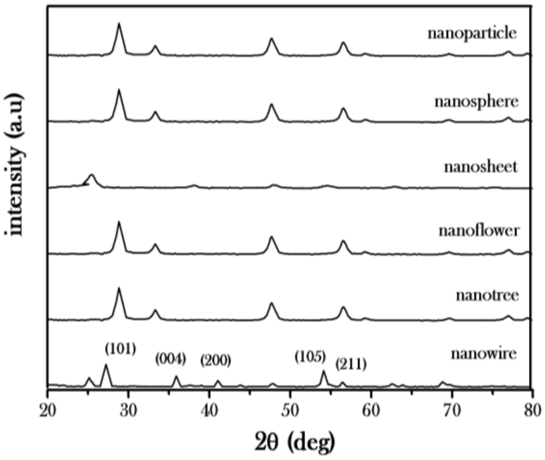

Figure 6.10: *XRD pattern of TiO_2 nanoparticles and TiO_2 nanostructures.*

The photovoltaic characteristics of the DSSCs constructed with different TiO_2 morphology are represented in figure 6.11a. The short-circuit current density (J_{sc}), the open-circuit voltage (V_{oc}), the fill factor (FF) and the overall power conversion efficiency (η) deduced from the J-V curves are summarized in table 6.2. It is observed that the efficiency of the cells increases in the following order, **nanosheet <nanosphere< nanoflower<nanowire <nanotree**. Increase in the surface area leads to enhancement in the dye loading leading to increase in the J_{sc} and hence J_{sc} follows the order nanowire <nanosheet <nanosphere< nanoflower< nanotree. Alternatively V_{oc} follows the order of probability of charge recombination at the interface between the nanoparticle and the electrolyte. But as expected, nanowire doesn't have the lowest efficiency due to the lowest surface area among the group. This could be due to the fact that nanowire offers the direct conduction pathway for the rapid collection of photogenerated electrons between the two electrodes thereby reducing the possibility of charge recombination during interparticle percolation thereby boosting V_{oc}.

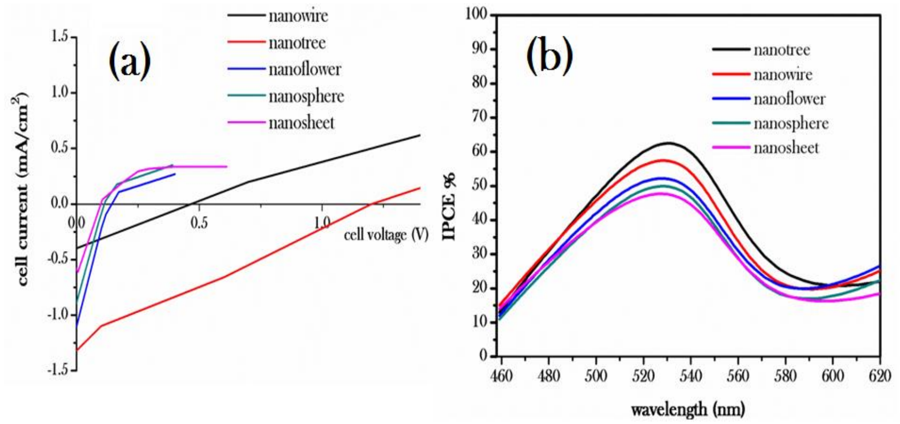

Figure 6.11: *(a) J-V characteristics for N719 dye sensitised DSSCs with ferrocene electrolyte with various nanostructured* TiO_2 *photoanode (b) IPCE characteristics of the DSSC with various nanostructured* TiO_2 *as photoanode.*

It is observed that nanotrees shows better photovoltaic performance than nanowires. In the case of DSSC with nanowires, they are randomly oriented as visible in figure 6.8d. This kind of random orientation of nanowires can actually pose way for electrical shorting between themselves. The ensuing electrical shorting might have compensated the effect of scattering between these randomly arranged nanowires leading to fall in photovoltaic parameters. For nanowires, instead of effective chemical bonding, there occurs formation of Ti^{4+}/ Ru dye complex in the gaps between them due to insufficient internal surface area leading to excess dye loading. This Ti^{4+}/ Ru dye complex absorbs the incident light but does not effectively inject the photogenerated electrons into the TiO_2 photoanode. This complex could eventually agglomerate and can act as a thick barrier for effective electron injection. The recombination rate between the charge carriers and dye/electrolyte also plays a very important role in determining the efficiency of a cell. 1D nanostructures offers the advantage of providing direct conduction pathway between the electrodes. According to Jiang et al, vertical 1 D structure along with providing such a facile transport mechanism can also pose a serious threat to the light dye interaction process[34]. There are chances of some photons to fall in between the vertical nanowires and hence all the input light cannot not be productively utilised. But in the case of our nanotrees the nanobranches spreading out 3D in almost all directions can effectively absorb the maximum number of incident photons. These nanobranches collect the photons thereby transferring it to the vertical 1 D skeleton. Hence it provides maximum internal surface area without sacrificing the merits of 1D smooth transport of charge carriers. The high density, multi branched hierarchical TiO_2 nanotrees can enhance the surface area for higher dye loading and light harvesting thereby increasing J_{sc}. By providing a direct conduction pathway along the crystalline TiO_2 branches probability of charge recombination also decrements thus boosting V_{oc}. These combined effects significantly enhance the power efficiency of DSSC.

In the case of nanotrees it is possible that along with the direct conduction pathway, its intertwined petal- like structures allow multiple reflections and scattering of light which eventually increases the optical path of the incident light enhancing the density of photogenerated electrons,leading to its improved photovoltaic performance. Thus it can be concluded that nanotrees offer both the advantages of 1D crystalline structure as well as large surface area similar to multiscale hierarchical configurations.

Photoanode	**J_{sc} (mA/cm^2)**	**V_{oc} (V)**	**FF %**	**η %**
TiO_2	0.171	0.485	20	2.82
TiO_2 nanowire	0.384	0.500	18	7.5
TiO_2 nanotree	1.309	1.252	22	10.2
TiO_2 nanosheet	0.464	0.102	32	2.87
TiO_2 nanosphere	0.864	0.118	21	3.58
TiO_2 nanoflower	1.081	0.150	22	5.37

Table 6.2: *Solar cell performance parameters for DSSCs with various TiO_2 based photoanodes.*

Figure 6.11b represents the IPCE curve of the nanostructures. The IPCE characteristics follow the J-V characteristics of the DSSC. The maximum IPCE value of 63% is shown with nanotree as photo anode. Figure 6.12 represents the comparison of stabilities for cells for a period of 3 weeks. Efficiency of the cell does not undergo noticeable change over a period of 3 weeks.

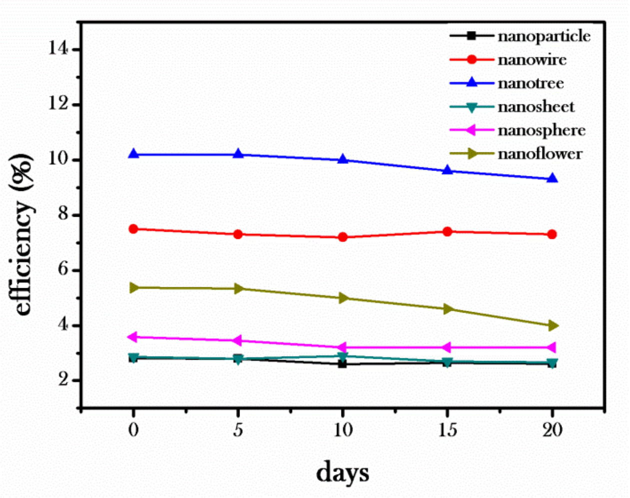

Figure 6.12: *Comparison of stabilities for cells for a period of 3 weeks.*

6.7 Effect of Doping

The energy state of the photo anode also plays a very crucial role in determining the efficiency of the cell. Doping of different materials either introduces additional energy states or minimises the defect states of TiO_2 which eventually alters the electron transport of the TiO_2. In recent years great interest has been devoted to study the effect of doping in TiO_2 for DSSC performance.

6.7.1 Experimental

TiO_2 based nanocomposites viz, TiO_2-SiO_2, TiO_2-CeO_2, TiN were synthesised as described in the chapter 5. Cell fabrication and instrumental details used is analogous to as described earlier.

6.7.2 Results and Discussions

Film thickness was limited to 0.033mm by using a digimatic micrometre. XRD measurements were carried out for all the samples and are shown in figure 6.13. All the peaks assignable to the anatase phase were clearly observed in the XRD patterns.

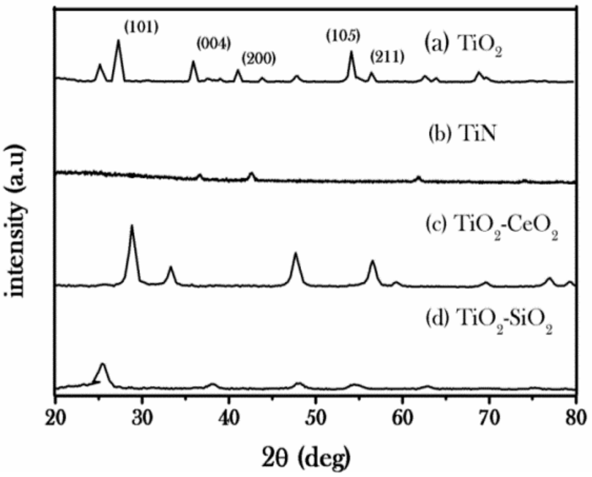

Figure 6.13: *XRD pattern of nanoparticles (a) TiO_2 (b) TiN (c) TiO_2-CeO_2 (d) TiO_2-SiO_2.*

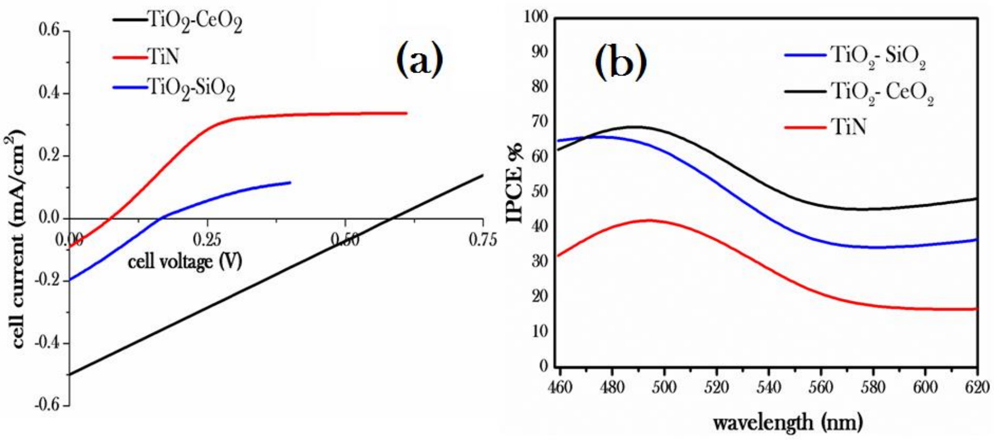

Figure 6.14: *(a) J-V characteristics for N719 dye sensitised DSScs with ferrocene electrolyte with various TiO_2 nanocomposites as photoanode (b) IPCE characteristics of the DSSC with various TiO_2 nanocomposites as photoanode.*

Figure 6.14a and table 6.3 gives the photocurrent voltage (J-V) characteristics of the DSSCs with photoanodes using TiO_2 nanocomposites viz; TiO_2-CeO_2, TiO_2-SiO_2, TiO_2-N (TiN). Among the three studied nanocomposites, TiO_2-CeO_2 showed superior photovoltaic performance than all other nanocomposites followed by TiO_2-SiO_2 and TiN.

Photoanode	J_{sc} (mA/cm^2)	V_{oc} (V)	FF %	η %
TiO_2	0.171	0.485	20	2.82
TiO_2-SiO_2	0.183	0.165	23	7.68
TiO_2-CeO_2	0.507	0.578	32	12.31
TiN	0.0907	0.078	2	0.53

Table 6.3: *Solar cell performance for DSSCs with various* TiO_2 *based photo anodes.*

In the case of TiO_2-CeO_2 nanocomposites Ce^{3+} and Ce^{4+} oxidised states were present as confirmed from the absorption spectra of the TiO_2-CeO_2 nanocomposites [35,36]. Figure 6.15 depicts the absorption spectra of the TiO_2-CeO_2 nanocomposites. From the figure it can be concluded that the Ce ions may exist either on the grain boundary or on the surface of the TiO_2 nanoparticle. As verified earlier, in chapter 5 Ce with partially filled f orbitals endows TiO_2 with special properties. It is verified that Ce doping positively moves the conduction band edge, and the Ce^{4+} effectively captures the electrons, which can improve the electron injection from the excited dye molecules. Figure 6.16 shows the positive movement of TiO_2 conduction band in TiO_2-CeO_2 nanocomposites.

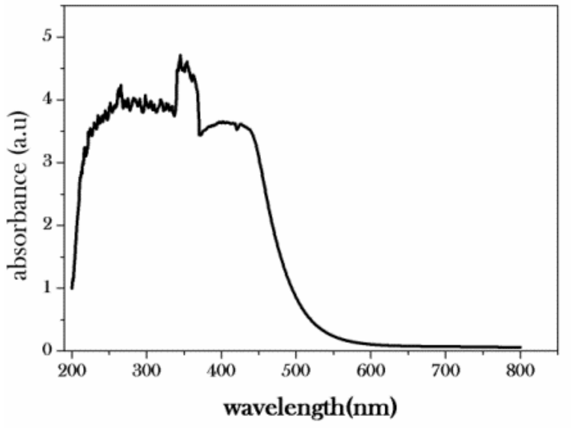

Figure 6.15: *Absorption spectra of* TiO_2-CeO_2 *nanocomposites.*

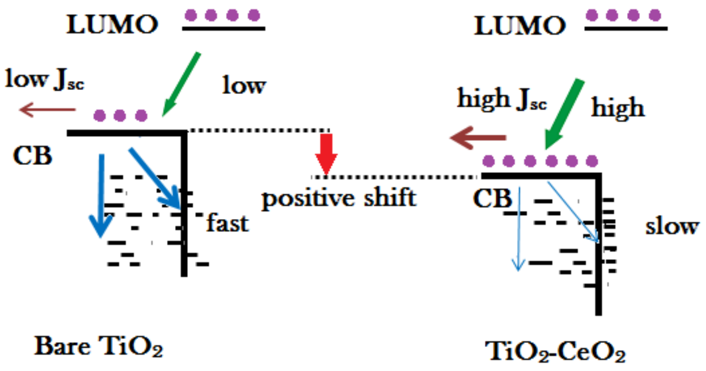

Figure 6.16: *Positive movement of TiO_2 conduction band in TiO_2-CeO_2 nanocomposites increases the driving force for electron injection (increases in J_{sc}) and reduces the charge recombination.*

So both the positive movement of the conduction band and the increased electron concentration in the photoanode contribute to the change of quasi-Fermi level/V_{oc}. It introduces impurity band states near the conduction band edge reducing the optical band gap. During illumination, Ce^{4+} traps the electrons thereby reducing it to Ce^{3+}. Hence Ce^{4+} acts as trap states attracting the injected electrons from the dye and blocking the interface recombination that makes the fill factor (FF) and hence efficiency to increase. For the cell with TiO_2-SiO_2 as photoanode, SiO_2 acts as a wide band gap insulating layer between the photoexcited electrons and the redox electrolyte ions reducing the probability for charge recombination between semiconductor and electrolyte .Moreover, the introduction of SiO_2 leads to more amount of micro/meso-pores which cannot be penetrated by electrolyte because of surface tension, which further reduces the chances of charge carrier recombination. In the case of TiN , efficiency of the DSSC is very less as implied from its J-V characteristics. Here the J_{sc} of the cell is very low indicating the poor adsorption of the dye on to the nanoparticle which in turn can be due to the low surface area of the nanoparticle available for dye loading. TiN is usually black in colour and here when applied on the ITO it appeared as a dark layer. Thus it is probable that it posed adverse effects to the dye molecules to harvest the sunlight effectively. TiN is considered to be very good conducting material[37] and hence it was expected to show much better performance. So, in the present case it can be concluded that its exceptional conducting property was overcome by the unfavourable effects of poor dye adsorption

Figure 6.14b shows the IPCE characteristics of the DSSCs with various nanocomposites. Among them DSSC with TiO_2-CeO_2 shows the highest IPCE value of 70%. Figure 6.17 represents the comparison of stabilities for cells for a period of 3 weeks. It can be inferred that the efficiency of the cell does not undergo noticeable change over a period of 3 weeks.

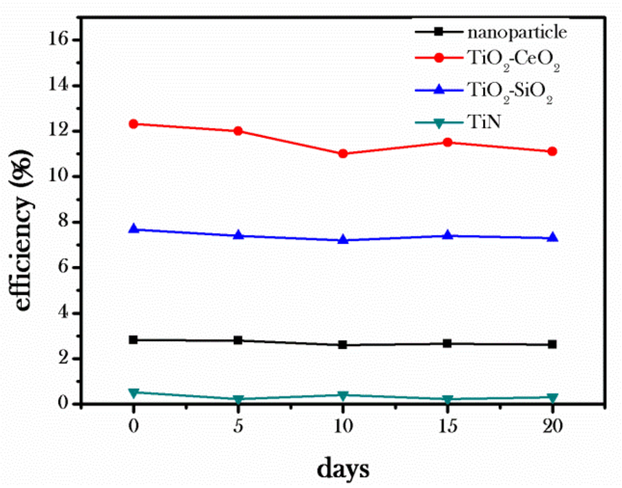

Figure 6.17: *Comparison of stabilities for cells for a period of 3 weeks.*

6.8 Conclusions

- ❑ We studied the performance of the DSSC cell based on titania nanoparticles with N719 dye, using three different electrolytes. It is found that the maximum efficiency is shown by the ferrocene electrolyte followed by the conventional iodine electrolyte. The efficiency, J_{sc} and V_{oc} , of the cell is highest for ferrocene which can be due to the enlarged energy level difference between the redox potential of the $Fe^{2+}/Fe^{3+}$and TiO_2 conduction band. PVA based electrolyte exhibited the least performance due to the poor mobility of charge carriers as well as poor wetting ability. Its incomplete penetration into the semiconductor to regenerate the dye plays a negative role. Ferrocene was adjudged as the best of the three electrolytes used.

- ❑ To further improve the performance of DSSCs based on the N719 dye standardised with ferrocence electrolyte, the photovoltaic parameters controlling the device performance were assessed using different TiO_2 nanostructures as photoanode. During the experiment it was observed that J_{sc} and V_{oc} showed enhancement for nanotree compared to all others due to improved light harvesting and charge collection efficiency. Multi-scattering phenomenon in nanotrees lead to increased optical path of the incident light enhancing the density of photogenerated electrons, which enhances its photovoltaic performance. Hence it was proved that the hierarchical nanostructures are the key to the realization of high efficiency DSSCs.

- ☐ To evaluate the dependence of performance of the cell on photoanode, its constituent was varied by using different TiO_2 based nanocomposites viz TiO_2-CeO_2, TiO_2-SiO_2, TiO_2-N (TiN). During the experiment with cells employing TiO_2 nanocomposites it was proved that doping of cerium introduced additional energy states in the band gap, influencing the light absorbance and the electron transport of the TiO_2 leading it to show better photovoltaic performance compared to other nanocomposites under study namely TiO_2–SiO_2 and TiN.

6.9 References

---

[1] B. O'Regan, M. Grätzel. (1991) "A Low-Cost, High-Efficiency Solar Cell Based on Dye-sensitized Colloidal TiO_2 Films." *Nature,* 353, 737

[2] Grätzel, Michael. (2005) "Solar energy conversion by dye-sensitized photovoltaic cells". *Inorg. Chem.* 44(20), 6841-6851.

[3] J Frank, Arthur, Nikos Kopidakis, and Jao van de Lagemaat. (2004) "Electrons in nanostructured TiO_2 solar cells: transport, recombination and photovoltaic properties." *Coord. Chem. Rev*. 248(13),1165-1179.

[4] Nazeeruddin, M. K., Zakeeruddin, S. M., Lagref, J. J., Liska, P., Comte, P., Barolo, C., ... & Grätzel, M. (2004). "Stepwise assembly of amphiphilic ruthenium sensitizers and their applications in dye-sensitized solar cell". *Coord. Chem. Rev*, 248(13), 1317-1328.

[5] Grätzel, M. (2004). Corrigendum to "Conversion of sunlight to electric power by nanocrystalline dye-sensitized solar cells".[J. Photochem. Photobiol. A: Chem. 164 (2004) 3–14. *J. Photochem. Photobiol. A* , 168(3), 235.

[6] Kalaignan, G. P., & Kang, Y. S. (2006). "A review on mass transport in dye-sensitized nanocrystalline solar cells". *J. Photochem. Photobiol. C: Photochem. Rev.* , 7(1), 17-22.

[7] V. Thavasi, V. Renugopalakrishnan, R. Jose, S. Ramakrishna (2009). "Controlled electron injection and transport at materials interfaces in dye sensitized solar cells". *Mater. Sci. Eng.*, R,63,81–99.

[8] Kalyanasundaram, K., & Grätzel, M. (1998). "Applications of functionalized transition metal complexes in photonic and optoelectronic devices". *Coord. Chem. Rev.*, 177(1), 347-414.

[9] Park, N. G., Van de Lagemaat, J., & Frank, A. J. (2000). " Comparison of dye-sensitized rutile-and anatase-based TiO_2 solar cells". *J. Phys. Chem. B*, 104(38), 8989-8994.

[10] A.F. Haught. (1984) "Physics consideration of solar energy conversion" *ASME J. Solar Energy Eng.*, 106, 3–15

---

[11] Winter, C. J., & Sizmann, R. L. (1991). “Solar power plants: fundamentals, technology, systems, economics”. *L. L. Vant-Hull (Ed.). New York: Springer-Verlag*.

[12] De Vos, A. (2008). “Thermodynamics of solar energy conversion”. *Berlin: Wiley-Vch*.

[13] Luque, A., & Araújo, G. L. (1990). “Physical limitations to photovoltaic energy conversion”. *Institute of Physics Publishing.*

[14] Baruch, P. (1985). “A two-level system as a model for a photovoltaic solar cell”. *J. Appl. Phys*., 57(4), 1347-1355.

[15] M A Green.(1982) , “Solar Cells”, *Prentice-Hall,New Jersey*,89.

[16] Hagfeldt, A., & Grätzel, M. (2000). “Molecular photovoltaics”. *Acc. Chem. Res*., 33(5), 269-277.

[17] Nazeeruddin, M. K., Kay, A., Rodicio, I., Humphry-Baker, R., Müller, E., Liska, P & Grätzel, M. (1993). “Conversion of light to electricity by cis-X2bis (2, 2'-bipyridyl-4, 4'-dicarboxylate) ruthenium (II) charge-transfer sensitizers (X= Cl-, Br-, I-, CN-, and SCN-) on nanocrystalline titanium dioxide electrodes”. *J. Am. Chem. Soc.*, 115(14), 6382-6390.

[18] Nazeeruddin, M. K., De Angelis, F., Fantacci, S., Selloni, A., Viscardi, G., Liska, P., ... & Grätzel, M. (2005). “Combined experimental and DFT-TDDFT computational study of photoelectrochemical cell ruthenium sensitizers”. *J. Am. Chem. Soc*., 127(48), 16835-16847.

[19] De Angelis, F., Fantacci, S., Mosconi, E., Nazeeruddin, M. K., & Grätzel, M. (2011). “Absorption spectra and excited state energy levels of the N719 dye on TiO_2 in dye-sensitized solar cell models”. *J. Phys. Chem. C*, 115(17), 8825-8831.

[20] De Angelis, F.; Fantacci, S.; Selloni, A.; Graetzel, M.; Nazeeruddin, M. K. (2007) “Influence of the Sensitizer Adsorption Mode on the Open-Circuit Potential of Dye-Sensitized Solar Cells”. *Nano Lett.*, 7, 3189–3195.

[21] Yun, Ho Gyeong.2011. “High efficiency photovoltaic cells based on metal substrate and nano structured TiO_2 films”. *Phd Thesis*, KAIST.

[22] Robertson, N. (2006). “Optimizing Dyes for Dye-Sensitized Solar Cells”. *Angew. Chem. Int. Ed*., 45(15), 2338-2345.

[23] G. Wolfbauer, A. M. Bond, J. C. Eklund, and D. R. MacFarlane, (2001) “A channel flow cell system specifically designed to test the efficiency of redox shuttles in dye sensitized solar cells” *Sol. Energ. Mat. Sol. Cells* 70, 85-101.

[24] Daeneke T, Kwon T H, Holmes A B, Duffy NW, Bach U and Spiccia L (2011), “High-efficiency dye-sensitized solar cells with ferrocene-based electrolytes” *Nat. Chem.* 3 211–5.

[25] Baxter, Jason B., and Eray S. Aydil. (2005) “Nanowire-based dye-sensitized solar cells.” *Appl. Phys. Lett.* 86,(5), 053114-053114.

---

[26] Lee, Chang Hyo, Seung Woo Rhee, and Hyung Wook Choi. (2012) “Preparation of TiO_2 nanotube/nanoparticle composite particles and their applications in dye-sensitized solar cells.” *Nanoscale Res. Lett.*, 7(1), 1-5.

[27] Wu, Jih-Jen, et al. (2008) “Performance and electron transport properties of TiO_2 nanocomposite dye-sensitized solar cells”. *Nanotechnology* 19(10),105702.

[28] Chae, Jinho, and Misook Kang. (2011) “Cubic titanium dioxide photoanode for dye-sensitized solar cells”. *J. Power Sources* 196(8),4143-4151.

[29] Tan, Bing, and Yiying Wu. (2006) “Dye-sensitized solar cells based on anatase TiO_2 nanoparticle/nanowire composites”. *J. Phys. Chem. B* 110(32),15932-15938.

[30] Yang, Xiao Hua, Zhen Li, Gang Liu, Jun Xing, Chenghua Sun, Hua Gui Yang, and Chunzhong Li. (2011) “Ultra-thin anatase TiO_2 nanosheets dominated with {001} facets: thickness-controlled synthesis, growth mechanism and water-splitting properties”. *Cryst. Eng. Comm.*, 13(5), 1378-1383.

[31] Hu, Yongxing, Jianping Ge, Yugang Sun, Tierui Zhang, and Yadong Yin. (2007) “A self-templated approach to TiO_2 microcapsules”. *Nano Lett.*,7(6),1832-1836.

[32] Tian, Guohui, Yajie Chen, Wei Zhou, Kai Pan, Chungui Tian, Xu-ri Huang, and Honggang Fu. (2011) “3D hierarchical flower-like TiO_2 nanostructure: morphology control and its photocatalytic property”. *Cryst. Eng. Comm* 13,(8), 2994-3000.

[33] Liu, Bin, and Eray S. Aydil. (2009) “Growth of oriented single-crystalline rutile TiO_2 nanorods on transparent conducting substrates for dye-sensitized solar cells”. *J. Am. Chem. Soc.*, 131(11), 3985-3990.

[34] Jiang, C. Y., X. W. Sun, G. Q. Lo, D. L. Kwong, and J. X. Wang. (2007) “Improved dye-sensitized solar cells with a ZnO-nanoflower photoanode”. *Appl. Phys. Lett.* 90(26), 263501-263501.

[35] Rao GR, Sahu HR. (2001) “ XRD and UV–Vis diffuse reflectance analysis of CeO_2–ZrO_2 solid solutions synthesized bycombustion method”. *Proc. Indian Acad. Sci. (Chem Sci)*; 113,651–8.

[36] Bensalem A, Bozon-Verduraz F, Delamar M, Bugli G. (1995) “Preparation and characterization of highly dispersed silica supported ceria”. *Appl. Catal. A*, 121,81–93.

[37] S.T. Myung, M. Kumagai, R. Asaishi, Y.K. Sun, H. Yashiro, (2008) “Nanoparticle TiN-coated type 310S stainless steel as bipolar plates for polymer electrolyte membrane fuel cell” . *Electrochem. Commun.*10 (3),480–484.

Chapter 7

General Conclusions and Future Prospects

Abstract

This chapter deals with the summary of the work presented in this thesis along with an outline of the future prospects.

7.1 Conclusions

From the work detailed in the previous chapters, following general conclusions can be drawn:

- ☐ TiO_2 nanoparticles were synthesised using the sol–gel method. The obtained nanoparticles were subjected to thermal treatment to obtain the anatase and rutile phase of TiO_2. The optical absorbance spectra showed a relative red shift with respect to the amorphous phase signifying an increase in size of the nanoparticles with annealing temperature. The fluorescence emission spectra studies carried out showed four peaks, which were found to be generated from excitonic as well as surface state transitions. Nonlinear optical studies using nanosecond laser displayed Reverse Saturable Absorption (RSA) which is explained through two photon absorption followed by the dominant role played by excitons. The optical limiting threshold was calculated for all the three phases and results displayed that anatase showed better limiting capability than the amorphous or rutile phase of TiO_2.

- ☐ Different TiO_2 nanostructures were synthesised namely, nanowires, nanosheets, nanospheres and nanoflowers. Linear and nonlinear optical properties were studied using optical absorption, fluorescence spectroscopy, and open as well as closed aperture Z-scan technique. The nonlinear properties of the nanostructured suspensions were found to be shape dependent. Among the different structures, nanoflower showed the highest nonlinear absorption and nonlinear refraction. This phenomenon is explained by the fact that nanoflower due to its peculiar structure has highest surface-to-volume ratio and also its intertwined petal-like structure causes repeated reflection and absorption causing thermal nonlinearity to take the lead. The optical limiting thresholds of the samples were also investigated and were found to decrease with the increase in the effective light matter interaction area of the sample.

- ☐ Different TiO_2 based nanocomposites viz, TiO_2-SiO_2, TiO_2-CeO_2, TiO_2-N (TiN), TiN-PVA were synthesised using sol gel technique. The nanocomposites showed enhanced nonlinear optical properties compared to pure TiO_2. For TiO_2-SiO_2, surface states and weak dielectric confinement of TiO_2 nanoparticles created by SiO_2 matrix lead to the enhancement of the optical nonlinear properties. In TiO_2-CeO_2, Ce 4f and oxygen defect levels smeared out to the forbidden energy gap of the host introducing new energy levels that made the optical properties of the nanocomposites to stand out from that of the host. The large third-order nonlinear optical susceptibility of the TiN nanoparticles is due to the surface plasmon resonance. The enhancement of nonlinear optical response makes it a promising material in photonics applications. The optical constants of TiN/PVA nanocomposite thin films were determined by simple calculations using only the absorption spectra. Simultaneously, the nonlinear parameters were also calculated using Z-scan Experiment. Z-scan results gave much larger values of nonlinear optical parameters and this discrepancy in values can be attributed to the role of SPR of TiN nanoparticles which lie close to the irradiated laser beam wavelength of 532 nm.

- ☐ We studied the performance of the DSSCs based on various electrolytes. To further improve the performance of DSSCs based on the N719 dye standardised with ferrocene electrolyte the photovoltaic parameters controlling the device performance were assessed using different TiO_2 nanostructures and TiO_2 based nanocomposites as photoanode. It was evidenced that the hierarchical nanostructures are the key to the realization of high efficiency DSSCs with nanotree as photoanode. Cells employing TiO_2 nanocomposites showed that introduction of cerium introduced energy states in the band gap, influencing the light absorbance and the electron transport of the TiO_2 leading it to show better photovoltaic performance.

7.2 Future Prospects

Following are the suggested studies which can be undertaken in the future:

- ☐ TiN due to its various favourable properties as discussed in previous chapters, is continuously gaining widespread scientific attention. As for noble metals morphology variations leads to shift in Surface Plasmon Resonance (SPR) and hence distinction in its related optical properties, similar studies can be performed for TiN as well[12]. Such kind of study will be first of its own.

- ☐ DSSCs have typically been prepared by sandwiching two electrodes, where the photoanode is composed of dye-coated nanocrystalline TiO_2 film deposited on a transparent conducting oxide (TCO), such as ITO/FTO(Indium/fluorine-doped thin oxide), and the positive electrode consists of nanoparticulate Pt on a ITO glass. TCO acts as a charge collector in DSSCs. An antireflection layer may also be required to improve the light harvesting efficiency due to the fact that such TCO coated glass reduces transmittance by 10–15%. Recently, a TCO-less DSSC structure has been proposed to utilize more incoming visible light, where plain glass was used instead of the TCO-coated glass[3,4]. The TiO_2 film was formed on a glass substrate without FTO, followed by deposition of Ti metal to be used as the charge collector. This FTO-less structure with a metal Ti back contact demonstrated a conversion efficiency of about 3.6%[1]. All the published reports have used only Ti metal as a charge collecting material, mainly due to the Ohmic contact requirement at the TiO_2/metal junction. The conductivity of Ti and TiN is reported as $(1.1{\sim}2.4) \times 10^4\ \Omega^{-1}\ cm^{-1}$ and $4.6 \times 10^4\ \Omega^{-1}\ cm^{-1}$, respectively and hence TiN is expected as a good candidate for back contact material. It is also known that the electrical conductivity of TiN depends on the composition ratio of titanium to nitrogen. Moreover, titanium alloys are well known to be corrosion resistant and chemically stable, and therefore used as a lightweight hardness abrasive material[5]. So with regard to the same we suggest more research could be done as TiN as back contact material.

- ☐ Noble metals deposited on semiconductor particles have been shown to improve photocatalytic electron transfer processes at the semiconductor interface[6]. Hence the concept of using functional nanocomposites involving metals especially plasmonic materials with TiO_2 is worth trying.

- ☐ So far, there have been limited investigations on DSSCs with various TiO_2 morphological composites such as, nanowires/nanospheres and so on[7,8]. These kinds of composites offer advantages of both the morphology.

- ☐ TiO_2 based nanocomposites can be doped for fabricating microstructured Polymethyl Metha Acrylate (PMMA) optical fibres, which have huge applications for sensing, engineering, medicine and so on.

7.3 References

---

[1] Dong, S., Chen, X., Gu, L., Zhou, X., Xu, H., Wang, H. and Chen, L. (2010). “Facile preparation of mesoporous titanium nitride microspheres for electrochemical energy storage”. *ACS Appl. Mater. Interfaces*, *3*(1), 93-98.

[2] Cheng, D. J., Sun, W. P., & Hon, M. H. (1987). “The morphology and structure of chemically vapour-deposited Ti (C, N) coatings”. *Thin Solid Films*, 146(1), 45-53.

[3] J. M. Kroon, N. J. Bakker, H. J. P. Smit, P. Liska, K. R. Thampi, P. Wang, S. M. Zakeeruddin, M. Gr€atzel, A. Hinsch, S. Hore,U. W€urfel, R. Sastrawan, J. R. Durrant, E. Palomares,H. Pettersson, T. Gruszecki, J. Walter, K. Skupien and G. E. Tulloch, “Nanocrystalline Dye-Ensi- Tized Solar Cells Having Maximum Performance”. *Progr. Photovolt.: Res. Appl.*, 2007, 15,1.

---

[4] N. Fuke, A. Fukui, R. Komiya, A. Islam, Y. Chiba, M. Yanagida, R. Yamanaka, and L. Han, (2008) "New approach to low-cost dye sensitized solar cells with back contact electrodes." *Chem. Mater*. 20(15), 4974–4979.

[5] Yoo, B., Kim, K. J., Kim, Y. H., Kim, K., Ko, M. J., Kim, W. M., & Park, N. G. (2011). "Titanium nitride thin film as a novel charge collector in TCO-less dye-sensitized solar cell". *J. Mater. Chem.*, *21*(9), 3077-3084.

[6] Subramanian, V., Wolf, E., & Kamat, P. V. (2001). "Semiconductor-metal composite nanostructures. To what extent do metal nanoparticles improve the photocatalytic activity of TiO_2 films." *J. Phys. Chem. B*, *105*(46), 11439-11446.

[7] Tan, B., & Wu, Y. (2006). "Dye-sensitized solar cells based on anatase TiO_2 nanoparticle/nanowire composites". *J. Phys. Chem. B*, *110*(32), 15932-15938.

[8] Lee, C. H., Rhee, S. W., & Choi, H. W. (2012). "Preparation of TiO_2 nanotube/nanoparticle composite particles and their applications in dye-sensitized solar cells". *Nanoscale Res. Lett.*, *7*(1), 1-5.

Appendix